

**About the Mechanics
of SSC Dipole Magnet Prototypes***

A. Devred, et al.

Magnet Division
Superconducting Super Collider Laboratory[†]
2550 Beckleymeade Ave.
Dallas, TX 75237

November 1991

*To be published in AIP Conference Proceedings Series, "The Physics of Particle Accelerators"
January 1992.

[†]Operated by the Universities Research Association, Inc., for the U.S. Department of Energy under
Contract No. DE-AC35-89ER40486.

ABOUT THE MECHANICS OF SSC DIPOLE MAGNET PROTOTYPES

A. Devred, T. Bush, R. Coombes, J. DiMarco, C. Goodzeit, J. Kuzminski,
M. Puglisi, P. Radusewicz, P. Sanger, R. Schermer, G. Spigo, J. Tompkins,
J. Turner, Z. Wolf, Y. Yu, and H. Zheng

Magnet Systems Division
Superconducting Super Collider Laboratory*
2550 Beckleymeade Avenue
Dallas, Texas, USA

T. Ogitsu
Superconducting Super Collider Laboratory and
KEK, National Laboratory for High Energy Physics
1-1 Oho, Tsukuba-shi
Ibaraki-ken, Japan

M. Anerella, J. Cottingham, G. Ganetis, M. Garber, A. Ghosh, A. Greene,
R. Gupta, J. Herrera, S. Kahn, E. Kelly, A. Meade, G. Morgan, J. Muratore,
A. Prodell, M. Rehak, E. P. Rohrer, W. Sampson, R. Shutt, P. Thompson,
P. Wanderer, and E. Willen

Brookhaven National Laboratory
Upton, New York, USA

M. Bleadon, R. Hanft, M. Kuchnir, P. Mantsch, P. O. Mazur, D. Orris,
T. Peterson, and J. Strait

Fermi National Accelerator Laboratory
Batavia, Illinois, USA

J. Royet, R. Scanlan, and C. Taylor

Lawrence Berkeley Laboratory
Berkeley, California, USA

ABSTRACT

During the last two years, nine 4-cm-aperture, 17-m-long dipole magnet prototypes were produced by Brookhaven National Laboratory (BNL) under contract with the Superconducting Super Collider (SSC) Laboratory. These prototypes are the last phase of a half-decade-long R&D program, carried out in collaboration with Fermi National Accelerator Laboratory and Lawrence Berkeley Laboratory, and aimed at demonstrating the feasibility of the SSC main-ring dipole magnets. They also lay the groundwork for the 5-cm-aperture dipole magnet program now underway. After reviewing the design features of the BNL 4-cm-aperture, 17-m-long dipole magnets, we describe in detail the various steps of their fabrication. For each step, we discuss the

* Operated by the Universities Research Association, Inc., for the U.S. Department of Energy under Contract No. DE-AC35-89ER40486.

parameters that need to be mastered, and we compare the values that were achieved for the nine most recent prototypes. The data appear coherent and reproducible, demonstrating that the assembly process is under control. We then analyze the mechanical behavior of these magnets during cooldown and excitation, and we attempt to relate this behavior to the magnet features. The data reveal that the mechanical behavior is sensitive to the collar-yoke interference and that the magnets exhibit somewhat erratic changes in coil end-loading during cooldown.

1 INTRODUCTION

The key event for the Superconducting Super Collider (SSC) collider dipole magnets during 1990 was the decision taken in January to increase the aperture from 4 cm¹ to 5 cm.² The reason for this decision was to improve the field quality in order to reduce the risk of beam losses.³ However, the implementation of such a change required the development of new tooling, which would take 12–18 months. It was therefore decided to continue the production of 4-cm-aperture prototypes so that design concepts developed for the 4-cm program could be tested before they were scaled up to the 5-cm program.

In this paper, we report on the design, fabrication, and mechanical behavior during cooldown and excitation of the nine most recent 4-cm-aperture, 17-m-long collider dipole magnet prototypes. The nine cold masses were built at Brookhaven National Laboratory (BNL). Three of them (designated DD0026, DD0027, and DD0028) were cold-tested at Fermi National Accelerator Laboratory (FNAL);^{4,5} the other six (designated DC0201, DC0202, DC0203, DC0204, DC0205, and DC0206) were cold-tested at BNL. In the second section of this paper, entitled “Magnet Features,” we shall start by reviewing the baseline design of these magnets, and we shall try to explain the role of the various components and how they are supposed to interact. We then shall detail the design variants that were implemented on some of these magnets and how they were expected to influence the performance. In the third section, entitled “Magnet Assembly,” we shall describe the successive steps of the assembly process, and we shall list the parameters that need to be controlled. As we go along, we shall summarize the assembly data of the nine magnets and discuss their reproducibility. In the fourth and fifth parts, entitled “Magnet Cooldown” and “Magnet Excitation,” we shall analyze the mechanical behavior of these magnets during cold testing, focusing primarily on the changes in coil azimuthal compressive stress and coil axial end-load. (The changes during cooldown result from differences in thermal shrinkage between the various magnet components. The changes during excitation result from the Lorentz force on the conductors.) As we go along, we shall attempt to relate the mechanical behavior to the construction features, and we shall discuss how that behavior conforms to the design concepts.

This paper is a summary of two previously published review papers^{6,7} to which we have added the data from four more magnets. Preliminary reports on the quench performance and the field quality of these nine magnets can be found in References 8 and 9. More detailed discussions on how quench performance and field quality are influenced by the mechanical design and behavior will be presented elsewhere.^{10,11}

2 MAGNET FEATURES

2.1 Baseline Design

2.1.1 Baseline Design Concepts

The nine magnets presented here, like their predecessors, follow the 1986 conceptual design¹ with a 4-cm aperture and a magnetic length of 16.6 m. A cross-sectional view of the cold mass

assembly is shown in Figure 1. The dipole field is produced by a two-layer cosine-theta coil that is mechanically constrained, both radially and axially, by stainless-steel collar laminations and by stainless-steel end plates. Iron yoke laminations, located outside the collars, enhance the magnetic field by roughly 20%. The cold mass is completed by an outer stainless-steel shell that delimits the region of circulation for the 4.35 K, 0.4 MPa forced flow of supercritical He. The design current is 6500 A, corresponding to a central field of 6.6 T.

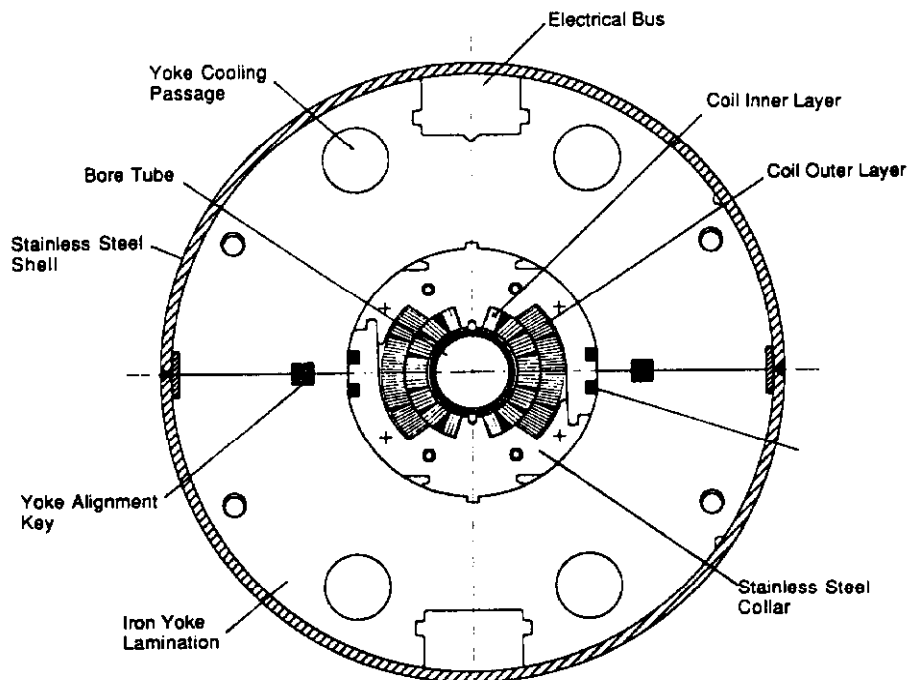


Figure 1. Cross-sectional view of the cold mass of BNL 4-cm-aperture, 17-m-long collider dipole magnet prototype (DC-series).

The first full-length collider dipole prototypes that were built (1986–87) exhibited excessive training.^{12–14} In order to understand this training behavior, subsequent magnets were instrumented with voltage taps on the coil inner layer (to locate the quench origins),¹⁵ and with beam-type strain-gauge transducers (to measure the azimuthal pressure exerted by the coil against the collar pole).¹⁶ Strain gauges were also mounted on the external surface of the cold mass shell to measure both radial and azimuthal stresses.¹⁷ Several features of the magnet design were then varied to determine their influence on quench performance. In 1988, it was found that the best-performing magnets were those with rigid support of the coil ends against the end plates and those where the iron yoke contributed to the radial support of the coil by interfering with the collars.^{17–19} The design of the collars and the yoke was then modified to ensure that this interference would occur, leading to the concept of *line-to-line fit*, the details of which were refined throughout 1989,²⁰ and which is now the baseline of the SSC main-ring dipole magnet program.

The starting point of the line-to-line fit design is the decision to make the outer radius of the stainless-steel collar laminations the same as the inner radius of the iron yoke laminations at room temperature. During collaring, the coil is squeezed into the collars with a large azimuthal pre-compression. After collaring, the coil exerts a large pressure against the collar poles, and the collared-coil assembly deflects along the vertical axis, becoming larger than the rated inner diameter of the iron yoke. When the yoke is put on, a gap thus remains between its two halves. This gap is progressively closed during the welding of the outer shell, which is put under tension and

compresses the yoke. After welding, the gap is entirely closed, and the outer circumference of the collar and the inner circumference of the yoke fit perfectly. During cooldown, the coil shrinks more than the stainless-steel collars, which in turn shrink more than the iron yoke. The pressure exerted by the coil on the collar poles thus decreases, but it remains large enough to keep deflecting the collars, thereby maintaining contact with the yoke on the vertical diameter. During excitation, azimuthal stress is redistributed while the coil tends to expand radially, especially at the midplane. The collared-coil assembly thus deflects along the horizontal axis and eventually contacts the yoke. At high currents, the collared-coil assembly thus contacts the yoke on a large perimeter on both sides of the midplane, and the yoke provides an extremely stiff support against the radial component of the Lorentz force. Also, the yoke defines a clear circular boundary for the collared-coil assembly, which is needed to ensure good field quality. At all times, the gap at the midplane of the yoke remains closed due to the compression exerted by the outer shell.

Having briefly explained the concepts underlying the design of these magnets, we shall now review the different components that constitute the cold mass.

2.1.2 Coil

The inner layer of the coil contains 16 turns and 3 copper wedges. It is wound from a 1.6° keystone-angle cable of 23 strands (strand diameter 0.808 mm). The outer layer contains 20 turns and 1 copper wedge and is wound from a 1.2° keystone-angle cable of 30 strands (strand diameter 0.648 mm). The strand twist pitch, before cabling, is 13 mm for both the inner- and the outer-layer cables; it lengthens to 15 mm after cabling. The inner-layer cable pitch length is 79 mm, while that of the outer-layer cable is 74 mm. The insulation for both inner- and outer-layer cables consists of a 25.4- μm -thick layer of Kapton,* helically wrapped with a 50% overlap, completed by a 102-to-127- μm -thick layer of epoxy-impregnated fiberglass, wrapped with a 0.5-mm gap. The winding of an inner-layer quarter coil requires about 550 m of conductor, while that of an outer-layer quarter coil requires about 686 m. The asymmetric copper wedges that are introduced between some of the coil turns serve two purposes: 1) they allow fine tuning of the magnetic field's high-order multipole components, and 2) they allow the coil to assume the correct arch-shape by compensating for the keystone-angle of the cables (which is too small).

2.1.3 Collars

The stainless-steel collar laminations are 1.5 mm thick and 15 mm wide and are made by a stamping process. They are spot-welded in pairs in two configurations, called left and right, and the left and right pairs are stacked together alternately into 149.1-mm-long packs. The spot-welding was introduced to increase the rigidity of the collars; the left-right stacking was introduced to eliminate twist in the collared-coil assembly. The collar packs are held together by means of two stainless-steel tubes flared at one end and located near the collar top, in an area of approximate neutral axis. They are locked around the coil by four phosphor-bronze tapered keys (3° taper per side, thus 6° total), which are driven horizontally into the keyways located near the midplane. The tapered keys were preferred to the square keys used on earlier prototypes because they limit the peak pressure on the coil during insertion.²¹ (There is a 50- μm clearance between the key and keyway widths, but this has no real significance.) The collaring of a magnet requires 110 collar packs, corresponding to a total of approximately 22,000 laminations.

As described earlier, the collared coil must be assembled so that while it is at liquid helium (LHe) temperature and is energized, it remains in azimuthal compression and exerts enough pressure against the collar to ensure vertical contact with the yoke. In other words, the pre-compression of the coil at room temperature must be large enough to compensate for the

* Kapton is a registered trademark of E.I. DuPont de Nemours & Co.

differences in thermal shrinkage of the various materials during cooldown and for the redistribution of azimuthal stress caused by the Lorentz force during energization. On the other hand, if the pre-compression is too great, it could degrade the Kapton insulation and create a risk of turn-to-turn or coil-to-ground leakages, or even shorts. (Kapton flows easily: it elongates by 3% at room temperature under a pressure of 69 MPa.) A compromise must therefore be reached; a suitable collaring scheme should limit the peak pressure seen by the coil, while providing enough pre-compression to compensate for the aforementioned losses.

2.1.4 Yoke and Shell

The iron yoke laminations are 1.5 mm thick and 77.47 mm wide and are made of low-carbon steel using a stamping process. They are compactly stacked into 146.4-mm-long modules and are held together by stainless-steel tubes in order to achieve a packing factor of about 97%. The yoke modules are assembled around the collared coil so that the split between the two halves is located at the midplane (see Figure 1). The modules are separated by two 1.5-mm-thick stainless-steel laminations, which are slotted for He venting (see paragraph 2.2.9, "Cross-Flow Cooling"). The two identical keys at the yoke midplane serve two purposes: 1) precise alignment of the yoke modules, and 2) correction of the iron saturation effects on the magnetic field. To avoid over-constraining the alignment, only one key is used for registration, while the other is set loose by oversizing the yoke keyway by about 125 μm . (The side of the laminations with the correctly sized keyway is marked by a notch on the outer perimeter.) The correction of the iron saturation effects will be described in paragraph 2.2.6, "Revised Yoke and Yoke Alignment Key." The total yoke mass in a magnet is approximately 5000 kg. The outer stainless-steel shell is 4.77-mm thick and consists of two halves welded around the yoke. The welds are also located at the yoke midplane.

As described earlier, in order to create sufficient interference between the collared-coil assembly and the yoke, the vertical diameter of the assembly is allowed to become larger than that of the yoke. Immediately after the collared coil is inserted in the yoke, a gap remains between the yoke halves. This gap is expected to close as the shell is welded around the yoke and applies a radial pressure on it. The question of whether it is crucial to ensure that the gap is closed at the end of shell-welding is widely debated. On one hand, if the gap is closed at room temperature, it will stay closed in the cold state, for both the collared-coil assembly and the outer shell have a larger thermal expansion coefficient than the iron yoke (see paragraph 4.2, "Change in Coil Azimuthal Compressive Stress During Cooldown"). The boundary of the collared-coil assembly is thus always well-defined, and its geometry should be very reproducible from magnet to magnet, at both room temperature and LHe temperature. This should help to control the field quality and to obtain good correlations between the warm and cold measurements of the multipole components. (If such correlations can be established, one can then limit the number of production magnets to be cold-tested and can rely on warm measurements to assess whether the magnets meet the field requirements). On the other hand, if the gap is not closed at room temperature, there is no guarantee that it will close during cooldown. If a gap remains at LHe temperature, the first worry is that it would alter the rigidity of the yoke where the radial component of the Lorentz force is the largest. However, this is not thought to be a problem, because as the collared-coil assembly deflects along the midplane and comes into contact with the open yoke, the radial stiffness is supplemented by a bending stiffness of the yoke halves, which also provides a very good support. Another worry is that the gap would distort the magnetic field. On a single magnet, the field distortion was calculated to be significant only if the gap at LHe temperature was larger than 250 μm . However, if there is a gap, its amplitude varies between the warm and the cold states, and one could speculate that on a large sample of magnets these variations could spoil the warm-cold correlations on the multipole components of the field. In order to preserve all the chances of getting good warm-cold correlations, it seems preferable, therefore, to ensure that the yoke midplane gap is closed from the time of the shell-welding. This implies that the vertical deflection of the collared-coil assembly must be kept within reasonable limits.

2.1.5 End Parts

Figure 2 presents a cutaway view of magnet DD0027 end parts. The coil ends maintain the same radial dimension as the straight sections. The spacing of the turns is designed to minimize the harmonic content of the ends. The main spacers are made of laminated, epoxy-impregnated fiberglass. Additional G10 spacers are also inserted between some of the turns to enforce the turn-to-turn insulation. These spacers were determined empirically to position the conductors in an approximate constant perimeter configuration. Each quarter-coil end is contained by a G10 saddle. The axial motion of the G10 saddles at each end of the coil is restrained by a stainless-steel ring, called the *backing ring*. This ring is pressed on by four screws set in the 38.1-mm-thick stainless-steel end plates. The end plates themselves are anchored to a stainless-steel ring, called the *bonnet*, which is in turn welded to the outer shell. The average torque with which the screws are set determines the axial pre-load of the coil. In order to decrease the magnetic field on the end turns, the iron yoke laminations are terminated 47.2 mm before the end of the outer coil straight section, and the last two yoke modules over the coil ends are made of non-magnetic stainless-steel laminations. These laminations are bonded with epoxy to keep the yoke laminations perpendicular to the magnet axis and to avoid "angling" during the skinning process or due to movement of the end collars during axial extension of the coil from the Lorentz forces.

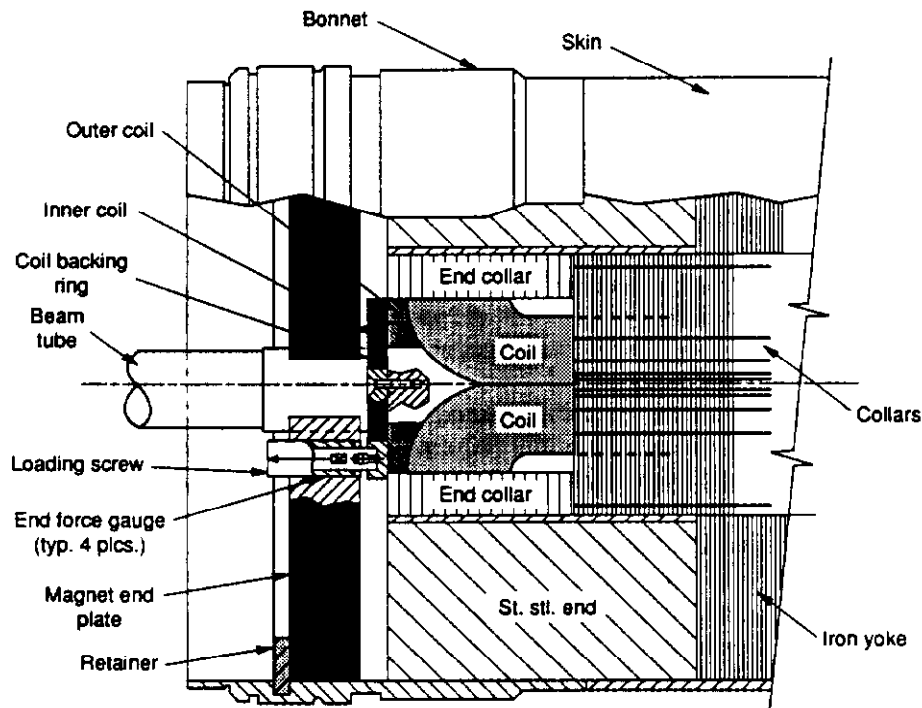


Figure 2. Cutaway view of the non-lead end part of BNL 4-cm-aperture, 17-m-long collider dipole prototype.

2.2 Variants

Having briefly presented the common features of these magnets, we shall now review their differences, which are summarized in Table 1.

Table 1. Variants in Design Features of Most Recent BNL 4-cm-Aperture, 17-m-Long Collider Dipole Magnet Prototypes.

	DD0026	DD0027	DD0028	DC0201	DC0202	DC0203	DC0204	DC0205	DC0206
Inner Conductor Copper-to-Superconductor Ratio	1.44	1.48	1.53	1.53	1.53	1.53	1.29	1.29	1.29
Inner Conductor Critical Current at 4.22K and 7T (A)*	7465	7822	7893	7893	7791	7791	8368	8368	8368
Epoxy Content of Inner/Outer Cable Fiberglass Wrap (% in weight)	24/24	24/24	24/24	24/24	20/24	20/24	20/24	20/24	20/20
Collar Material	High Manganese	Nitronic 40	Nitronic 40	Nitronic 40	Nitronic 40	Nitronic 40	Nitronic 40	Nitronic 40	Nitronic 40
Collar Shape	Round	Round	Round	Anti-Ovalized	Anti-Ovalized	Anti-Ovalized	Anti-Ovalized	Anti-Ovalized	Anti-Ovalized
Collar-Yoke Shim	None	None	None	None	76.2 μm **	76.2 μm **	76.2 μm **	76.2 μm **	76.2 μm **
Yoke Design				Revised	Revised	Revised	Revised	Revised	Revised
Yoke Mass (kg)	5001.1	5001.0	5001.2	5117.8	5122.8	5127.0	5126.9	5129.6	5126.7
End Design	'yoke' set screws	'yoke' set screws	'yoke' set screws removed						

*Measured on conductor short samples

**152.4 μm on diameter

2.2.1 Copper-to-Superconductor Ratio

The inner-layer conductors of the DD-series magnets have a nominal copper-to-superconductor ratio of 1.5 to 1. In the case of the DC-series magnets, three of them (DC0201, DC0202, and DC0203) have a nominal ratio of 1.5 to 1; the three others (DC0204, DC0205, and DC0206) have a nominal ratio of 1.3 to 1. All the magnets use outer-layer conductors with a nominal ratio of 1.8 to 1. The lower inner-layer conductor ratio was employed in order to pursue the possibility, suggested by conductor short sample tests, that copper-to-superconductor ratio could play a significant role in training performance.²² However, as we shall describe elsewhere,¹⁰ most of the training quenches of the DC-series magnets originated in the outer layer, and no significant differences were observed in the quench performance of the inner layer.

2.2.2 Epoxy Content of Inner Layer Conductor Fiberglass Wrap

After magnet DC0201, the epoxy content of the fiberglass wrap around the inner-layer conductor was decreased from 24% to 20% in weight in order to curtail epoxy buildup on the inner surface of the coils. The epoxy content of the outer-layer conductor fiberglass wrap is 24% in weight for all the magnets except DC0206, for which it was lowered to 20%.

2.2.3 Collar Material: Nitronic-40 versus High-Manganese Steel

All magnets use Nitronic-40 stainless-steel collars, except magnet DD0026, which uses High-Manganese stainless-steel collars developed by Kawasaki Steel Corporation. The High-Manganese steel was tried because its integrated thermal expansion coefficient between 300 K and 4.2 K is lower than that of Nitronic 40, 1.7×10^{-3} compared to 3.0×10^{-3} , and thus is lower than that of the yoke, 2.0×10^{-3} . This would seem to allow more even contact of the yoke and the collared-coil assembly during cooldown (see paragraph 4.2.1). The yield strength of both kinds of steel is 620 MPa.

2.2.4 Collar Shape: Round versus Anti-Ovalized

Magnets up to and including DD0028 used *round* collars. The deflection of the collared coil assembly, however, which was measured to be about 250 μm on the vertical diameter after collaring completion, was deemed excessive and was thought to contribute to potential gaps between the yoke halves. The DC-series magnets, therefore, employed *anti-ovalized* collars, intended to compensate for this deflection. The main difference between the round and anti-ovalized collars resides in the location of the keyways with respect to the midplane, as detailed in Figure 3. In the round collars, the keyways are placed so that when the top and bottom collars are joined and keyed (with no coil in them), their centers coincide, resulting in a round shape. In the anti-ovalized collars, the location of the keyways has been modified so that when joined and keyed, the centers of the top and bottom collars are shifted by 254 μm , reducing the collars' vertical diameter by the same amount. (The anti-ovalized collar keyways are also closer to the midplane to enhance the rigidity of the extremity of the collar arms.)

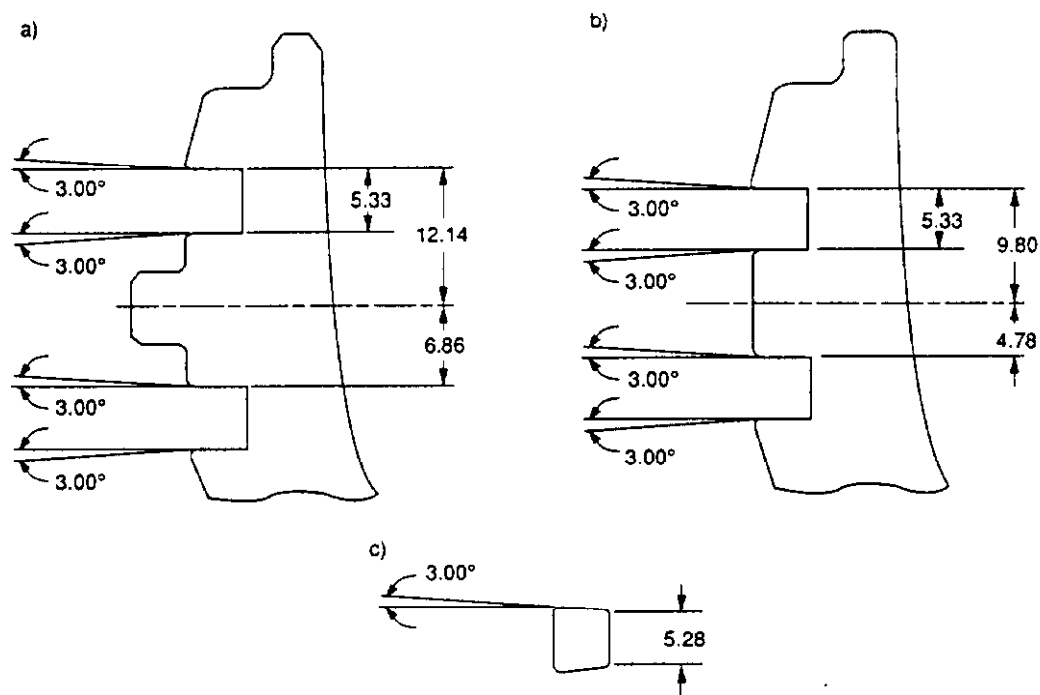


Figure 3. Collar key and keyway designs for most recent BNL 4-cm-aperture, 17-m-long collider dipole prototypes: a) round collar keyway, b) anti-ovalized collar keyway, c) key (the key design is common to the two types of collars).

2.2.5 Collar-Yoke Interference

Tests on DC0201 suggested that the 254- μm reduction of the collar vertical diameter permitted the collared-coil assembly to lose contact with the yoke along the vertical axis in the cold state. Subsequent magnets, therefore, included 19.05-mm-wide, 76.2- μm -thick brass shims located on either side of the tabs at the top and bottom of the collared coil assembly. The shims were secured with double adhesive tape about 100- μm thick before compression, and with a tested post-compression thickness of less than 25 μm .

2.2.6 Revised Yoke and Yoke Alignment Keys

The round collars used on the DD-series magnets had horizontal tabs at the midplane which fitted into grooves punched in the yoke (see Figure 3). These tabs were removed from the anti-ovalized collars, and the notches at the midplane of the yoke were replaced by straight edges.

Another difference between the DD-series and DC-series magnets is the material of the yoke alignment key at the midplane of the yoke. The DD-series magnets use low-carbon magnetic steel keys, while the DC-series magnets use non-magnetic stainless-steel keys. This change was made following computer simulations that showed it would reduce the iron saturation effects at high field. The maximum change in the sextupole harmonic due to non-linear properties of iron is calculated to be less than 0.4 units in the entire range of operation of the DC-series magnets (it would be 1.2 units if the keys were magnetic).²³ It was calculated to be 0.7 units for the DD-series magnets.

2.2.7 Yoke Density

The yoke design specifications call for a fixed overall length and a fixed overall mass. However, in some of the DC-series magnets, spaces developed between the yoke modules because of too tight stacking. Extra laminations were then added in order to achieve the specified overall length, thus resulting in a higher density. Magnets DC0203 and DC0204 included 7 extra laminations per yoke half; magnet DC0205 included 11; magnet DC0206 included 5. The total yoke masses for the different magnets are reported in Table 1.

2.2.8 Yoke Set Screws

Magnets DD0026 and DD0027 included yoke set screws in addition to the coil set screws which push against the backing ring and provide the axial restraint of the coil (see paragraph 2.1.5, "End Parts"). The yoke screws were located at the periphery of the end plates and pushed directly against the yoke. During cooldown, the axial thermal shrinkage of the yoke is smaller than that of the collared-coil assembly and the outer shell (see paragraph 4.3, "Change in Coil Axial Pre-load During Cooldown"). Thus it is possible that in the cold state the yoke set screws could cause a bending of the end plate that would bypass the coil set screws and alter the coil axial loading. The yoke screws were thus removed from DD0028 and excluded from later magnet designs.

2.2.9 Cross-Flow Cooling

All five magnets incorporated a cooling scheme which involves the circulation of He between the various cooling passages in the magnet. At set intervals, He is directed from the top yoke-cooling passages to the coil-cooling passage, and from the coil-cooling passage to the bottom yoke-cooling passages. This *cross-flow* of He perpendicular to the magnet axis allows more of the total mass flow to participate in removing heat from the synchrotron radiation and in maintaining the coil at a suitable temperature.²⁴ The scheme is realized by partially blocking the two top yoke-cooling passages at one end and the two others at the other end, thus creating a radial pressure difference which instigates the cross-flow; the cross-flow occurs at the stainless-steel laminations separating the yoke modules (see paragraph 2.1.4, "Yoke and Shell"). In addition, helium must be prevented from leaking from the cross-flow path into spaces such as the loading flat between the collar and the yoke. Silicon (RTV) or indium plugs are thus periodically placed in these gaps to obstruct any such flow.

The blocking of the yoke cooling passages at the magnet ends is realized by inserting a plug into a stainless-steel tube mounted between each He cooling passage of the last yoke module and the corresponding end-plate hole. On the DD-series magnets, and on magnets DC0201 and

DC0204, the stainless-steel tubes were tack-welded to the end plates and sealed with RTV into the yoke-cooling passages as a safety precaution against high He pressure during a magnet quench. However, it was then thought that the RTV sealing might result in a rigid mechanical connection between the end plates and the yoke. The tubes could thus be pushing against the yoke in a manner similar to that of the yoke set screws, resulting in a similar bending of the end plates. The mounting of the tubes was modified on the subsequent magnets of the DC-series (DC0202, DC0203, DC0205, and DC0206) to avoid any such risk.

2.3 Instrumentation

All nine magnets have the same standard instrumentation, including voltage taps, strain-gauge collar packs, bullet gauge assemblies, and temperature sensors.

2.3.1 Voltage Taps

The total number of voltage taps is 41, all of which—except the quarter-coil voltage taps used for quench detection—are located on the inner layer of the coil. The instrumented turns are the three turns of the first block near the pole, and the first turn of the second block adjacent to the wedge. Extra taps are also located in the ramp-splice area where the inner-layer conductor ramps up to the radius of the outer layer and is spliced to the outer-layer conductor.

2.3.2 Strain-Gauge Collar Packs

Magnets DD0027 and DD0028 are both equipped with two strain-gauge collar packs. The axial locations of the packs are determined from the azimuthal size measurements that are performed after coil curing (see paragraph 3.1.3, “Azimuthal Coil Size Measurements”), with one pack located near the minimum inner-layer size, and the other located near the maximum. (Since the fluctuations in the coil size are coming from non-uniformities in the curing fixture, the axial locations of the extrema are very reproducible from coil to coil.) Each pack contains eight beam-type strain-gauge transducers to measure the azimuthal pressure exerted by the different quarter-coils against the collar pole faces, and six compensating gauges—two for the inner layer transducers and four for the outer ones.¹⁶ The other magnets have only one strain-gauge collar pack, located at the minimum inner-layer size.

2.3.3 Bullet Gauge Assemblies

All nine magnets are instrumented with special set screws located at the *return end* of the magnet. (The return end is the magnet end opposite where the current leads are connected.) These screws are machined to accommodate a small cylindrical piece, called the *bullet*, on which strain gauges are mounted to measure the force exerted by the coil against the end plate; these are designated as *bullet gauge assemblies*.¹⁶ Each of the four bullets has two active gauges. The eight active gauges share two compensating gauges.

2.3.4 Temperature Sensors

The instrumentation of all nine magnets also includes four carbon-glass resistor thermometers, two mounted in one of the four He bypass holes in the *lead-end* end plate (the lead end is the magnet end where the current leads are connected), and the other two mounted in one of the four He bypass holes in the return-end end plate. These sensors were added to better track the coil temperature.

2.3.5 Test Stand Instrumentation

The test stands of the BNL and FNAL test facilities are instrumented to monitor the flow of He and other cryogenic parameters. In particular the stand instrumentation includes warm and cold pressure transducers at both ends of the magnet.

3 MAGNET ASSEMBLY

3.1 Coil Assembly

The four quarter coils are wound and cured separately, then joined during the assembly process.

3.1.1 Winding

The coils are wound onto convex, laminated mandrels using the *shuttle-type* winding machine pictured in Figure 4. The cable is fed from a quasi-static supply spool while the mandrel is shuttled back and forth longitudinally.²⁵ After the mandrel has travelled one length, the supply spool transfers to the other side of the mandrel, which in turn retraces its path to complete one turn. The mandrel is also rocked azimuthally to ensure a proper lay of the cable, especially at the

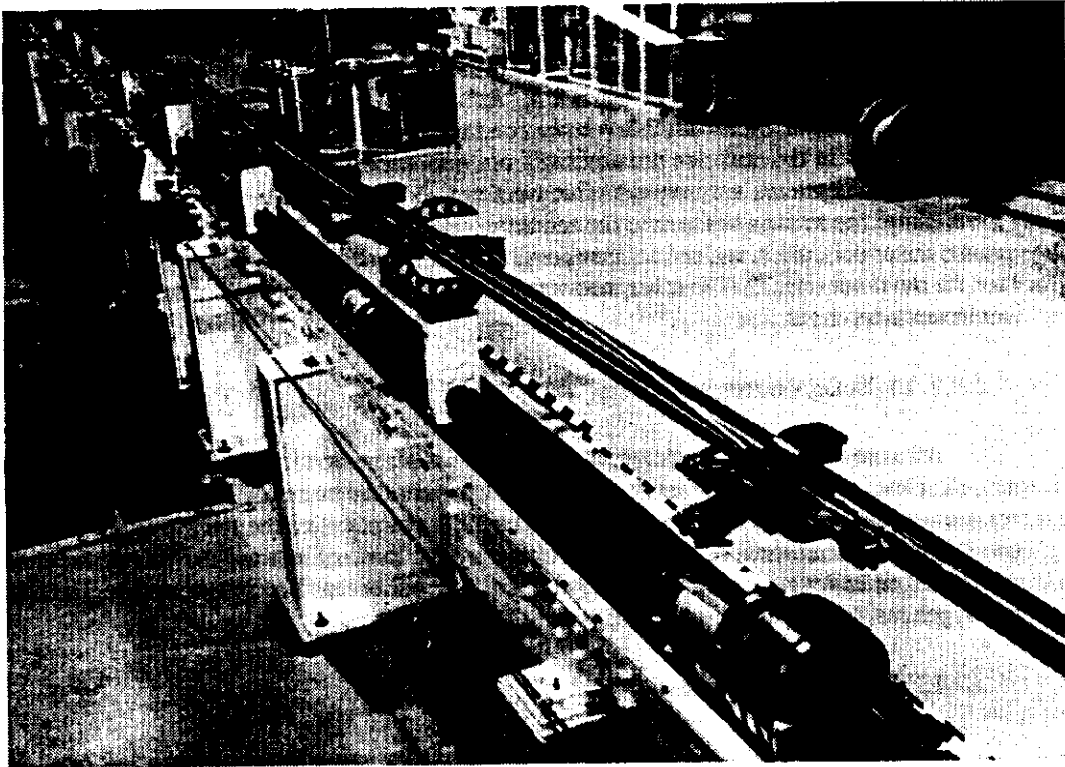


Figure 4. BNL shuttle-type winding machine for 4-cm-aperture, 17-m-long collider dipole magnet coils.

ends. Throughout the operation, the cable tension is maintained constant at about 175 N. For the outer coils, a 75- μm sheet of Teflon and fiberglass-impregnated tape is laid over the mandrel. This has been shown empirically to enhance the quality of the outer coil's inner surface which, in the final assembly, rests against the inner coil.

After winding is completed, a 25.4- μm -thick layer of tedlar is wrapped with roughly 50% overlap around the coil on its mandrel, to keep them together and to facilitate subsequent manipulations. The tedlar wrapping also permits compaction and reduction of the radial dimensions of the coil ends, where the conductors have a tendency to spring back. It then helps to protect the coil, as the coil-mandrel assembly is turned down and laid into the curing mold cavity. It also acts as a mold release at the end of curing.

3.1.2 Curing

The objectives of curing are three-fold: 1) to polymerize the epoxy of the cable insulation in order to make the coil rigid and thus easier to manipulate, 2) to form the coil into the correct shape and the correct dimensions, and 3) to make the coil as uniform as possible along the coil length. Correctness of the coil dimensions is important for the field quality. Uniformity of the coil is also required to achieve uniform pre-compression after collaring.

Figure 5 shows the bed of the curing press onto which the tedlar-wrapped coil-mandrel assembly is laid. This bed consists of concave, laminated-steel blocks, constructed to very accurate

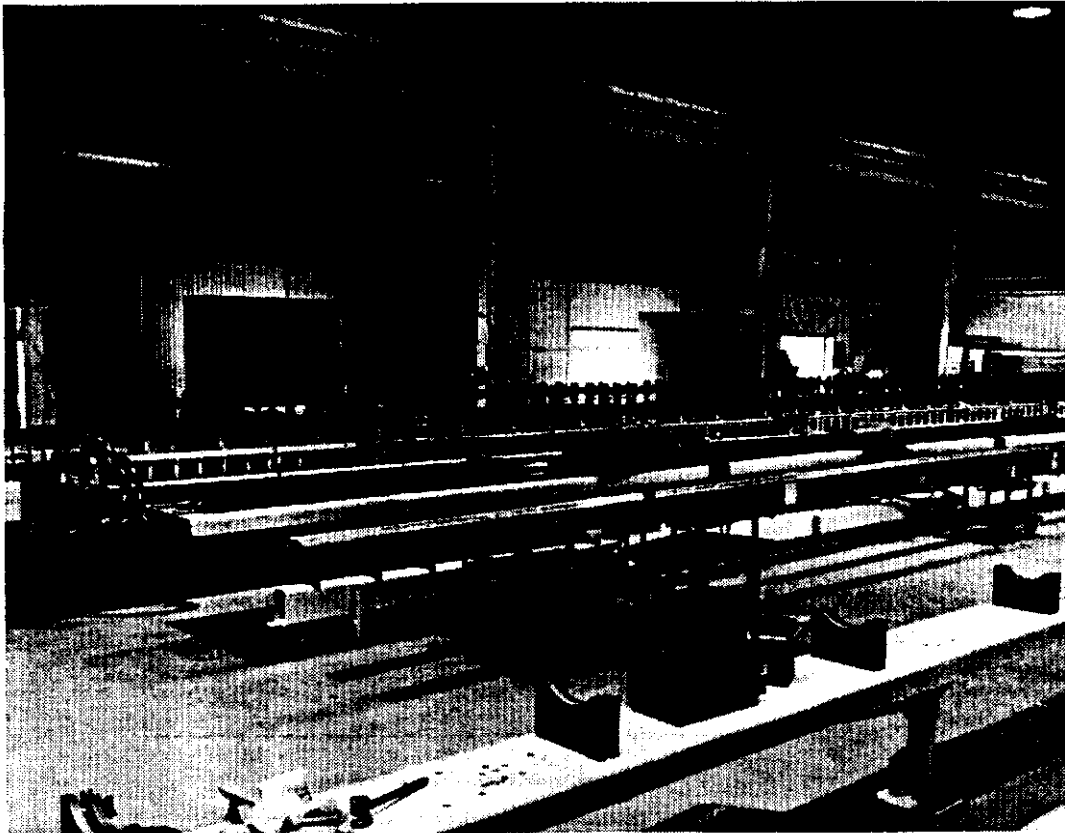


Figure 5. BNL curing press and molding fixtures for 4-cm-aperture, 17-m-long collider dipole magnet coils.

dimensions and called *form blocks*. These form blocks can be heated by the circulation of oil. Coil-mandrel assembly and form blocks are covered by steel contact parts, called *top hats*, which are hydraulically pressed. The nominal curing pressure is $50 \text{ MPa} \pm 15 \text{ MPa}$ for both inner and outer quarter-coils. The heating sequence includes several steps. The first phase consists in ramping up the temperature to 90° C , at which point epoxy enters the gel phase. Measurements of the gaps between the form blocks and the top hats are made along the curing fixture to determine the azimuthal size of the coil under the nominal curing pressure. These measurements are used to determine the thickness of a shim to be inserted between the form blocks and the hats. The shim limits the pressure applied to the coil in order to avoid problems such as electrical shorts between turns, or cable or strand deformation. The second phase of the operation is the curing itself, during which both temperature and pressure are increased, the former to 135° C , the latter until the gap closes between the form blocks and the top hats. These conditions are maintained for about 100 min. The last phase is simply cooldown to room temperature. During the curing phase, the ends are also loaded to a nominal force of 8500 N.

3.1.3 Azimuthal Coil Size Measurements

When curing is complete, the tedlar wrap is removed, and the coil is separated from its mandrel and placed on a stable fixture. A measuring device is used manually to compare the azimuthal size of the coil to that of a steel block of accurate dimension, called the *master*. There are two masters—one used for inner-layer coils and one used for outer-layer coils—which assume the design coil sizes. The measurements are taken at intervals of 0.75 m on both sides of the coil straight sections, under a pressure of 70 MPa for the inner coil and of 55 MPa for the outer coil. (These pressures are the target pre-compressions for the collaring.)

Figure 6 shows a typical example of azimuthal coil size measurements as a function of axial location for the coils used in magnet DC0204. The four traces correspond to the four quarter-coils. The values are the deviations from the master size of each layer, and, for each position, are averaged over the left and right sides of the coil. (A positive deviation indicates a coil size larger

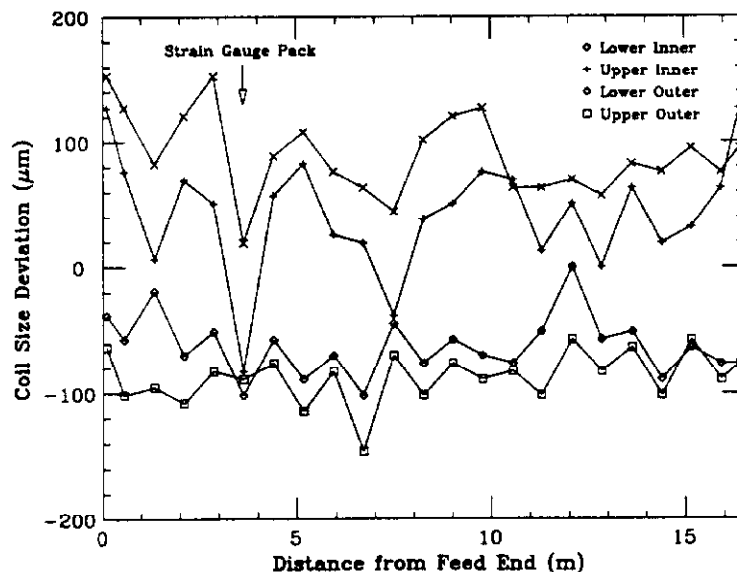


Figure 6. Azimuthal coil size deviations measured along the four quarter-coils assembled in BNL 4-cm-aperture, 17-m-long collider dipole magnet prototype DC0204. The deviations are measured with respect to steel masters. Each point is an average between measurements taken at the given axial location on both sides of the quarter-coil.

than that of the master). Also shown in Figure 6 is the position selected for the strain gauge pack. Table 2 summarizes the coil size measurements for all nine magnets. The values are the deviations from the master size and are averaged over the length of the two inner and two outer quarter-coils. It appears that the coil sizes vary slightly from magnet to magnet, presumably due to slightly different cable dimensions or slightly different curing conditions. However, it also appears that for a given magnet, the standard deviation does not exceed 50 μm ; the uniformity of the coils is thus very good. As we shall see, these coil size measurements are used to optimize the thicknesses of the shims that are inserted between the collar poles and the coils to achieve suitable coil pre-compression (see paragraph 3.2.1, "Optimizing the Coil Pre-Compression").

Table 2. Average Coil Size Deviations, Coil Shim Thicknesses, and Effective Sizes of Coil Packages of Most Recent BNL 4-cm-Aperture, 17-m-Long Collider Dipole Prototypes (in μm).

Magnet	Inner Layer			Outer Layer		
	Size Deviation ^a	Shim Thickness	Package Size ^b	Size Deviation ^a	Shim Thickness	Package Size ^b
DD0026	122 \pm 49	640	710	-64 \pm 23	820	720
DD0027	138 \pm 51	640	845 ^c	-63 \pm 27	820	755 ^c
DD0028	61 \pm 27	640	680 ^c	-125 \pm 51	820	695 ^c
DC0201	-7 \pm 36	720	760	-162 \pm 39	770	750
DC0202	30 \pm 23	640	770	-88 \pm 24	720	710
DC0203	167 \pm 43	640	870	-73 \pm 33	720	740
DC0204	67 \pm 23	640	730	-74 \pm 23	720	740
DC0205	87 \pm 43	640	720	-81 \pm 28	720	755
DC0206	16 \pm 42	770	820	-82 \pm 30	820	840

^a Left-right average over the length of the two coil halves.

^b At the axial location of the strain-gauge pack.

^c At the axial location of the feed-end pack.

As we shall describe later (see paragraph 4.2.1.3, "Non-Linearity and Temperature Dependence of the Coil Mechanical Properties"), the coil mechanical properties at low pressure are highly non-linear. For high pressure, however, the coil stress-strain curve tends to become linear,²⁶ and an effective Young's modulus and an effective coil spring rate can be defined. Measurements on the inner coils of the 4-cm-aperture, 17-m-long dipole prototypes led to a spring rate of 0.2 MPa/ μm in the range of 35–80 MPa.

3.1.4 Splicing and Final Assembly

In the final stages of the coil assembly, the four quarter-coils are encased in Kapton caps to reinforce the ground insulation and to reduce the risk of flashing between the edges of the conductor and the collars. The quarter-coils are then assembled into two half-coils, each consisting of one inner and one outer layer. A 50.8- μm sheet of Teflon is inserted between the two layers to smooth the interface and create a slip plane. The layers of each half-coil are then connected electrically in series by what is called a *ramp-splice*.

The ramp-splice, represented in Figure 7, is formed as follows. First, conductor from the inner layer pole turn is bent radially in its plane in order to ramp up to the outer coil radius; bending begins 14 cm from the end of the inner coil straight section. The conductor is then spliced over a length of 76.2 mm to conductor from the outer layer pole turn, using a 96% tin–4% silver

solder. (The splice length is approximately equal to the average twist pitch of the inner and outer layer conductors.) The ramp and splice are then encased in a G10 holder, 152.4 mm in length. For the DD-series magnets, the area where the inner-layer conductor enters the G10 holder was observed as the origin of a large number of quenches.¹⁸ Therefore, starting with magnet DC0201, a length of conductor from the inner-layer pole turn before the ramp was epoxied to the adjacent turn in order to prevent this turn from moving radially inward during collaring. (This is the only place on the coil where the turns are not laminated together.)

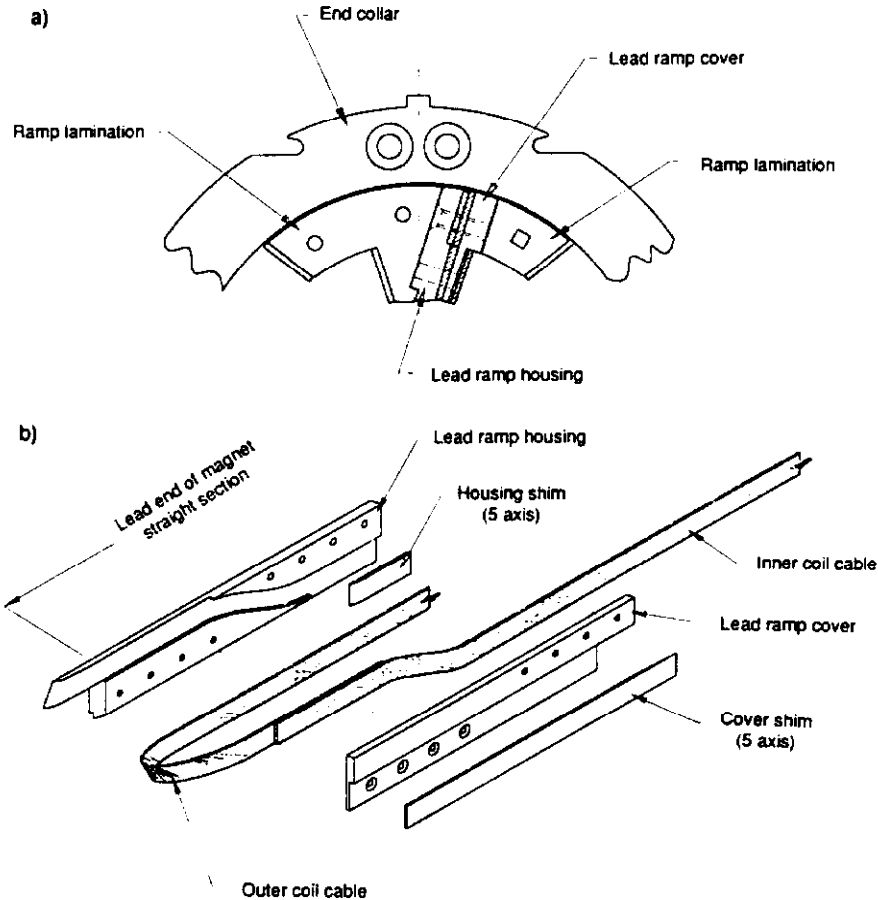


Figure 7. Detailed design of the ramp-splice between the inner and outer layers of a BNL 4-cm-aperture, 17-m-long collider dipole magnet coil: a) cross-sectional view, b) exploded view.

The coil halves, joined now by the ramp-splice, are then assembled around the beam tube, made of Nitronic 40 stainless steel with a wall thickness of 1.27 mm. The outer surface of the coil assembly is covered by several layers of ground insulation that sandwich the quench protection heaters, as detailed in Figure 8. First, comes a pair of 101.6- μm -thick Kapton caps. Next is a 25.4- μm -thick layer of Teflon, which creates a sliding surface between the coil and the collars. Next is another 127- μm layer of Kapton, followed by the quench protection heater assemblies (one per quadrant); each assembly consists of a 101.6- μm -thick copper-clad, stainless-steel strip, glued between two 25- μm -thick layers of Kapton, and covered by another 127- μm -thick layer of Kapton. Next are two more 127- μm -thick layers of Kapton. Finally there is a 381- μm -thick layer of stainless steel, called the *collaring shoe*, whose purpose is to protect the coil insulation against the ripples of the collar laminations.

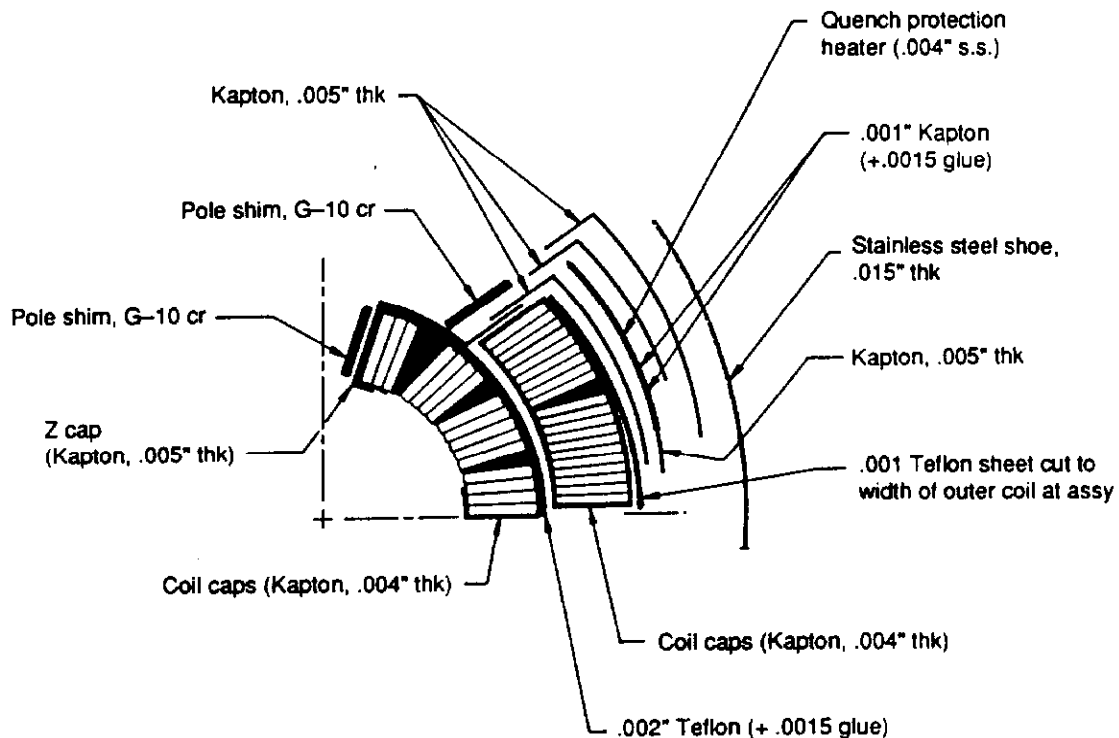


Figure 8. Assembly drawing of the ground insulation of a BNL 4-cm-aperture, 17-m-long collider dipole magnet coil. The dimensions are in U.S. customary units: 0.001 in = 25.4 μm .

3.2 Collaring and Keying

Collaring is one of the most important steps in the magnet assembly. It is during collaring that the coil is pre-compressed, and it is this pre-compression which deflects the collars and creates the interference with the yoke along the vertical diameter. It is, therefore, crucial to achieve suitable pre-compression and suitable collar deflection in demonstrating the feasibility of the line-to-line fit design. Similarly, the design's feasibility hinges on whether the coil pre-compression and collar deflection for real magnets are reproducible enough to make these features part of a production process. We shall now describe the details of the collaring technique, then discuss the reproducibility of the collaring data on our sample of magnets.

3.2.1 Optimizing the Coil Pre-Compression

3.2.1.1 Pole Shims. As just stated, one of the goals of collaring is to apply to the coil a suitable level of azimuthal compressive stress. The azimuthal pre-compression is achieved by squeezing the coil into a cavity smaller than the coil at rest. The level of pre-compression is determined by the coil's size and spring rate and by the arc length of the cavity delimited by the collars. However, the coil properties depend on many parameters, including the conductor dimensions, the epoxy content of the insulation, and the curing parameters, which in the course of an R&D program are deliberately varied. To achieve a reproducible level of pre-compression, the arc length of the collar cavity must therefore be varied. Since it is not practical to stamp new collars for each magnet, the collars are deliberately designed with cavities larger than necessary. Brass shims of adjustable thicknesses, referred to as *pole shims*, are introduced between the collar poles and the coil. The level of coil pre-compression is thus determined by the pole shim thickness.

3.2.1.2 Optimizing the Pole Shim Thickness. Since the coil properties can vary, the most reliable way to optimize the shim thickness is to measure the actual size under pressure of each individual quarter-coil before collaring, as described in paragraph 3.1.3 “Azimuthal Coil Size Measurements.” Let s_m designate the measured azimuthal size of a given quarter-coil under a pressure, σ_m . The spring rate of the coil is a non-linear function of the coil stress; however, as we mentioned earlier, for pressures in the 35–80 MPa range, it can be considered as constant. The azimuthal coil size, s , can then be related to the coil stress, σ , and to the coil spring rate, k , by

$$\sigma = \sigma_m + k (s - s_m) . \quad (1)$$

To achieve a target pre-compression, σ_0 , the azimuthal size of the coil must be

$$s = s_m + \frac{\sigma_0 - \sigma_m}{k} . \quad (2)$$

Let l_0 designate the fixed arc length of the collar cavity containing a given coil layer. The thickness, t , of the two identical shims to be inserted between the upper and bottom poles of the collar and the quarter-coils of the given layer is determined by

$$l_0 = s_u + s_l + 2t , \quad (3)$$

where s_u designates the azimuthal size of the upper quarter-coil of the given layer under the pressure σ_0 , and s_l , the azimuthal size of the lower quarter-coil.

Table 2 summarizes the coil size measurements of the magnets of interest. The values in Table 2 are, in fact, the differences between the actual coil sizes, s_m , and that of the master, s_d , for the quarter-coil of the given layer under a compression, σ_m . These are averaged over the upper and lower quarter-coils. If t_d designates the design shim thickness, defined as

$$t_d = \frac{l_0}{2} - s_d , \quad (4)$$

the optimized shim thickness, t_o , is given by

$$t_o = t_d - (s_m - s_d) . \quad (5)$$

(In deriving Eq. (5), we assume that $\sigma_m = \sigma_0$. If it does not, the sizes would have to be corrected using Eq. (2).)

In practice, however, Eqs. (3) through (5) must be corrected to take into account the collar deformations. As the coil is pre-compressed into the collars, it exerts a large pressure against the collar poles, which results in a deflection of the collars along the vertical diameter. As the collars deflect, the azimuthal length of the collar cavity increases, which, in turn, results in a decrease of the coil azimuthal compressive stress. The amplitude of this effect is not easy to predict, for, as we shall describe later, the collar deformations are partially inelastic (see paragraph 3.2.4, “Collar Deflection Comparison”). The deformations are nevertheless reproducible, and an empirical correction can be derived.

3.2.1.3 Implementing the Pole Shims. Whereas in principle it would be possible to take many coil size measurements and custom-design shims for each individual collar pack, this would

considerably increase assembly time. Therefore, in practice, custom-designed shims are used only for the packs covering the coil ends or at the axial locations where there are large deviations in the coil sizes. For the straight sections, the optimization is done on average over the coil length, and an average shim thickness is calculated for each of the coil layers. Trials are then performed in order to verify the shim sizing in relation to the target pre-compressions. If the target pre-compressions are not achieved, the shim thicknesses are adjusted. Table 2 presents the result of this optimization for the coil straight sections of the magnets of interest. (The target pre-compression is 70 MPa for the inner layer and 55 MPa for the outer layer; the design shim thickness is 533.4 μm for the inner layer and 660.4 μm for the outer layer.) Shims of the pre-determined thicknesses and of the same length as the collar packs are then mounted on the eight faces of the collar poles of each pack. In order to avoid sliding during collaring, they are *mechanically seated* by means of small tabs fitting into grooves in the end of each pack. (To permit an efficient seating, the pack lengths are eventually adjusted to that of the shims by means of washers between some of the laminations.)

3.2.1.4 Coil Midplane Position. As mentioned earlier, the current plan is to use shims only during the R&D phase of the program. Once the parameters of the design are entirely determined and the fabrication process is under control, the shim thicknesses should no longer vary from magnet to magnet. It will then be a matter of correcting the pole angle of the collars to include this extra thickness. However, experience with the HERA dipole magnets showed that the shimming could not be abandoned, for it offers a means to correct for eventual errors in the skew quadrupole component of the magnetic field.²⁷ A skew quadrupole component usually arises from a displacement of the coil midplane. The position of the coil midplane is determined by a force balance between the upper and lower quarter-coils. If a quarter-coil is larger or stiffer than the corresponding quarter-coil of the other half (that is, if s_u and s_l are not equal), the midplane is shifted, and an asymmetry is introduced between the coil halves. This asymmetry results in a skew quadrupole component. There is no way to control the position of the midplane, except by controlling the coil properties. If the coils cannot be made perfectly identical, one can either sort the coils to assemble matching pairs or partially correct for the differences between s_u and s_l by introducing different-sized pole shims between the upper and lower halves. For instance, let t_u and t_l designate the thicknesses of the upper and lower pole shims. Eq. (3) then becomes

$$l_0 = (s_u + t_u) + (s_l + t_l) \quad . \quad (6)$$

Another equation must be added to express the minimization of the skew quadrupole component, which either requires a numerical computation or must rely on empirical data. In the case of the SSC dipole magnets, the goal is to impose very tight quality control on the coil fabrication in order to produce coils with nearly identical properties that would not require any sorting or shimming. The pre-production series magnets will tell us if such a goal is achievable.

3.2.2 Collaring and Keying

3.2.2.1 Description of the Process. Once the shims have been installed on the collar packs, the packs are placed manually around the coil and beam tube assembly, starting from the *lead end* of the coil, where the electrical connections are located. The assembly is then placed onto a precision, carefully aligned bed against which the collaring press operates. The press itself is about 2 m long and is moved along the collaring bed, as seen in Figure 9. It is equipped with two series of hydraulic cylinders. The vertical cylinders are used to press on the top and bottom halves of the collar packs until the keyways at the collar sides are almost aligned. The horizontal cylinders are then pressurized incrementally to drive the tapered keys into the keyways, as the vertical cylinder pressure is incrementally reduced. Once the keys are inserted, the horizontal pressure is released.

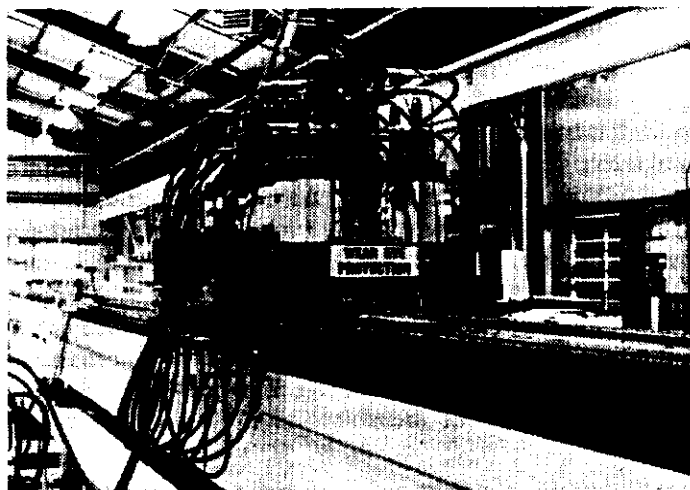


Figure 9. BNL collaring press for the 4-cm aperture, 17-m-long collider dipole magnet prototypes.

Figure 10 shows typical profiles of the collaring pressures and of the pressure exerted by the coil against the collar pole during the assembly of magnet DC0204, as measured by the beam-type strain-gauge transducers of the strain-gauged pack. The coil stresses presented here are averaged over the four transducers of each layer. As can be seen in Figure 10, coil compression increases as vertical pressure is applied. It is maintained roughly constant during key insertion, then abruptly decreases as the collaring pressures are released. What we referred to earlier as target pre-compression is, of course, the pre-compression that remains once the collaring is completed. This level of pre-compression is achieved by appropriately sizing the pole shims; but to assemble the collared coil, the keys must be inserted, and for a given shim size—or more generally speaking, *coil package size*—the key insertion requires that the coil be compressed to a higher level than that of the target pre-compression.

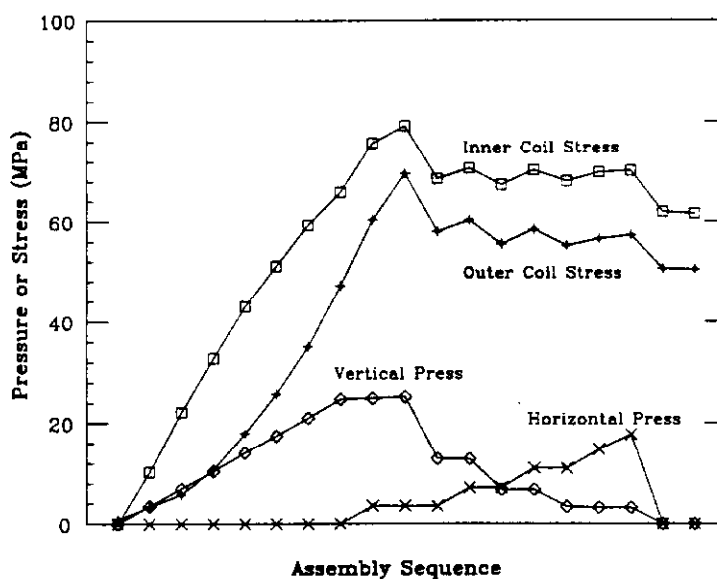


Figure 10. Collaring pressures and coil stresses during the collaring of BNL 4-cm-aperture, 17-m-long collider dipole magnet prototype DC0204. The stress data are averaged over the four coil quadrants.

3.2.2.2 Limiting the Coil Overpressure. As mentioned in the introduction, the peak pressure during collaring must be limited because it creates a risk of damaging the coil insulation. This led to the use of tapered keys.²¹ The advantage of tapered keys over squared keys is that due to their taper they can be forced into the keyways without these being perfectly aligned. In the case of square keys, both halves of the collar needed to be perfectly joined so that the keyways would be fully open before insertion of the keys. But with tapered keys, part of the horizontal driving force can be used to fully open the keyways, and thus to complete the conjunction of the collar halves. Because the keyways need not be as open as for the squared keys, less vertical pressure is required to start the key insertion, which in turn allows one to limit the peak stress seen by the coil during collaring. In the case of 4-cm SSC dipole prototypes, the maximum pressure needed to insert square keys can be as high as 140 MPa, while that to insert tapered keys can be limited to the desired 70 MPa.

Another difference between the square-key and the tapered-key techniques is that the latter permits control of the *spring back* of the collars at the time of the collaring pressure release. This spring back comes from the fact that while they are under the collaring press, the collar arms are almost stress-free (they see only a small outward bending moment resulting from the coil radial pressure); after the completion of collaring and keying, the collar arms of the keyed assembly are in tension. At the time of the collaring pressure release, the collar arms spring back from zero into tension. This effect is particularly dramatic for the square key collars which are overcompressed to fully open the keyways. It can be greatly reduced (and even eliminated) in the case of tapered keys, which can be driven against the loading surface of the collar keyway, thereby pre-tensioning and elongating the collar arms (in the elastic range) as they end up in the keyed assembly. The spring back of square key collars is typically between 25 and 35 MPa, and that of tapered key collars usually less than 15 MPa.

A last feature of the tapered-key insertion method is that as the keys load the collar keyways and complete the collar halves conjunction, they increase the clamping force on the coil. The vertical collaring pressure can then be decreased accordingly to maintain a constant coil pressure during the operation. This is clearly illustrated in Figure 10, where, as the horizontal pressure is incrementally applied, the vertical pressure is incrementally reduced, and both inner and outer layer stresses stay constant. This also helps reduce coil overpressure during collaring. In practice, a film of lead-based lubricant is applied to the tapered keys to facilitate their insertion.

3.2.2.3 Tapered Key versus Square Key Technique. As we described, the primary reason for using tapered keys is to limit coil overpressure during collaring. On the other hand, the main objection to the tapered key technique is that as the keys are inserted and force open the keyways, they can distort the keyways or become distorted themselves. This can result in non-uniformities on the vertical diameter of the collared-coil assembly along the magnet length, and thus in magnetic field distortions. On the other hand, in the case of squared keys, the complete opening of the keyways is effected by the vertical pressure, and the keys could be inserted virtually by hand. Thus there is minimal key distortion and minimal risk of non-uniformity. Later, we shall see that although the tapered key technique on earlier prototypes led to somewhat erratic distortions,²⁸ the collar deflections are now very reproducible, and there is less concern of degrading the field quality.

The most serious objection to the tapered key technique that can be envisioned is that the horizontal force used to drive the keys in also loads the coil at the midplane. This load is applied in an area where the two half-coils can slide on the midplane ground insulation, eventually causing the midplane turns to move inward. There is no easy way to prevent this from happening. One possibility is to support the coil from the inside by inserting a collaring mandrel. Such a technique was used for the fabrication the HERA magnets. In the case of the HERA dipole magnets, the collaring process had three main phases. First, the collars were pressed onto the coil with the mandrel in place and with a vertical force of about 2 MN/m. Second, the vertical force was reduced to 500 kN/m, and the collaring mandrel was extracted. And third, the collars were re-pressed with a vertical force varying from 3.5 to 4.5 MN/m, and the stainless-steel pins, which in the HERA dipole magnet design are used to lock the collar packs around the coil, were inserted through the

holes of the collars laminations. (These stainless-steel pins serve a purpose similar to that of the keys in the SSC dipole magnet design.) The application of such a collaring process to the SSC dipole magnets could eventually help reduce but not eliminate the risk of midplane turn motions. Indeed, the collaring mandrel would still have to be removed prior to key insertion—that is, prior to the application of the horizontal force, which eventually causes these motions.

3.2.3 Coil Pre-Compression Comparison

The target pre-compressions are 70 MPa for the coil inner layer, and 55 MPa for the coil outer layer at room temperature. Having described the collaring process, we now need to verify that these goals can be achieved and that the eventual fluctuations from magnet to magnet are not random.

3.2.3.1 Effective Size of Coil Package. To make cross-magnet comparisons, we need to find a sensible way to reduce the data. From what we described above, coil compression results from squeezing the coil into a cavity smaller than its size at rest. Fluctuations in the coil compression are, therefore, expected to originate from differences in the collar cavity sizes and in the size of the coil package itself (and eventually in the coil modulus). Two types of collars were used for the magnets described in this paper: round and anti-ovalized. The anti-ovalized collars have the same geometry as the round collars, except that the centers of the top and bottom collars have been shifted with respect to each other by a distance $2a = 254 \mu\text{m}$ towards the midplane. Compared to that of the round collars, the arc length of the anti-ovalized collars cavity is, therefore, reduced by $2a$, for both inner and outer layers. On the other hand, the coil package size can be calculated by adding the shim thickness and the actual quarter-coil size. An appropriate parameter for cross-magnet comparisons seems to be the parameter m , defined for each layer by

$$m = t + (s_m - s_d) \quad \text{for round collars,} \quad (7a)$$

and

$$m = t + (s_m - s_d) + a \quad \text{for anti-ovalized collars.} \quad (7b)$$

In the following, we shall refer to m as the *effective size* of the coil package.

3.2.3.2 Inner Layer Pre-Compression. Figure 11 presents summary plots of the inner coil stress versus the effective size of the inner coil package at various times of the assembly and testing of the nine magnets described in this paper. For clarity of presentation, the magnets have been divided into two series: Figure 11(a) shows the data for magnets DD0026, DD0027, DD0028, and DC0201, and Figure 11(b) shows the data for all the remaining DC-series magnets. The stresses reported here are those measured in average over the four inner-layer strain-gauge transducers; the values of m are those listed in Table 2 and are calculated from the inner coil size measurements at the axial location of the strain-gauge pack. Squares mark the peak stress during collaring, and crosses mark the stresses just after collaring; diamonds represent data just before cooldown, and circles represent data just after cooldown. In case two magnets have approximately the same coil package size, the data of one of the magnets are differentiated from that of the other by means of arrows. For magnets DD0027 and DD0028, which have two strain gauge packs, the two series of data are differentiated by means of the letters FE and RE, which refer to the locations of the strain-gauge packs with respect to the magnet ends: FE for the pack closest to the lead end, and RE for the pack closest to the return end.

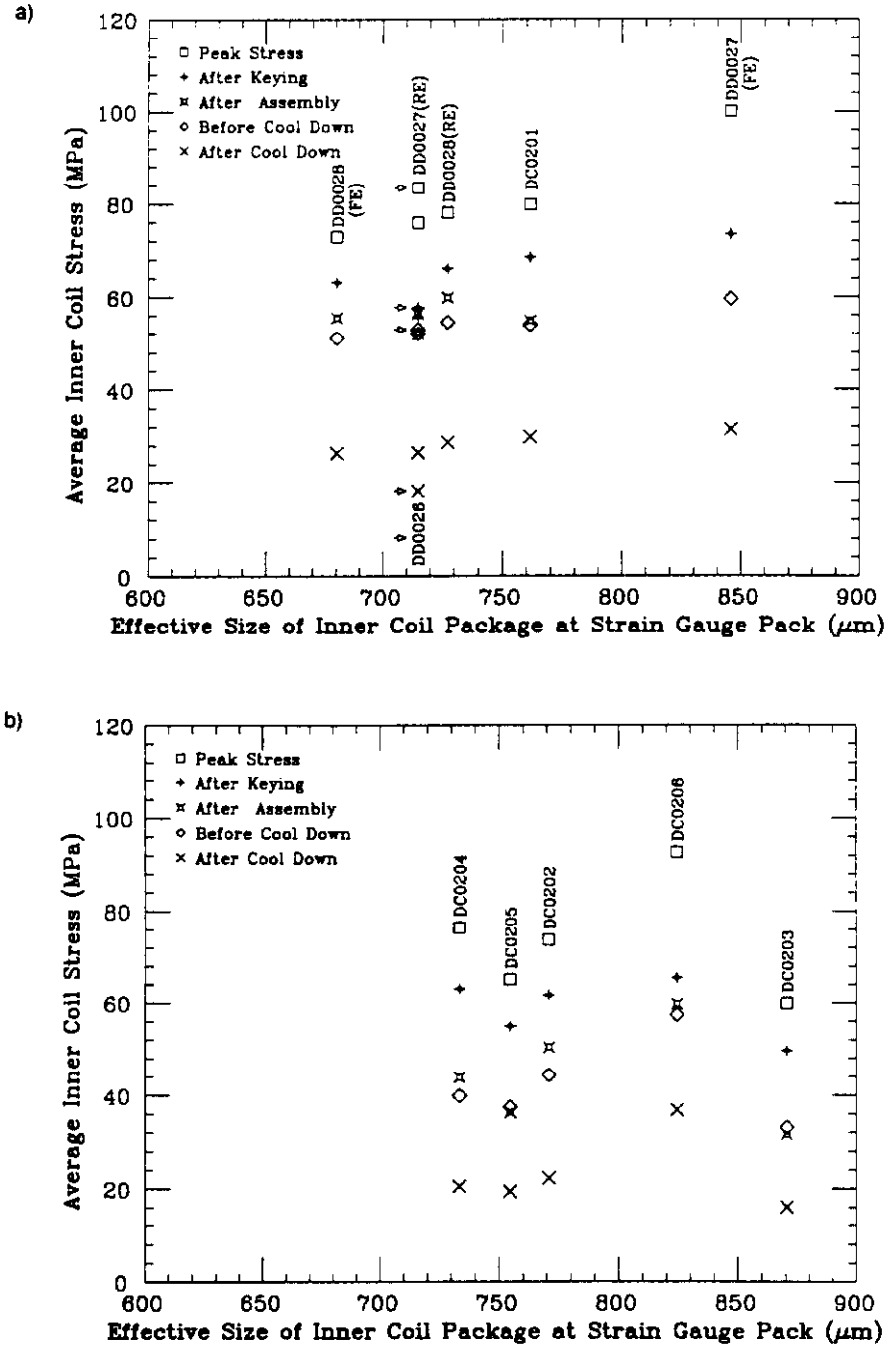


Figure 11. Summary of coil inner layer pre-compressions at various times of assembly and testing versus effective sizes of inner layer package for most recent BNL 4-cm-aperture, 17-m-long collider dipole prototypes: a) inner layer using a fiberglass wrap with an epoxy content of 24% in weight, b) inner layer using a fiberglass wrap with an epoxy content of 20% in weight. The pre-compression data are averaged over the four coil quadrants. The effective sizes of the inner layer packages are calculated at the locations of the strain-gauge packs.

Let us first comment on Figure 11(a). Three main features need to be discussed: 1) the peak stresses during collaring are all below 100 MPa; 2) there is a stress relaxation between the end of keying and the beginning of testing; and 3) despite the dispersion of the after-keying data, the before-cooldown data lie on a regular line. As described earlier, one of the main concerns during collaring is to limit the coil overpressure. The data presented in Figure 11 show that the BNL tapered-key insertion technique allows us to limit this overpressure to a reasonable level. The fact that the before-cooldown data are below the after-keying data is surprising. From what we described earlier (see paragraph 2.1.1, "Baseline Design Concepts"), we would expect the shell-welding to result in an increase of the force exerted by the yoke on the collars, and, thus, in an increase of the coil azimuthal compressive stress. In reality, it appears that during the first few days following magnet assembly the stresses relax, and the amplitude of this relaxation is larger than the stress increase resulting from shell-welding. The origin of this relaxation is not yet fully understood. The most likely cause is flow or creep of the Kapton insulation, whose yield point (69 MPa at room temperature and 3% elongation) has been locally exceeded. Micrographic observations have indeed shown that the Kapton insulation had a tendency to flow into the voids between the cable strands and at the corners of the coil, at both the pole plane and the midplane.²⁹ It is, however, remarkable that at the time of testing, the stresses have stabilized at the fairly reproducible level of 50–60 MPa, right below the yield point of Kapton. This relaxation is not desirable, of course, but it is not thought to be a problem here, since it appears reproducible. Figure 11(a) also shows the stresses after cooldown, but these data will be discussed in paragraph 4.2.2, "Review of Inner-Layer Cooldown Stress Loss Measurement."

In comparison to Figure 11(a), the data in Figure 11(b) are more scattered and do not exhibit the same clear trends. First, it is odd to find that it is the magnet with the largest inner coil package, DC0203, that achieves the lowest pre-compression level. Second, the amplitude of the stress relaxation between the after-keying data and the before-cooldown data appears to be much larger than for the magnets of Figure 11(a). This larger relaxation results in the fact that all the magnets except DC0206 end up at the time of testing with a lower stress level than that observed in Figure 11(a): around 40 MPa for magnets DC0202, DC0204, and DC0205, and as low as 30 MPa for magnet DC0203. Also, neither the before-cooldown data, nor the after-cooldown data lie on regular lines. The only known differences between the magnets in Figure 11(b) and in Figure 11(a) are (see paragraph 2.2, "Variants"): 1) the shims that were added at the tops and bottoms of the collars, and 2) the lower epoxy content of the inner conductor fiberglass wrap (the epoxy content was lowered from 24% in weight for the magnets in Figure 11(a) to 20% in weight for the magnets in Figure 11(b)). The addition of the collar-yoke shims can only increase the force exerted by the yoke on the collars, and thus can only result in an increase of coil pre-compression. On the other hand, lowering the epoxy content without changing the other parameters of the fiberglass wrap is equivalent to replacing matter with void, thus leaving more room for the Kapton to flow as well as decreasing the rigidity of the fiberglass filling. It is therefore most likely that the difference in behavior between the two series of magnets is due to the change in epoxy content. Of course, the situation depicted in Figure 11(b) is not desirable. It also demonstrates the extreme sensitivity of the mechanical properties of the coil to any change in design parameters.

3.2.3.3 Outer Layer Pre-Compression. Figure 12 presents the same kind of plots for the outer coil stress versus the effective size of the outer coil package. For clarity of presentation, the magnets have been divided into two series: Figure 12(a) presents the data for the DD-series magnets, and Figure 12(b) presents the data for the DC-series magnets. Both plots seem to follow trends similar to those of Figure 11. There is, however, one striking difference between the data in Figure 11 and the data in Figure 12: there is no apparent decrease in outer-layer stress between the time of keying and the time of testing. Even in the case of the DD-series magnets, the before-cooldown stresses appear to be higher than the after-keying stresses. This would indicate that in the case of the outer layer, the stress relaxation that eventually follows collaring is smaller than the stress increase resulting from shell-welding. In other words, there appears to be less Kapton flow or Kapton creep in the coil outer layer than in the coil inner layer. A plausible explanation for this

different behavior is that the outer layer sees much less overpressure during collaring. For instance, the peak stresses reported in Figure 12 are all below the yield point of Kapton. One can then speculate that this limited overpressure induces less Kapton flow, resulting in very little change in the coil azimuthal compressive stress.

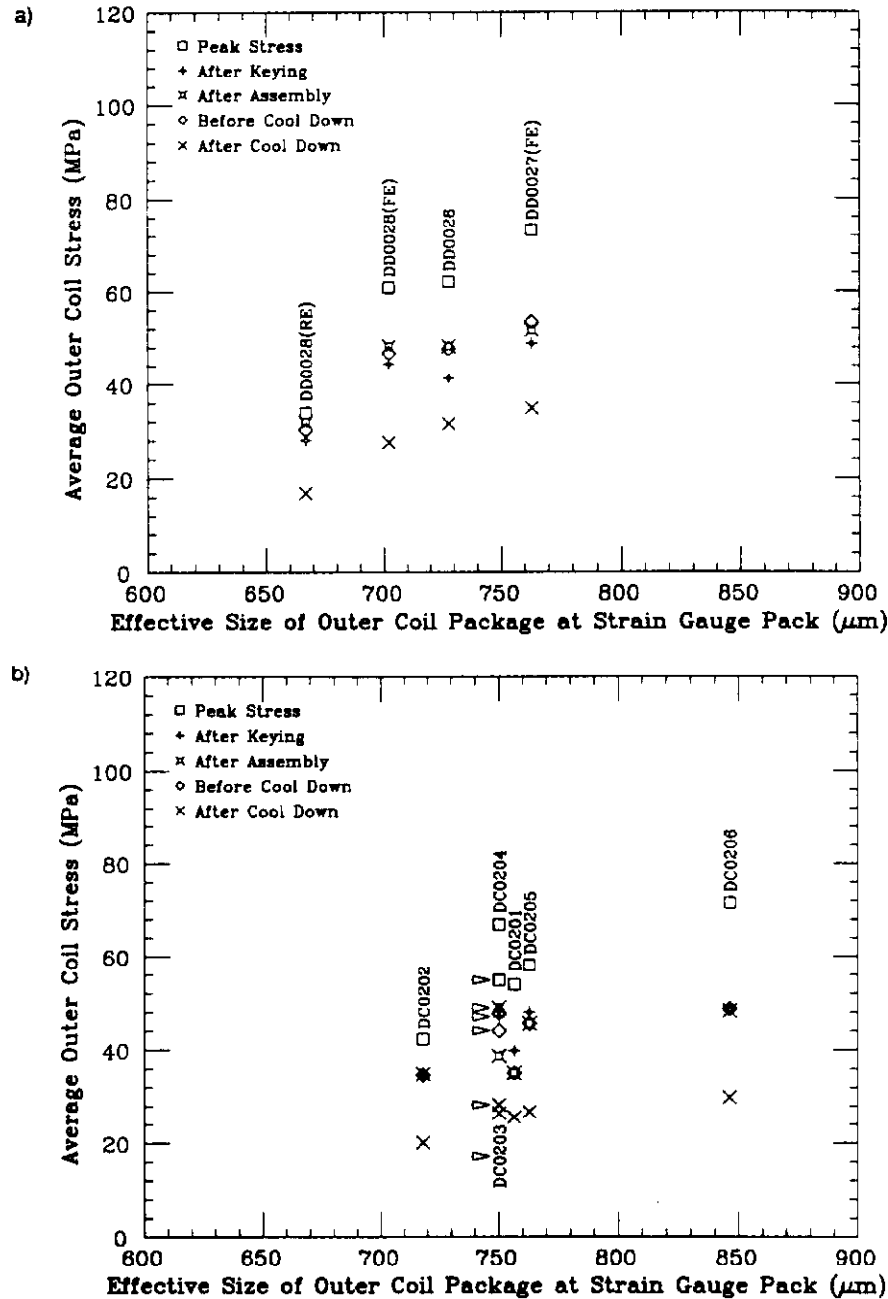


Figure 12. Summary of coil outer layer pre-compressions at various times of assembly and testing versus effective sizes of outer layer package for most recent BNL 4-cm-aperture, 17-m-long collider dipole prototypes: a) DD-series magnets, b) DC-series magnets. The pre-compression data are averaged over the four coil quadrants. The effective sizes of the outer layer packages are calculated at the locations of the strain-gauge packs.

We have deliberately separated the foregoing discussions of the inner and outer stress data. This separation is of course arbitrary, for the collars compress the two coil layers at the same time. Figure 13 shows an example of a spring model that could be used to describe the coil/collar interaction. If we wanted to be thorough, we would have to add the friction at the interface between the two coil layers and at the interface between the coil and the collars. The interdependence of the two layers could eventually explain some of the particularities observed in Figures 11 and 12. This is not, however, the place to conduct such an analysis, and we shall therefore limit ourselves to what has already been presented.

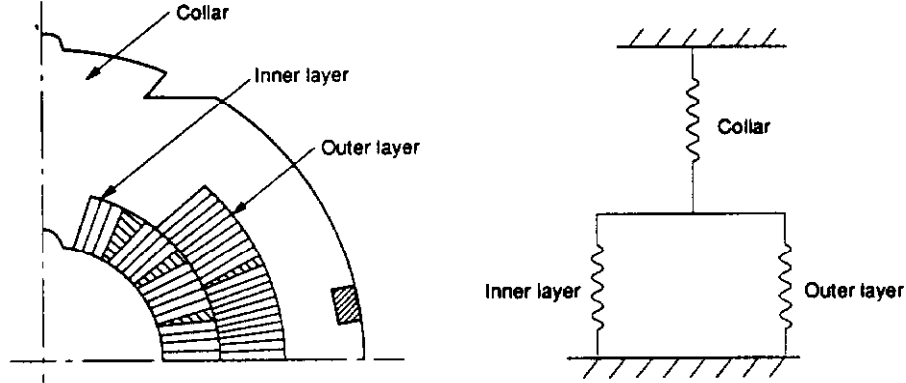


Figure 13. Spring model describing the coil/collar interaction in the collared-coil assembly of a BNL 4-cm aperture, 17-m-long collider dipole magnet prototype.

3.2.4 Collar Deflection Comparison

Having discussed the coil pre-compression, the next step is to verify that this pre-compression results in suitable and reproducible collar deflections.

Let us first define what we mean by collar deflections. A nominal collar deflection along a given axis can be defined simply as the difference between the measured diameter of the collared-coil assembly along this axis and the design inner diameter of the yoke along the same axis. There is no problem in comparing horizontal deflections of round and anti-ovalized collar magnets, because they have the same horizontal dimensions. For the vertical deflections, however, there will be an offset of amplitude $2a$. For cross-magnet comparison purposes, we shall, therefore, use for the vertical deflection an effective deflection, d_{ve} , defined by

$$d_{ve} = \text{nominal vertical deflection} \quad \text{for round collars,} \quad (8a)$$

and

$$d_{ve} = \text{nominal vertical deflection} + 2a \quad \text{for anti-ovalized collars.} \quad (8b)$$

Now, the collar deflections result from simultaneous compression of the inner and outer coil layers. The relevant parameter to do cross-magnet comparison of these deflections is, therefore, the average stress, σ_a , defined by

$$\sigma_a = \frac{\sigma_i w_i + \sigma_o w_o}{w_i + w_o}, \quad (9)$$

where σ_i and σ_o designate the inner and outer layer stress, and w_i and w_o designate the inner and outer conductor widths.

Figure 14 features a plot of the effective vertical deflections (upper data) and the nominal horizontal deflections (lower data) measured along the length of the collared-coil assembly of magnet DC0204. On average, the collared-coil assembly appears to deflect vertically outward by about $280\text{ }\mu\text{m}$, and to deflect horizontally inward by about $50\text{ }\mu\text{m}$. Figure 15 features a summary plot of the effective vertical deflection (upper data) and the nominal horizontal deflection (lower data) versus the average coil pre-compression for the nine magnets described in this paper. (The deflections are measured at the location of the strain gauge packs.) The main feature of Figure 15 is that the collar deflections appear to be relatively independent of the coil pre-compression. This is certainly true for the vertical deflections, which lie within $50\text{ }\mu\text{m}$ of each other, while the average pre-compression varies from 45 MPa to slightly more than 60 MPa. The horizontal deflections exhibit more dispersion. This dispersion, however, may be explained by the fact that different magnets were keyed with different horizontal pressures.

The fact that the collar deflections do not relate to the average stress indicates that the deformations of the collared-coil assembly are partially inelastic. This inelasticity is probably introduced by scoring of the tapered key during the keying procedure described above. However, unlike the earlier prototypes where the scoring of the keys led to erratic collar deflections,²⁸ it now appears that the collared coil can be assembled in order to produce a consistent and suitable vertical deflection, with a limited, inward horizontal deflection. These inelastic deformations are therefore no longer thought to be a problem. They can even be seen as an advantage, since to some extent they decouple the collar deflections from the azimuthal stress, thus rendering the shape of the collared-coil assembly less sensible to the mechanical properties of the coil. The reproducibility of the collar deflections demonstrated in Figure 15 is an important step in demonstrating the feasibility of the line-to-line fit design.

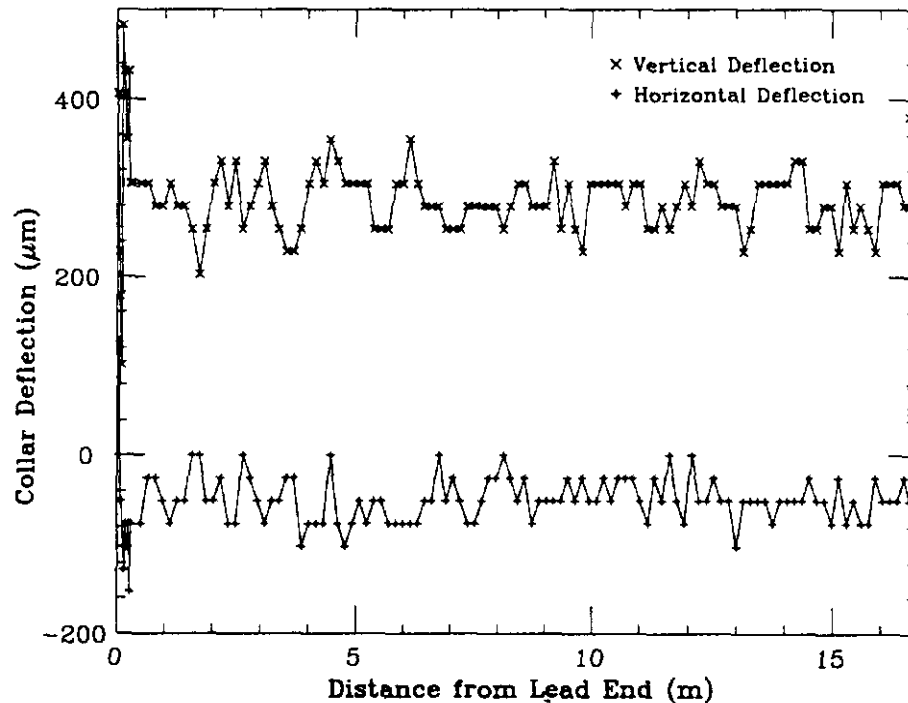


Figure 14. Effective vertical deflections and nominal horizontal deflections measured along the collared-coil assembly of BNL 4-cm-aperture, 17-m-long collider dipole magnet prototype DC0204.

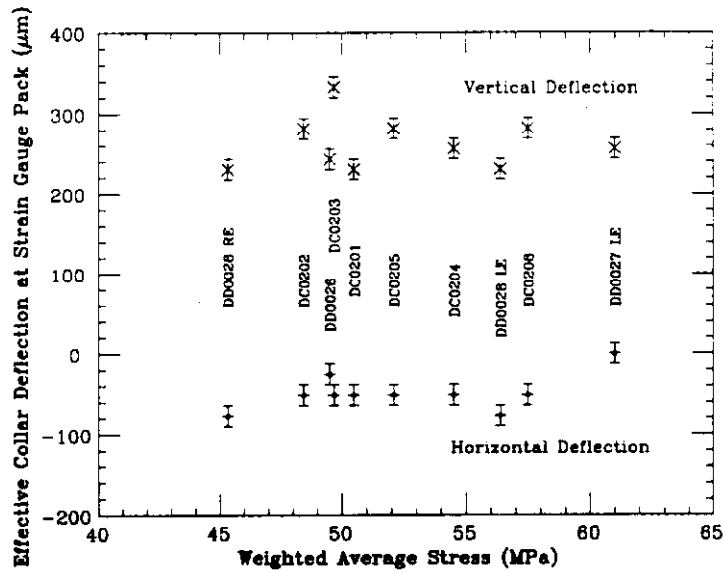


Figure 15. Summary of effective vertical collar deflections and nominal horizontal collar deflections versus average coil pre-compressions for most recent BNL 4-cm-aperture, 17-m-long collider dipole prototypes. The deflections are measured at the location of the strain-gauge packs. The pre-compression data are averaged over the four coil quadrants.

3.3 Yoke-Stacking and Shell-Welding

Yoke-stacking and shell-welding operations are straightforward. First, the bottom yoke halves are stacked and aligned on a precision plate. Alignment bars are inserted through the electrical bus slot, and tie rods are drawn through the yoke tube holes to hold the modules together (both the bars and the rods are removed at the end of shell-welding). The bottom half-shell is then assembled around the bottom yoke, and yoke and shell are rotated 180°. Next, the collared-coil assembly is laid into the bottom yoke halves and is covered with the top yoke halves and shell, as depicted in Figure 16. The two shell halves are clamped with stainless-steel clamps, called *band clamps*. These are tightened until the gaps between the two shell halves on each side of the magnets are reduced to 1.5 mm. The two halves are then tack-welded every 30 cm, and the band clamps are removed. Last, the gaps between the shell halves are filled up by two successive welding passes, called the *root pass* and the *final pass*. Welding is done manually by two welders, one on either side of the cold mass, who try to stay in step with one another, as shown in Figure 17. The welding rod material is 308L stainless steel.

As we describe throughout the paper, the key idea of the line-to-line fit design is to assemble the collared coil so that it will interfere with the yoke on the vertical diameter. The first step in verifying that this interference occurs is to measure the collar deflections. The second step is to verify that a gap remains between the two yoke halves after they are placed around the collared coil assembly. On the other hand, as we also described earlier (see paragraph 2.1.4, "Yoke and Shell"), a gap at the yoke midplane is undesirable in the cold state because it could eventually alter the rigidity of the support against the radial component of the Lorentz force. A conservative solution to this problem is to ensure that the yoke gap is closed at room temperature by the end of shell-welding. The closure of the yoke gap is thus monitored throughout the welding process through small openings of a few centimeters, left every 2 m along the welding path to allow insertion of feeler gauges.



Figure 16. Yoke-stacking operation on a BNL 5-cm-aperture, 15-m-long collider dipole magnet prototype. The operation is similar on a 4-cm-aperture prototype.

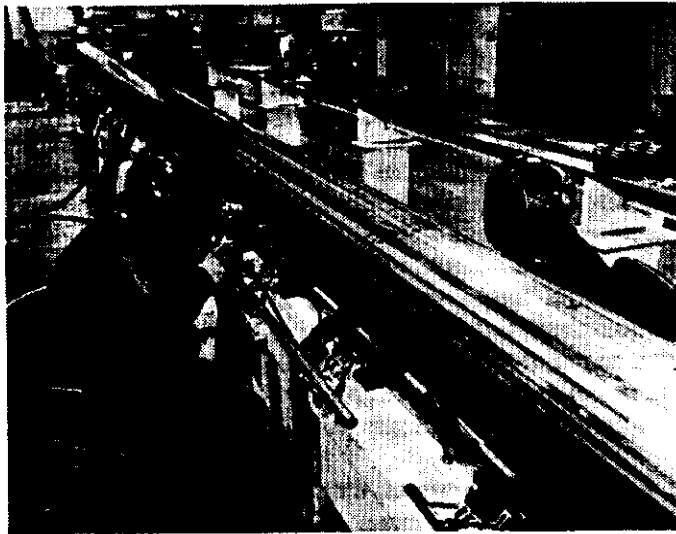


Figure 17. Shell-welding operation on a BNL 5-cm-aperture, 15-m-long collider dipole magnet prototype. The operation is similar on a 4-cm-aperture prototype.

Table 3 presents a summary of the yoke gap history during shell-welding of some of the magnets described in this paper (the values are averaged over all measurements, on both sides of the cold mass). It can be seen that for the DD-series magnets, which use round collars, a small gap remains after the shell-welding. It was to correct for this gap that anti-ovalized collars were designed. Indeed, magnet DC0201, which was the first magnet to use anti-ovalized collars, shows no gap at the yoke midplane. In the case of DC0201, however, the gap appears to be closed from the beginning of assembly. This raises the question of whether there is an adequate yoke-collar interference on the vertical diameter. It is to resolve this uncertainty that shims were added at the top and bottom of the collared coil assemblies of the subsequent DC-series magnets. The data for magnets DC0204 and DC0205 show that the combination of anti-ovalized collars and collar-yoke

shims produces the desired effect on the yoke midplane gap: it is wide open at the beginning of yoke assembly, ensuring the existence of a yoke-collar interference, and it is closed by the end of shell-welding, providing the best assurance that it will stay closed throughout cooldown and energization. The yoke midplane gap can thus be controlled, and it can be verified during assembly that it is correctly open or closed. These two facts constitute another step in demonstrating the feasibility of the line-to-line fit design.

Table 3. Average Yoke Gap History During the Shell Welding of Most Recent BNL 4-cm-Aperture, 17-m-Long Collider Dipole Prototypes (in μm).

Magnet	Pre-Tack	Tack	Root	Final
DD0027	270	140	90	50
DC0201	0	0	0	0
DC0204	250	160	90	0
DC0205	330	150	50	0

3.4 End Plates

The last phase of the assembly is mounting of the end plates and setting of the screws, which load the coil ends axially. The first screws to be mounted are those of the return end, which contain the bullet gauge assemblies. The four set screws are tightened until the bullet gauges register the desired axial pre-load. The torque value needed to reach this pre-load is noted, so that the screws at the other end of the magnet, which does not contain bullet gauge assemblies, can be tightened to the same torque value. (The setting of the additional yoke set screws mounted on the end plates of magnets DD0026 and DD0027 was not recorded.)

The first column of Table 4 summarizes the total axial pre-loads (summed over the four bullet gauges) as measured at the end of the assembly of the nine magnets described in this paper. The pre-load setting for the DD-series magnets and magnet DC0204 was 4.5 kN total. On subsequent magnets, the setting was increased in order to compensate for the unexpectedly large loss observed during cooldown (see paragraph 4.3, "Change in Coil Axial Pre-Load During Cooldown"). It was raised to 7.5 kN on magnets DC0201 and DC0202. It reached 9.5 kN on magnets DC0203 and DC0205. Finally, magnet DC0206 was set to 35 kN.

Table 4. End Force Measurements After Assembly and Before Cooldown on Selected BNL-Built, 4-cm-Aperture, 17-m-Long Collider Dipole Magnet Prototypes.

Magnet	After Assembly (kN)	After Mounting on Test Stand (kN)
DD0026	4.6	8.3
DD0027	5.0	11.2
DD0028	4.4	14.6
DC0201	7.5	6.8
DC0202	7.9	14.0
DC0203	9.5	16.4
DC0204	4.9	8.6
DC0205	9.9	12.7
DC0206	35.9	45.2

The second column of Table 4 lists the total end-force registered by the bullets just before cooldown of these magnets, after they have been mounted on the test stand. Although these measurements are taken at room temperature and before any exercise of the magnets, the values appear widely spread and 2-to-3 times higher than they were at the end of assembly. The reason for this increase has not yet been fully investigated, but it is probably related to shrinkage effects induced by the welding of the bonnet (see paragraph 2.1.5, "End Parts") to the so called *single-phase bellows* of the test stand. (The bellows connect the magnet cold mass to the *end can* of the test stand for He distribution.) Of course, these erratic changes are not desirable. However, they are not thought to be a problem for the cold-testing of the magnets, because they all correspond to an increase of axial pre-load. As long as this increase is limited and does not create a risk of shorts at the coil ends, it can only improve the axial support of the coil.

3.5 Summary

In this section, we reviewed the fabrication processes of the nine most recent BNL 4-cm-aperture, 17-m-long SSC dipole prototypes. For each step of the fabrication (coil winding and curing, collaring, yoke-stacking and shell-welding, and mounting of end plates), we discussed the parameters that need to be controlled (coil size, coil azimuthal pre-compression, collar deflections, yoke midplane gap, and coil axial pre-load), and we compared their values for the nine magnets. Although it appears that the level of the coil pre-compression achieved for the magnets using a fiberglass wrap with an epoxy content of 20% in weight is lower than expected, and although the coil axial pre-load appears to be dramatically affected by the welding of the magnets on the test stand, the assembly data are coherent and in line with the design concepts that were developed. Especially, it appears that the vertical collar-yoke interference, which is the cornerstone of the line-to-line fit design, can be controlled and can be made reproducible from magnet to magnet. Having discussed the magnet assembly, the next step is to see whether these satisfactory data translate into the expected mechanical behavior during cold-testing.

4 MAGNET COOLDOWN

4.1 Introduction

The first important step after magnet assembly is cooldown from room temperature to LHe temperature. During cooldown, the various parts that constitute the magnet shrink with different thermal expansion coefficients. In the azimuthal direction, the coil is expected to shrink more than the stainless-steel collars. In the radial direction, collars made of Nitronic-40 stainless steel shrink more than the iron yoke, while High-Manganese steel collars shrink less. And last, in the axial direction, the coil is expected to contract less than the outer steel shell, which, in turn, is expected to shrink more than the supposedly monolithic iron yoke. These thermal shrinkage differentials result in changes in coil azimuthal compressive stress and coil axial loading. If not controlled, they can lead to a situation where the coil is not sufficiently supported during excitation. Also, as there are large frictional forces involved, some parts of the magnet cold mass can be prevented from shrinking as much as they would, resulting in stress lock-ups. There is then a risk that these stress lock-ups could be released during excitation, leading to heat dissipation and unexpected quenches.

In this section, we shall attempt to summarize the cooldown data from the nine magnets considered in this paper. The data reported here are those measured by the two types of strain gauges described in paragraph 2.3, and which are monitored throughout cooldown by a slow data logger system. However, the strain gauges themselves are very sensitive to temperature.^{16,30,31} To convert the gauge outputs into stress or force, we therefore need to use calibrations at the corresponding temperature. In practice, the gauges are calibrated only at room temperature and LHe

temperature. The stress or force can thus be accurately computed only at these two temperatures. We shall therefore limit our analyses to the before- and after-cooldown values, and we shall not consider the intermediate temperatures. The section will be divided into two paragraphs, in which we shall successively discuss the change in coil azimuthal compressive stress and the change in coil axial loading. First, we shall try to predict the sign and amplitude of the change, and then we shall review the actual data. As we did for the assembly, we shall try to determine if the cooldown data are reproducible from magnet to magnet, and, if they are not, we shall try to explain the differences and to find correlations with specific magnet features.

4.2 Change in Coil Azimuthal Compressive Stress During Cooldown

4.2.1 Predicting the Cooldown Stress Loss

Three effects have to be taken into consideration to estimate the change in coil azimuthal compressive stress during cooldown: 1) the thermal shrinkage differential between the coil and the collars in the azimuthal and radial directions, 2) the thermal shrinkage differential between the collar and the yoke steels in the radial direction, and 3) the non-linearity and temperature dependence of the coil mechanical properties. Let us first discuss these three effects, then estimate the cooldown stress loss.

4.2.1.1 Thermal Shrinkage Differential Between Coil and Collars. The thermal expansion coefficient of the coil in the azimuthal direction, integrated between room temperature and LHe temperature, α_c , was measured to be 4.5×10^{-3} , compared to 3.0×10^{-3} for Nitronic-40 stainless steel, and 1.7×10^{-3} for High-Manganese stainless steel.³² During cooldown, the coil thus shrinks more than the collars. This shrinkage differential results in an apparent increase of the arc length of the collar cavity, Δl_1 . An upper limit of the increase, Δl_{1m} , can be estimated by assuming that there are no frictional forces between the coil inner layer and coil outer layer, and between the coil outer layer and the collars. This upper limit is expressed as

$$\Delta l_{1m} = (\alpha_c - \alpha_{ss}) l_0 \quad , \quad (10)$$

where α_{ss} is the thermal expansion coefficient of the collar steel, integrated between room temperature and LHe temperature, and l_0 is the arc length of the collar cavity at room temperature ($l_0 = 64.3$ mm for the coil inner layer, and $l_0 = 55.4$ mm for the coil outer layer).

Typically,

$$\frac{\Delta l_{1m}}{l_0} = 1.5 \times 10^{-3} \quad \text{for Nitronic-40 steel collar magnets, and}$$

$$\frac{\Delta l_{1m}}{l_0} = 2.8 \times 10^{-3} \quad \text{for High-Manganese steel collar magnets.}$$

In the absence of friction, the apparent increase of the arc length of the collar cavity resulting from the thermal shrinkage differential between the coil and the collars is thus expected to be 87% larger for High-Manganese steel collar magnets than for Nitronic-40 steel collar magnets.

4.2.1.2 Thermal Shrinkage Differential Between Collar and Yoke Steels. At room temperature, the magnet is assembled in such a way that there is a perfect fit between the outer surface of the collared-coil assembly and the inner surface of the yoke. However, the thermal expansion coefficient of the yoke low-carbon steel, integrated between room temperature and LHe temperature, was measured at 2.0×10^{-3} , compared to 3.0×10^{-3} for Nitronic-40 stainless steel,

and 1.7×10^{-3} for High-Manganese stainless steel.³² Thus, during cooldown, the iron yoke shrinks differently from the collars. This thermal shrinkage differential will influence the collar-yoke fit, eventually resulting in a change of the shape of the collared-coil assembly.

Let us first consider the case of the Nitronic-40 steel collars magnet. During cooldown, the inner diameter of the iron yoke is expected to become larger than the outer diameter of the collars. As it shrinks away, the yoke leaves some room for the collared-coil assembly to spring back along the vertical diameter and to assume the oval shape it had prior to yoke-stacking. If we assume that the yoke midplane gap is always closed, the spring-back is accompanied by a stretching of the collar cavity, eventually resulting in a decrease of the coil azimuthal compressive stress. An upper limit of the increase in arc length of the collar cavity resulting from the thermal shrinkage differential between the yoke and collar steels, Δl_{2m} , can be estimated by assuming that there is no loss of vertical contact, and no frictional forces between the collars and the yoke. So we have

$$\Delta l_{2m} = (\alpha_{ss} - \alpha_y) d_y \quad \text{for Nitronic-40 steel collars,} \quad (11a)$$

where α_y is the thermal expansion coefficient of the yoke low-carbon steel, integrated between room temperature and LHe temperature, and d_y is the inner diameter of the yoke at room temperature ($d_y = 110.8$ mm).

Typically,

$$\frac{\Delta l_{2m}}{l_0} = 1.7 \times 10^{-3} \quad \text{for coil inner layer, and}$$

$$\frac{\Delta l_{2m}}{l_0} = 2.0 \times 10^{-3} \quad \text{for coil outer layer.}$$

For Nitronic-40 steel collar magnets, the effect of spring-back of the collared-coil assembly inside the yoke, due to the thermal shrinkage differential between the collars and the yoke in the radial direction, is thus expected to be 13 to 33% larger than the effect of the thermal shrinkage differential between the coil and the collars in the azimuthal direction

Let us now consider the case of High-Manganese steel collar magnets. During cooldown, the iron yoke is expected to shrink more than the collared-coil assembly. If, at room temperature, we started with a perfect fit between the outer surface of the collared-coil assembly and the inner inner surface of the yoke, the differential thermal shrinkage results in an increase of the radial pressure exerted by the yoke onto the collars. This increase in radial pressure is eventually supported by the collared-coil assembly, and the outer radius of the collared-coil assembly is reduced. A reduction in radius results in an apparent decrease of the arc length of the collar cavity, causing the coil azimuthal compressive stress to increase. An upper limit of the decrease in arc length of the collar cavity resulting from the thermal shrinkage differential between the yoke and collar steels, Δl_{2m} , can be estimated by assuming that the yoke midplane gap is always closed and that the yoke is infinitely stiff. It is expressed as

$$\Delta l_{2m} = (\alpha_{ss} - \alpha_y) l_0 \quad \text{for High-Manganese steel collars.} \quad (11b)$$

Typically,

$$\frac{\Delta l_{2m}}{l_0} = -0.3 \times 10^{-3} \quad \text{for both inner and outer layers.}$$

For High-Manganese steel collar magnets, the thermal shrinkage differential between the collars and the yoke in the radial direction is thus expected to partially compensate for the large thermal shrinkage differential between the coil and the collars in the azimuthal direction.

4.2.1.3 Non-Linearity and Temperature Dependence of the Coil Mechanical Properties. Typical stress-strain curves, measured on straight stacks of SSC-type conductors, can be found in References 26, 33, and 34. The data in Reference 33 are for conductor stacks using the Kapton-fiberglass insulation scheme described in this paper (see paragraph 2.1.2); the data in References 26 and 34 are for conductor stacks using a *whole* Kapton insulation scheme (with no fiberglass wrap). However, the measurements for the two kinds of insulation are in good qualitative agreement, and can be summarized as shown in Figure 18. Let us first comment on the room-temperature curve. It appears that there is a large hysteresis between the loading branch of the curve (top) and the unloading branch of the curve (bottom). It also appears that both the loading and unloading branches of the hysteresis are non-linear, and that in the pressure range of interest ($10 < \sigma \leq 70$ MPa), they can be fitted by a second-order polynomial. Let us now comment on the liquid nitrogen (LN_2) temperature curve. It first appears that the LN_2 curve lies above the room temperature curve, indicating an increase in coil stiffness. There is still an hysteresis between the loading and unloading branches of the curve, but the amplitude of the hysteresis is lower than at room temperature. And finally, as was also the case at room temperature, both the loading and unloading branches of the hysteresis are non-linear and can be fitted by a second-order polynomial. It thus appears that at any temperature, both the loading and the unloading branch of the coil stress-strain curve can be fitted by a relation of the form:

$$\sigma = A(T) \epsilon^2 + B(T) \epsilon + C(T) \quad \text{for } \sigma, 10 \leq \sigma \leq 70 \text{ MPa,} \quad (12)$$

where σ and ϵ designate the coil stress and strain, and A , B , and C are three temperature-dependent parameters. (In theory, the C coefficient should be zero, but in practice, the zero-deformation position of an experimental set-up is never known accurately. The measurements are thus only reliable above a certain level of deformation. Hence, when fitting the experimental data, the points near zero-strain are excluded, and the fitting polynomial can end up with a non-zero C coefficient.)

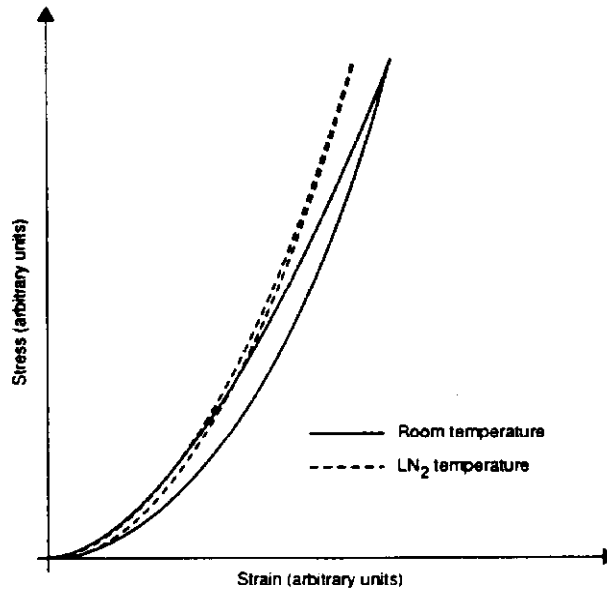


Figure 18. Typical stress-strain curves measured on a straight stack of SSC-type insulated conductors at room and LN_2 temperatures.

Having explained how the coil mechanical properties are expected to vary, the next step would be to put numbers on the coefficients A , B , and C . (Note that for estimating the cooldown changes, we are interested only in the unloading branch of the stress-strain curve.) The problem, however, is that there are very few low-temperature data available. The experiments carried out in References 26 and 34 were purely qualitative, and the only low-temperature measurements presented in Reference 33 were performed on a stack of outer-layer conductors. To proceed, then, we need to make some assumptions. The outer layer conductor data of Reference 33 show that for the unloading branch of the stress-strain curve, the LN_2 curve is not that much different from the room-temperature curve. In the following, we shall therefore neglect the influence of temperature, and take for A , B , and C their room-temperature values. By fitting in the range $10 \text{ MPa} \leq \sigma \leq 70 \text{ MPa}$ the unloading branch of the room-temperature stress-strain curves given in Reference 33, we obtain for the coil inner layer:

$$A = 1.1 \times 10^6 \text{ MPa}, \quad B = -5100 \text{ MPa}, \quad \text{and} \quad C = 15.0 \text{ MPa},$$

and for the coil outer layer:

$$A = 1.1 \times 10^6 \text{ MPa}, \quad B = -3400 \text{ MPa}, \quad \text{and} \quad C = 8.0 \text{ MPa}.$$

4.2.1.4 Stress Loss Computation. Having discussed the three effects to be considered, we can now go back to the stress-loss computation. Let ϵ_w and ϵ_c designate the coil strain at room temperature and LHe temperature. If we assume that there are no frictional forces, the change of stress during cooldown, $\Delta\sigma_c$, can be estimated as

$$\Delta\sigma_c = \sigma(\epsilon_c) - \sigma(\epsilon_w) \quad . \quad (13)$$

Combining Eqs. (12) and (13), and assuming that the parameters A , B , and C do not depend on the temperature yields,

$$\Delta\sigma_c = A \Delta\epsilon_c (2 \epsilon_w + \Delta\epsilon_c) + B \Delta\epsilon_c \quad , \quad (14)$$

where $\Delta\epsilon_c$ is the change in coil strain during cooldown.

The room temperature strain, ϵ_w , can easily be derived from the room temperature stress, σ_w , by using Eq. (12). It is expressed as

$$\epsilon_w = \frac{-B + \sqrt{B^2 - 4A(C - \sigma_w)}}{2A} \quad . \quad (15)$$

Combining Eqs. (14) and (15) yields

$$\Delta\sigma_c = 2\sqrt{A} \Delta\epsilon_c \sqrt{\sigma_w + \frac{B^2 - 4AC}{4A}} + A \Delta\epsilon_c^2 \quad , \quad (16)$$

for

$$10 \text{ MPa} \leq \sigma_w + \Delta\sigma_c \quad \text{and} \quad \sigma_w \leq 70 \text{ MPa} \quad .$$

With the parameter values given above, we obtain for the coil inner layer:

$$\Delta\sigma_c = 2.1 \times 10^6 \Delta\epsilon_c \sqrt{\sigma_w - 9.1 \times 10^6} + 1.1 \times 10^{12} \Delta\epsilon_c^2 ,$$

and for the coil outer layer:

$$\Delta\sigma_c = 2.1 \times 10^6 \Delta\epsilon_c \sqrt{\sigma_w - 5.4 \times 10^6} + 1.1 \times 10^{12} \Delta\epsilon_c^2 .$$

It thus now remains to estimate $\Delta\epsilon_c$.

From what we previously calculated, the change in strain during cooldown, $\Delta\epsilon_c$, is given by

$$\Delta\epsilon_c = -\frac{\Delta l_1}{l_0} - \frac{\Delta l_2}{l_0} , \quad (17)$$

where Δl_1 is the change in arc length of the collar cavity resulting from the thermal shrinkage differential between the coil and the collars, and Δl_2 is the change in arc length of the collar cavity resulting from the thermal shrinkage differential between the collars and the yoke. Neither Δl_1 nor Δl_2 can be calculated accurately because of unknown frictional forces at the various interfaces of the system. However, in either case, an upper limit of the absolute value of the change can be estimated. Combining these upper limits thus enables us to determine an upper limit of the change in strain during cooldown, $\Delta\epsilon_{cm}$. From Eqs. (10), (11), and (17), we see that

$$\Delta\epsilon_{cm} = -\frac{\Delta l_{1m}}{l_0} - \frac{\Delta l_{2m}}{l_0} = -(\alpha_c - \alpha_{ss}) - (\alpha_{ss} - \alpha_y) \frac{d_y}{l_0}$$

for Nitronic-40 steel collars, and (18a)

$$\Delta\epsilon_{cm} = -\frac{\Delta l_{1m}}{l_0} = -(\alpha_c - \alpha_{ss}) \quad \text{for High-Manganese steel collars.} \quad (18b)$$

Introducing these expressions of $\Delta\epsilon_{cm}$ into Eq. (16) allows us to determine an upper limit of the change of stress cooldown, $\Delta\sigma_{cm}$.

To compare with these maximum values, it is interesting to consider two other limiting cases. For the Nitronic-40 steel collar magnets, it is the change in stress calculated with the assumption that there is no spring-back of the collared-coil assembly inside the yoke. This change is expressed as

$$\Delta\epsilon_c = -\frac{\Delta l_{1m}}{l_0} = -(\alpha_c - \alpha_{ss}) . \quad (19a)$$

For the High-Manganese steel collar magnets, it is the change in stress calculated after taking into account the increase of radial pressure on the collared-coil assembly due to the larger thermal expansion coefficient of the yoke. We have

$$\Delta\epsilon_c = -\frac{\Delta l_{1m}}{l_0} - \frac{\Delta l_{2m}}{l_0} = -(\alpha_c - \alpha_{ss}) . \quad (19b)$$

The continuous and dashed lines of Figure 19 present the plots of the maximum cooldown stress losses for the coil inner layer of Nitronic-40 and High-Manganese steel collars magnets, as calculated by combining Eqs. (16) and (18). The continuous and dashed lines of Figure 20 present the same plots for the coil outer layer. The dotted and dot-dashed lines of both Figures 19 and 20

present the plots of the expected cooldown stress losses as calculated by combining Eqs. (16) and (19). It appears that due to the quadratic form of Eq.(12), $\Delta\sigma_c$ is expected to decrease quasi-linearly with increasing σ_w . It also appears that due to the eventual large spring-back of the collared-coil assembly inside the yoke, Nitronic-40 steel collar magnets have the potential to lose more pre-compression during cooldown than High-Manganese steel collar magnets.

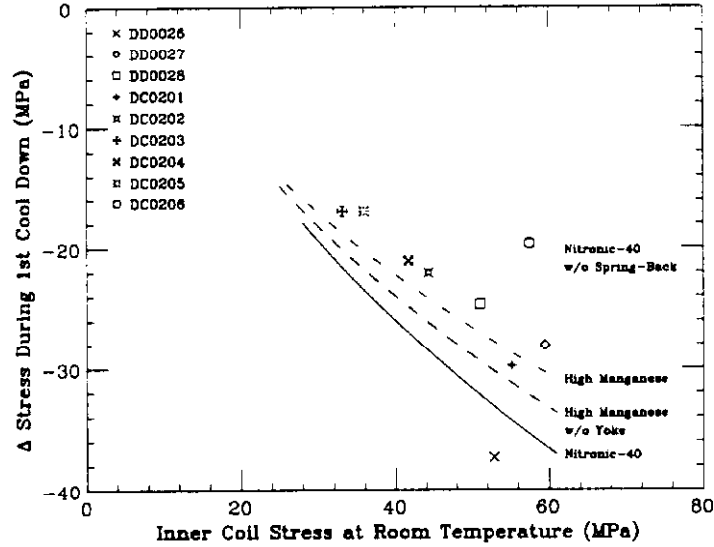


Figure 19. Changes in the azimuthal pressure exerted by the coil inner layer against the collar pole during the first cooldowns of the most recent BNL 4-cm-aperture, 17-m-long collider dipole magnet prototypes as a function of the before-cooldown pressures. The pressure data are averaged over the four coil quadrants. The various lines represent analytical predictions.

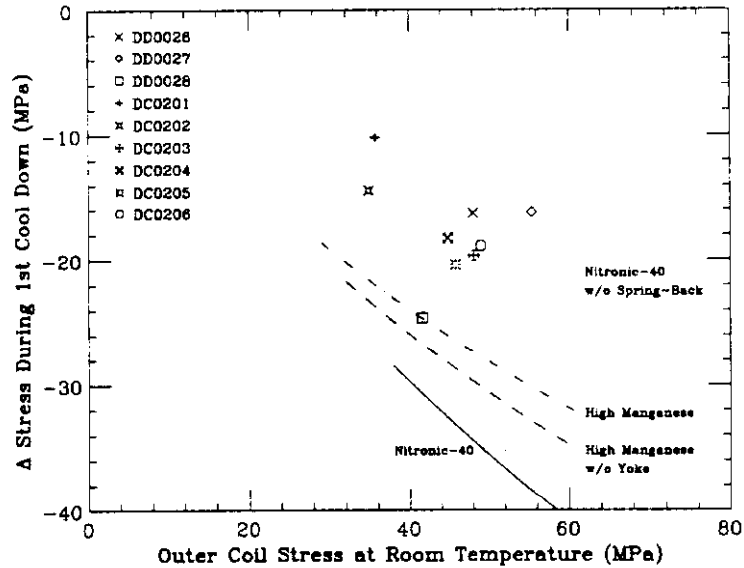


Figure 20. Changes in the azimuthal pressure exerted by the coil outer layer against the collar pole during the first cooldowns of the most recent BNL 4-cm-aperture, 17-m-long collider dipole magnet prototypes as a function of the before-cooldown pressures. The pressure data are averaged over the four coil quadrants. The various lines represent analytical predictions.

4.2.2 Review of Inner Layer Cooldown Stress Loss Measurements

The stress values before and after the first cooldown of the nine magnets described in this paper are summarized in Table 5a. Figure 19 presents a summary plot of the cooldown stress losses as a function of the before cooldown stresses, while Figures 11 shows the room temperature and LHe temperature stresses as a function of the effective sizes of the coil inner-layer package.

Table 5a. Summary of Average Inner Coil Stress Measurements on Selected BNL-Built, 4-cm-Aperture, 17-m-Long Collider Dipole Magnet Prototypes.

Magnet	After Keying (MPa)	After Assembly (MPa)	Before First Cooldown (MPa)	After First Cooldown (MPa)	Before First Warm-up (MPa)	Initial Stress vs. I^2 Slope ^a (MPa/kA ²)	Unloading Current (A)	Warm Collar-Yoke Interference ^b (μ m)	Cold Collar-Yoke Interference ^b (μ m)
DD0026	57.8	56.3	52.9	15.6	20.7	.52	-6500	241	274
DD0027 ^c	73.3		59.5	31.4	29.9	.69	>7200	254	143
DD0028 ^c	66.1	55.5	51.1	26.4	25.5	.71	-7200	229	118
DC0201	68.5	53.7	55.2	25.4	33.3	1.12	-6500	51	-60
DC0202	50.4	44.2	44.3	22.2	22.8	.83	-6500	177	66
DC0203	31.6	31.6	33.1	16.1	19.0	.72	-6000	228	117
DC0204	43.9	41.0	41.7	20.6	24.1	.81	-6500	152	41
DC0205	36.3	36.1	35.9	18.9	19.8	.74	-6000	177	76
DC0206	59.8	59.8	57.5	36.8	34.4	.99	-7300	177	76

^a On average over selected strain gauge runs from the first and second testing cycles.

^b Estimated at the axial location of the strain-gauge pack.

^c At the feed-end pack.

The main features of Figure 19 are: 1) all the Nitronic-40 steel collar magnets but one (magnet DC0206) lie approximately on the same line, and this line is parallel to that computed using the combination of Eqs. (16) and (18a), and 2) the High-Manganese steel collar magnet (magnet DD0026) lies below the line; that is, it has apparently lost more pre-compression than the Nitronic-40 steel collar magnets. Let us first comment on the Nitronic-40 steel collar magnets. The fact that the cooldown stress losses measured on all but one of these magnets increase quasi-linearly with increasing room-temperature stress is a confirmation that, in the pressure range of interest, the coil stress-strain curve has the quadratic form suggested by Eq. (12). The fact that the line defined by these magnets lies above, and is parallel to, the line computed by using Eqs. (16) and (18) is also quite satisfactory, especially if one considers that we neglected the influence of temperature on the coil stress-strain curve, and that, to parameterize the room-temperature curve, we used data that were taken in a relatively crude experiment. The data in Figure 19 thus show that for a first-cut estimation of the cooldown stress loss, a fit of the unloading branch of the room-temperature stress-strain curve is good enough. There is yet no clear explanation of why magnet DC0206 behaves differently from the other magnets. As we shall see in paragraph 5.2.2, it also exhibits a peculiar behavior during excitation. The peculiarity of the stress measurements during both cooldown and excitation leads us to suspect that something was wrong with the mounting of the strain gauge pack itself.

Let us now comment on the High-Manganese steel collar magnet. From the change in strain calculated in paragraph 4.2.1.4, we would have expected the negative thermal shrinkage differential between the coil and the collars to be partially offset by the positive thermal shrinkage

differential between the collars and yoke steel, thus eventually resulting in a smaller cooldown stress loss than for the Nitronic-40 collar magnets. The data in Figure 19 show that such is not the case. It also appears that, unlike the Nitronic-40 steel collar magnets, magnet DD0026 lies below the maximum cooldown stress-loss curve computed by using the combination of Eqs. (16) and (18b). The *measured* cooldown stress loss on the High-Manganese steel collar magnet thus appears to be larger than expected. One possible explanation for this discrepancy is that it is introduced by the measuring technique. In other words, we suspect that in the case of the High-Manganese steel collar magnet, the mounting of the inner-layer beam-type strain-gauge transducers amplifies the cooldown stress loss. Indeed, for the inner layer, the whole pole part of the collar laminations supporting the beam is cut in order to host a solid and accurately EDM'd stainless-steel base. However, the stainless steel used for the base and the beam is A286, whose thermal expansion coefficient, integrated between room temperature and LHe temperature, was measured to be 2.9×10^{-3} .³² The base supporting the transducer, and the transducer itself, thus shrink more than the pole part of the adjacent High-Manganese steel collars, resulting, at LHe temperature, in a parallel misalignment of the face of the beam with respect to the pole face of the adjacent collars (the angle of the beam is not expected to change). Studies have shown that such parallel misalignment could eventually result in relatively large errors in the stress measurements. To determine whether the excessive shrinkage of the strain-gauge transducer mounting base is really the cause of the larger loss measurement would require further experimentation. Having no more experimental facts available, we shall therefore limit ourselves to the conclusion that for the High-Manganese steel collar magnet of Figure 19, there are some questions about the reliability of the measurements.

Let us now go back to Figure 11. In paragraph 3.2.3.2, we divided the nine magnets of this paper into two series. The first series included magnets DD0026, DD0027, DD0028, and DC0201. They were characterized by the fact that their before-cooldown stresses exhibited a linear correlation with their coil inner-layer package sizes. The second series included magnets DC0202 and following, and was characterized by the fact that their before-cooldown stresses were lower than for the first series of magnets, and they exhibited a much weaker correlation with their coil inner-layer package sizes. The data in Figure 11(a) show that with the exception of magnet DD0026, the after-cooldown stresses for the magnets of the first series also lie on a regular line. (The fact that magnet DD0026 lies below the line is consistent with the observation made in Figure 19 that the High-Manganese steel collar magnet seemed to lose more azimuthal compressive stress during cooldown than the Nitronic-40 steel collar magnets.) The data of Figure 11(a) indicate that if magnets are assembled in a reproducible way, they end up after cooldown with a reproducible level of coil azimuthal pre-compression. On the other hand, if there are fluctuations in the way they are assembled, we are not surprised to find, as in Figure 11(b), that they end up after cooldown with inconsistent levels of pre-compressions. It is, nevertheless, comforting that the fluctuations in the room-temperature pre-compressions of the second-series magnets do not jeopardize the correlation observed in Figure 19. In other words, even though the room-temperature pre-compressions are not consistent, the cooldown losses are reproducible and are consistent with those of the first-series magnets.

4.2.3 Review of Outer Layer Cooldown Stress Loss Measurements

The cooldown data for the outer layer of the nine magnets described in this paper are summarized in Table 5b and on Figure 20. The changes during cooldown appear more erratic than for the inner layer, and they do not follow the same magnet-to-magnet pattern. Two reasons can be found to explain this more erratic behavior: 1) the outer-layer strain gauge measurements may be less reliable than those of the inner layer, and 2) the compression of the outer layer by the collars may be influenced by the inner layer.

Table 5b. Summary of Average Outer Coil Stress Measurements on Selected BNL-Built, 4-cm-Aperture, 17-m-Long Collider Dipole Magnet Prototypes.

Magnet	After Keying (MPa)	After Assembly (MPa)	Before First Cooldown (MPa)	After First Cooldown (MPa)	Before First Warm-up (MPa)	Inner Stress vs I^2 Slope ^a (MPa/A ²)	Contact Current (A)	Warm Collar-Yoke Interference ^b (μ m)	Cold Collar-Yoke Interference ^b (μ m)
DD0026	41.6	48.6	48.0	31.7	29.0	.19	0	241	274
DD0027 ^c	49.1	-	55.4	39.2	35.0	.25	3730	254	143
DD0028 ^c	44.7	32.0	41.6	17.0	13.7	.22	4350	229	118
DC0201	40.1	35.3	35.7	25.5	24.0	.25	5020	51	-60
DC0202	34.9	35.1	34.9	20.5	19.4	.24	4790	177	66
DC0203	47.3	49.2	48.1	28.4	28.7	.28	4680	228	117
DC0204	48.7	38.9	44.8	26.5	25.7	.24	4920	152	41
DC0205	48.3	46.5	45.8	25.4	27.7	.26	4860	177	76
DC0206	48.7	48.6	49.0	30.1	31.7	.27	5020	177	66

^a On average over selected strain gauge runs from the first and second testing cycles.

^b Estimated at the axial location of the strain-gauge pack.

^c At the feed-end pack.

Let us first discuss the reliability of the stress measurements. The stress data presented in Tables 5a and 5b are average values over the four coil quadrants. However, for most of the magnets the standard deviation of the four outer-layer pressures is much larger than that of the inner-layer pressures. (The most dramatic case is magnet DD0027, with a standard deviation of 11.7 MPa for the outer-layer pressures after cooldown, compared to 2.3 MPa for the inner-layer pressures.) This difference can possibly arise from the mounting of the beam-type strain-gauge transducers themselves. As we have already described, in the case of the inner layer the whole pole part of the collar laminations supporting the beams is cut in order to host a solid and accurately EDM'd stainless-steel base.¹⁶ In the case of the outer layer, the beams are also mounted against a solid and accurately EDM'd backing plate, but the backing plate itself rests against a laminated surface. The roughness of this surface does not allow a perfect alignment of the beam, eventually leading to asymmetries between the four quadrants. Of course, this larger spread of the outer stress data raises questions about the reliability of the mean values given in Table 5b.

The question of the influence of the inner layer on the outer-layer pre-compression was already discussed in paragraph 3.2.3.3. As the collars are mounted around the coil, they compress the two layers simultaneously. The two layers can therefore be considered as two parallel springs, as represented in Figure 13. The balance of forces in the collared-coil assembly thus depends on the respective values of the two spring rates. If the inner-layer spring is stiffer, it dominates the outer-layer spring and determines the vertical deflection of the collars, and thus the azimuthal compressive stresses. Another influence which was not discussed in paragraph 3.2.3.3 is that both the inner layer and the collars apply a radial pressure on the outer layer. Because of Poisson's ratio, this radial pressure tends to increase the arc length of the coil outer layer, eventually resulting in an increase of azimuthal compressive stress. Also, the radial pressure introduces frictional forces at the interface between the two coil layers and between the coil outer layer and the collars that can prevent the outer layer from moving freely. All these mechanisms result in variations of the outer-layer pre-compression, which could explain the poor correlation observed in Figure 20.

On the other hand, it is interesting to note that in Figure 12, although the room-temperature stresses did not exhibit any clear correlation to the effective sizes of the outer-layer package, the

LHe-temperature stresses end up showing some kind of correlations, especially for the DC-series magnets. These correlations, however, should be viewed with caution because of the large error bar on each data point, and we shall not elaborate on their significance.

4.3 Change in Coil Axial Pre-Load During Cooldown*

4.3.1 Predicting the Cooldown Change

Predicting the change in coil axial pre-load during cooldown is not as straightforward as it is for the coil azimuthal compressive stress. As we described in paragraph 2.1.5, the coil is loaded axially by means of screws that are set through the end plate. The end plate itself is anchored to a stainless-steel cylinder, called the *bonnet*, which is welded to the outer shell. During cooldown, the end plate is thus expected to follow the shrinkage of the outer shell. Let us first ignore the presence of the iron yoke. The change in coil axial pre-load during cooldown is then determined by the difference in thermal expansion coefficients in the axial direction between the coil and the outer shell. The thermal expansion coefficient of the coil in the axial direction, integrated between room temperature and LHe temperature, was measured at 2.5×10^{-3} , compared to 2.9×10^{-3} for the outer shell steel.³² In this situation, the outer shell thus shrinks more than the coil, and the coil axial pre-load is expected to increase during cooldown. Let us now take the iron yoke into consideration. The yoke laminations used for the nine magnets described in this paper were compactly stacked so that the yoke would behave mechanically as a monolith (see paragraph 2.1.4). During magnet assembly, the outer shell is welded around the yoke (see paragraph 3.3). The welding puts the shell into tension, and the shell then applies a radial pressure on the yoke, eventually closing the yoke midplane gap. The radial pressure results in high frictional forces at the interface between the yoke and the shell. During cooldown, the shell tries to shrink more than the monolithic yoke, whose integrated thermal expansion coefficient between room temperature and LHe temperature was measured to be only 2.0×10^{-3} .³² However, the high frictional forces at the interface prevent the shell from doing so. The frictional forces thus result in an apparent stretching of the outer shell in the axial direction in order to match the thermal shrinkage of the iron yoke. In this situation, the change of axial pre-load during cooldown is determined by the difference in thermal expansion coefficients in the axial direction between the coil and the iron yoke. From the aforementioned data, the axial pre-load is thus expected to decrease during cooldown. In reality, the yoke is not purely monolithic, and part of the differential thermal shrinkage between the yoke and the shell is used to close gaps between the yoke laminations. The change in axial pre-load during cooldown is thus expected to vary from magnet to magnet, depending on the amount of frictional forces between the yoke and the outer shell, and, eventually, on the yoke-packing factor.

4.3.2 Review of Axial Pre-Load Measurements During Cooldown

The coil axial pre-loads, as measured by the bullet gauges before and after the first cooldown of the nine magnets discussed in this paper, are reported in Table 5c. For all but one magnet, the axial pre-load decreased during the first cooldown. The magnet with increasing pre-load is magnet DC0201, which used anti-ovalized, Nitronic-40 steel collars, with no shims between the collars and the yoke. Magnet DC0201 was thus the magnet which was expected to have the lowest vertical interference between the collar and the yoke. Also, it was the only magnet of the series whose yoke midplane gap was measured to be closed at the end of the yoke-stacking, prior to the shell-welding (see Table 3). Therefore, the band clamps used to hold the two shell halves in place around the yoke in preparation for welding required less tension than on other magnets, resulting in a lower

* Analyses of the axial mechanics are preliminary.

Table 5c. Summary of Total End Force Measurements on Selected BNL-Built, 4-cm-Aperture, 17-m-Long Collider Dipole Magnet Prototypes.

Magnet	After Assembly (kN)	Before First Cooldown (kN)	After First Cooldown (kN)	Before First Warm-up (kN)	Initial Force vs. I^2 Slope ^a (kN/A ²)	Final Force vs. I^2 Slope ^a (kN/A ²)	Warm Collar-Yoke Interference ^b (μm)	Cold Collar-Yoke Interference ^b (μm)
DD0026	4.6	8.3	4.4	7.7	0.18	0.24	208	241
DD0027	5.0	11.2	1.0	4.6	0.17	0.24	218	107
DD0028	4.4	14.6	8.1	12.5	0.17	0.24	221	110
DC0201	7.5	6.8	25.6	31.1	0.30	0.35	34	77
DC0202	7.9	14.0	10.6	21.1	0.27	0.32	185	74
DC0203	9.5	16.4	8.6	13.8	0.23	0.24	201	90
DC0204	4.9	8.6	5.9	17.5	0.22	0.26	178	67
DC0205	9.9	12.7	8.7	18.1	0.25	0.26	189	78
DC0206	35.9	45.2	16.0	22.5	0.31	0.34	249	138

^a On average over selected strain gauge runs from the first and second testing cycles.

^b Estimated on average over the magnet length.

radial pressure on the yoke. (As described in paragraph 3.3, the band clamps are tightened until the gap between the two shell halves on each side of the magnet is 1.5 mm.) These two facts are consistent with low frictional forces at the interface between the yoke and the shell, which could eventually account for the observed increase of coil axial pre-load during cooldown. For all other magnets, the yoke midplane gap was measured to be open at the end of the yoke-stacking. To achieve the same gap between the shell halves, the band clamps therefore needed more tension, resulting in a higher radial pressure on the yoke. After shell-welding, this higher radial pressure resulted in a larger perimeter of contact between the shell and the yoke, and thus higher frictional forces at the interface. This is consistent with the observed decrease of axial pre-load during cooldown. Also, one would expect the amplitude of this decrease to be somewhat related to the vertical collar-yoke interference at room temperature, since it is the vertical collar-yoke interference that determines the tension to be put on the band clamps to bring the gap between the shell halves to the required value of 1.5 mm. Let i_w designate the vertical collar-yoke interference at room temperature. As we described in paragraph 3.2.4, the diameters of the collared-coil assembly are routinely measured after the completion of collaring. Let d_v designate the measured vertical diameter. Assuming that the yoke midplane gap is entirely closed at the end of shell-welding, i_w can be estimated as:

$$i_w = d_v - d_y \quad \text{for magnets with no collar-yoke shims,} \quad (20a)$$

and

$$i_w = d_v - d_y + 2t_{c-y} \quad \text{for magnets with collar-yoke shims,} \quad (20b)$$

where d_y is the vertical inner diameter of the iron yoke, and t_{c-y} is the thickness of the shims that were added on the top and bottom of the magnets after and including DC0202 (see paragraph 2.2.5). Figure 21 presents a summary plot of the change in axial pre-load during the first cooldown of the

nine magnets described in this paper as a function of the vertical collar-yoke interference at room temperature. (The value of i_w is that calculated in average over the magnet length.) The cooldown data appear to correlate relatively well with i_w , and they follow the expected trend: the larger the collar-yoke interference at room temperature, the larger the frictional forces between the yoke and the shell, and the larger the decrease of coil axial pre-load during cooldown.

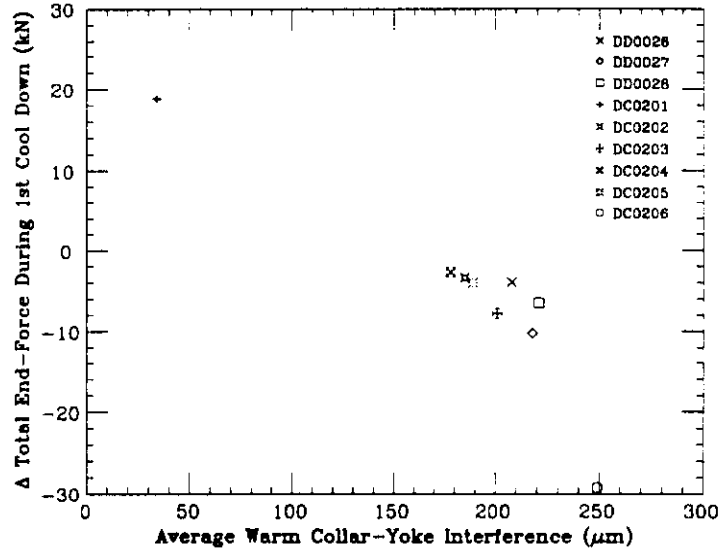


Figure 21. Changes in the force exerted by the coil against the end-plate loading screws during the first cooldowns of the most recent BNL 4-cm-aperture, 17-m-long collider dipole magnet prototypes as a function of the warm collar yoke interference. The force data are summed over the four loading screws. The interference is calculated in average over the magnet length.

As we have seen, the changes in axial pre-load reported in Table 5c can be qualitatively explained. However, one can notice that the LHe temperature values are more scattered than what could be explained by these changes. This is because the room-temperature values were already scattered. As we described in paragraph 3.4, the axial pre-load is set during assembly to a nominal value. However, as the magnet is mounted on the test stand, bellows are welded at the periphery of the bonnet, connecting the magnet cold mass to the He distribution. This welding induces a distortion of the bonnet, resulting in an increase of axial pre-load that greatly varies from magnet to magnet. Aside from the fact that it is not reproducible, this increase is not thought to be a problem, since it goes in the direction of better axial loading. On the other hand, the fact that the axial pre-load can decrease during cooldown, and the fact that the sign and the amplitude of the change depend on a friction coefficient, are more worrisome, for it is difficult, if not impossible, to predict the axial pre-load level at LHe temperature and to ensure that this level will be sufficient. In the case of magnet DD0027, for instance, the axial pre-load at LHe temperature ended up being very small, perhaps leading to poor quench performance. In order to avoid this situation, the setting of the end force was progressively increased on subsequent magnets. Studies are also underway to understand the influence of the yoke-packing factor on the change in axial pre-load during cooldown.

4.4 Summary

In this section, we reviewed the cooldown data for the nine most recent BNL 4-cm-aperture, 17-m-long SSC dipole prototypes. For both the coil azimuthal compressive stress and the coil axial loading, correlations were found between the changes during cooldown and specific assembly

features which could qualitatively account for the observed differences between magnets. For the coil inner-layer, the cooldown stress loss appears to increase with increasing room temperature stress, as can be expected from the non-linearity of the coil stress-strain curve. The sign and the amplitude of the change in coil axial pre-load appear to depend on the warm collar-yoke interference, as can be expected from frictional effects at the interface between the yoke and the outer shell. However, despite the consistency of the cooldown changes, it appears that coil axial pre-load, and, to a lesser extent, the coil pre-compression, end up being relatively spread at LHe temperature. The origin of this spread is to be found in the magnet-to-magnet variation that already existed at room temperature.

5 MAGNET EXCITATION

5.1 Introduction

The Lorentz force has three main components which are applied to the coil as the magnet is energized: 1) an azimuthal component, directed from the pole to the midplane, which tends to compress both the coil inner and outer coil layers, and to unload the collar pole; 2) a radial component, directed outwardly, which tends to bend the collars, with a maximum deflection at the midplane; and 3) an axial component, also directed outwardly, which tends to stretch the coil at the ends. As we described all along, the magnets are designed and assembled in order to provide good support against these three components of the Lorentz force. To compensate the effects of the azimuthal component, the coils are pre-compressed azimuthally at room temperature. To enhance the support against the radial component, the collars and the yoke are made to fit at room temperature, so that at LHe temperature and full excitation the deflecting collared-coil can come into contact with the yoke around the midplane. And last, the coil is prevented from moving axially by the use of thick end plates. (The effects of the axial component of the Lorentz force are also reduced by sharing the force between the collared-coil assembly and the interfering yoke and shell.) It is now time to analyze the behavior during excitation of the nine magnets described in this paper in order to determine whether the design goals have been achieved.

The data reported here are those measured by the two types of strain gauges described in paragraph 2.3. They were taken during specific current cycles called *strain-gauge runs*. A strain-gauge run consists of ramping the current step-by-step up to a maximum value, then down to zero, and reading out the strain gauges at each step; the step increments are usually equally spaced in current squared. (The first magnet excitation after cooldown to a current of the order of the operating current is always a strain-gauge run.) We shall successively discuss the change in the azimuthal pressure exerted by the coil against the collar and the change in the force exerted by the coil against the end plate. As we did for assembly and cooldown, we shall try to determine whether the excitation data are reproducible from magnet to magnet, and if they are not we shall try to explain to explain the differences and find correlations with specific magnet features.

5.2 Change in the Azimuthal Pressure Exerted by the Coil Against the Collar Pole During Excitation

5.2.1 Predicting the Change in Azimuthal Pressure During Excitation

As we described earlier, the main effect on the pressure exerted by the coil against the collar pole is expected to be that of the azimuthal component of the Lorentz force. This component being directed from the pole towards the midplane, the pressure against the collar pole is expected to decrease as a function of current. Also, since the Lorentz force is proportional to the product of the current, I , by the field, and since the field itself is proportional to the current, the decrease is

expected to be linear in current squared. In the following we shall therefore always plot the pressure measurements as a function of current squared, and we shall look at the slope of the pressure versus I^2 . (Note that the operating conditions correspond to approximately 42 kA^2 .)

5.2.2 Review of Inner Layer Pressure Measurements During Excitation

5.2.2.1 Example of Typical Change During Excitation. Figure 22 presents an example of typical change in the inner-layer pressure as a function of current squared during an excitation of magnet DC0204. The four traces correspond to the pressures measured by the four beam-type strain-gauge transducers (one for each quadrant). The arrows indicate the up- and down-ramps of the current.

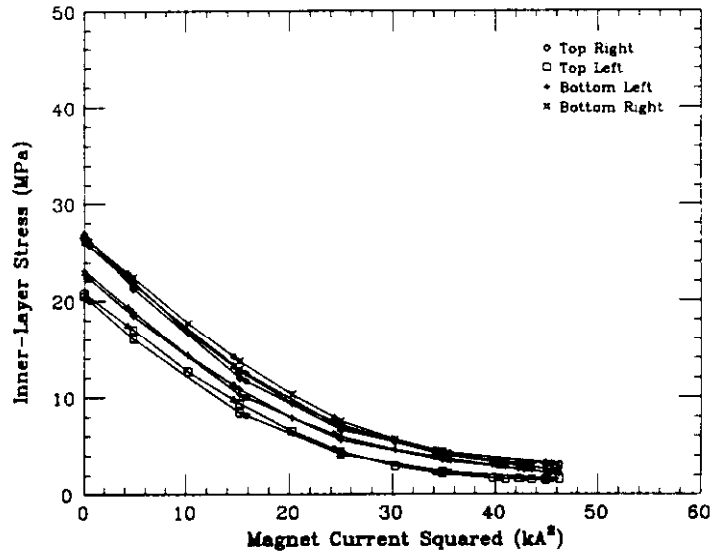


Figure 22. Changes in the azimuthal pressure exerted by the coil inner layer against the collar pole during an excitation of BNL 4-cm-aperture, 17-m-long collider dipole magnet prototype DC0204. The four traces correspond to the four coil quadrants.

It appears that at low currents, the pressure exerted by the coil against the collar pole decreases linearly versus current squared. This is consistent with what was expected from the Lorentz force. As the current increases, however, the pressure flattens out and eventually reaches a constant level. The flattening of the pressure can in part be explained by the non-linearity of the coil stress-strain curve described in paragraph 4.2.1.3. The fact that at high currents the pressure does not change while the Lorentz force is still increasing indicates that the collar pole unloads and that the average pressure exerted by the coil against the pole face becomes zero. (The non-zero values measured by the gauges must result from offsets introduced by differences between the active and compensating-gauge reference resistance values.) In the following, we shall refer to *unloading current*, defined as the current at which the slope of the inner-layer pressure versus I^2 becomes less than 10% of the initial slope.

5.2.2.2 Cross-Magnet Comparison. The unloading of the coil inner layer illustrated in Figure 22 is typical of the magnets discussed in this paper. Figure 23 presents a summary of the inner-layer pressure versus I^2 plots for the nine magnets of interest. For clarity of the presentation, the magnets have been divided into two groups. Figure 23a presents typical plots for magnets DD0026, DD0027, and DD0028, while Figure 23b presents typical plots for the remaining DC-series magnets. For each magnet, the pressures are averaged over the four coil quadrants and only the current up-ramp data are displayed. Aside from magnet DD0027, which was excited up to 7200 A without its inner-layer pressures reaching a plateau, all magnets exhibited unloading. The unloading currents, summarized in Table 5a, range from 6000 A to 7300 A.

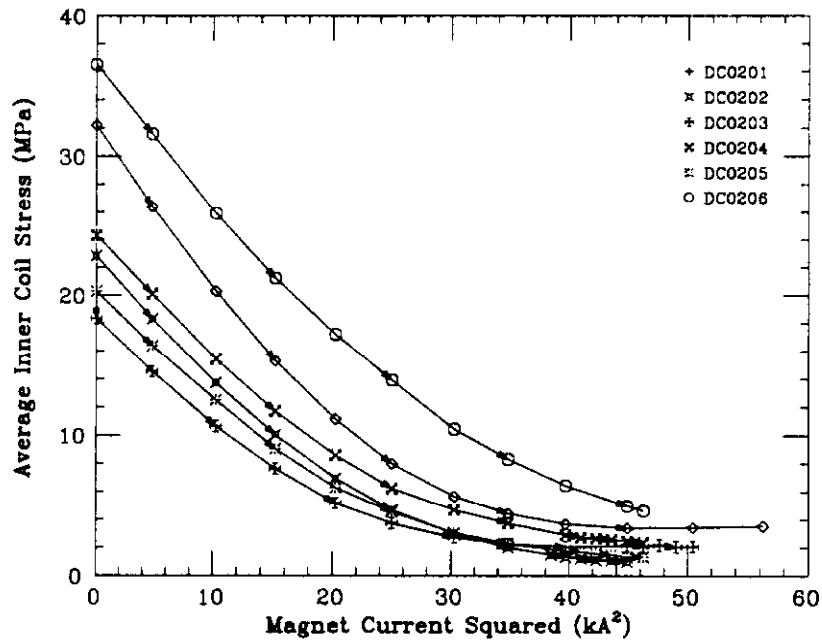
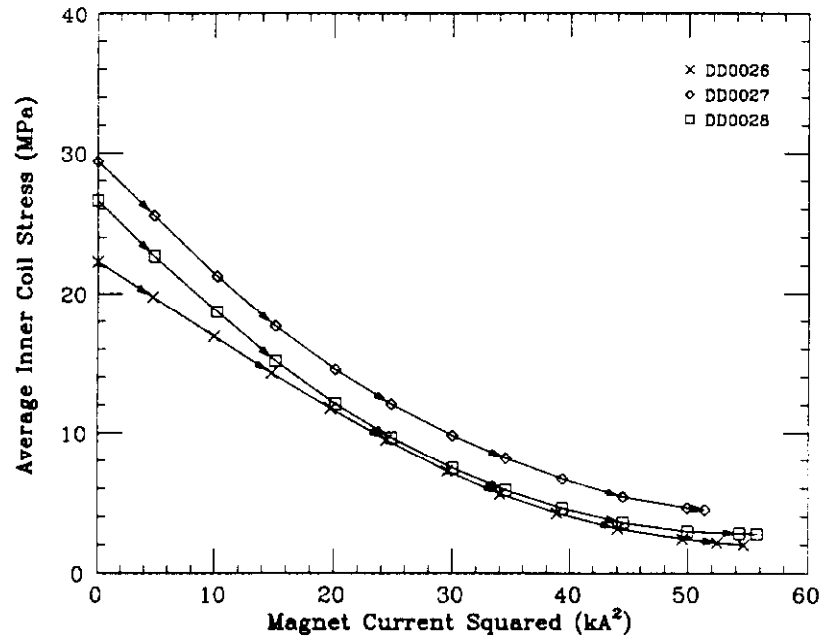


Figure 23. Summary of the changes in the azimuthal pressure exerted by the coil inner layer against the collar pole during excitations of the most recent BNL 4-cm-aperture, 17-m-long collider dipole magnet prototypes: a) DD-series, and b) DC-series magnets. The pressure data are averaged over the four coil quadrants.

Originally, this unloading was not intended; it had not been observed in magnets prior to magnet DD0019.¹⁸⁻²⁰ A prime reason why the actual magnets exhibit such behavior, while the

earlier prototypes did not, is that their level of inner-layer pre-compression at LHe temperature is much lower: 20 MPa for magnet DC0204, compared to 55 MPa for magnet DD0017. Another reason is that for most of the recent magnets, the initial slope of the pressure versus I^2 is larger: 0.78 MPa/kA² for magnet DC0204, compared to 0.56 MPa/kA² for magnet DD0017. The level of cold pre-compression is determined by the pre-compression at room temperature, which is itself controlled by the thickness of the brass shims inserted during assembly between the coil and the collar pole (see paragraph 3.2.1). Magnets after and including DD0019 were deliberately assembled with a lower pre-compression to avoid overstressing the coil insulation during collaring. Thus, obtaining a lower level of pre-compression in the cold state is not surprising. On the other hand, the slope of the stress versus I^2 was expected to depend only on the azimuthal component of the Lorentz force, and was not expected to vary significantly from magnet to magnet.

Let us look more carefully at Figure 23. In Figure 23a, it appears that for high currents (above 5000 A, let us say), the three curves are parallel. However, for lower currents, the slopes for magnets DD0027 and DD0028 appear to be larger than for magnet DD0026. On Figure 23b, it appears that the initial slopes for magnets after and including DC0202 are of the same order, while the initial slope of magnet DC0201 is larger. The initial slope values are also summarized in Table 5a. Overall, the smallest slope is observed for magnet DD0026, which uses round, High-Manganese steel collars: 0.52 MPa/kA². The largest is that of magnet DC0201, which uses anti-ovalized, Nitronic-40 steel collars: 1.05 MPa/kA². The other magnets—which use either round, Nitronic-40 steel collars, or anti-ovalized, Nitronic-40 steel collars, with shims at the tops and bottoms—occupy an intermediate position, with slopes between 0.7 and 0.8 MPa/kA². The dependence of the slope on the collar configuration suggests that it may be related to the collar-yoke interference.

5.2.2.3 Influence of Collar-Yoke Interference. There is no practical way to directly measure the collar-yoke interference at LHe temperature, but it can be estimated. In paragraph 3.2.4, we described how the diameters of the collared-coil assembly were routinely measured after completion of collaring, and in paragraph 4.3.2, we explained how these measurements could be used to estimate the vertical collar-yoke interference at room temperature, i_w (see Eqs. (20a) and (20b)). Assuming that the yoke midplane gap remains closed during cooldown, the vertical collar-yoke interference at LHe temperature, i_{LHe} , can be estimated to be

$$i_{LHe} = i_w - (\alpha_c - \alpha_y) d_y , \quad (21)$$

where α_c and α_y are the thermal expansion coefficients, integrated between room temperature and LHe temperature of the collar and yoke steels, and d_y is the inner diameter of the yoke at room temperature. (In the computations, α_c is taken to be 3.0×10^{-3} for Nitronic-40 steel and 1.7×10^{-3} for High-Manganese steel, $\alpha_y = 2.0 \times 10^{-3}$, and $d_y = 110.8$ mm.)

Figure 24 presents a summary plot of the initial slopes of the inner-layer pressure versus I^2 as a function of the estimated vertical collar-yoke interferences at LHe temperature. For each magnet, the slope is calculated on average over the four coil quadrants. (For magnets DD0027 and DD0028, which were equipped with two strain-gauge packs, we selected the data from the pack located at the minimum coil size location.) The collar-yoke interference is that calculated from Eqs. (20) and (21), using the vertical collar diameter measured at the axial location of the strain-gauge pack. To the data of the nine magnets described in this paper, we added the data of all the previously built, *line-to-line fit* design magnets. This includes magnets DD0016, DD0017, DD0018, and DD0019. Magnets DD0016, DD0017, and DD0028 use round, Nitronic-40 steel collars, while magnet DD0019 uses round, High-Manganese steel collars. The four magnets were assembled with a high room-temperature pre-compression, resulting in large vertical collar deflections. With the exception of magnets DD0018 and DC0206, which are slightly off, all magnets appear to lie on the same line, showing a strong correlation between the initial slope of the pressure versus I^2 and the vertical collar-yoke interference.

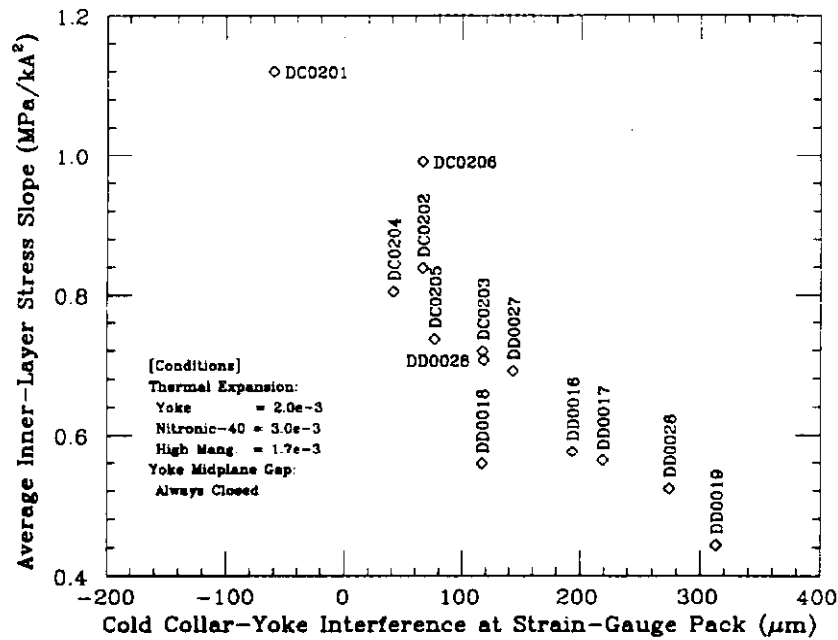


Figure 24. Correlation between the initial slopes of the average inner-layer stress versus current squared and the estimated collar-yoke interferences at LHe temperature of the most recent BNL 4-cm-aperture, 17-m-long collider dipole magnet prototypes. The slopes are averaged over the four coil quadrants. The interference is calculated at the axial location of the strain-gauge pack.

5.2.2.4 Explaining the Influence of the Collar-Yoke Interference. The strong sensitivity of the inner-layer pressure on the vertical collar-yoke interference was not expected, and there is not yet a full understanding of why it happens. One plausible explanation is as follows. As described earlier, in the body of the magnet the Lorentz force has two components: 1) an azimuthal component, which tends to compress the coil towards the midplane, and 2) a radial component, which tends to bend the collars outward, and which is maximum at the midplane. If the yoke is tightly fitted to the collars, it provides a quasi-infinitely stiff support against the radial component of the Lorentz force. The collars do not bend, and the unloading of the collar pole results only from the compression of the coil under the azimuthal component of the Lorentz force. On the other hand, if the yoke is not tightly fitted to the collar, there can be a gap between the collar and the yoke, extending over a certain angle on both sides of the midplane. During energization, the collars bend and the coil deflects accordingly, with a maximum displacement at the midplane. The arc length of the coil thus increases, resulting in a decrease of azimuthal compressive stress. In this case, the initial unloading of the coil from the collar pole results from two causes: 1) the coil compression under the azimuthal component of the Lorentz stress, and 2) the coil bending under the radial component of the Lorentz force. This second factor accelerates the initial rate of unloading of the collar pole, resulting in a higher slope.

The amplitude of the bending moment that stretches the coil depends on the angular extent of the gap between the collars and the yoke with respect to the midplane. The larger the angle, the larger the bending moment. Rather than looking at the gap on both sides of the midplane, one can also look at the perimeter of contact between the collar and the yoke on both sides of the pole plane. The smaller the perimeter, the larger the bending moment. If we assume that the yoke midplane gap is always closed, the perimeter of contact is completely determined by the amount of vertical interference between the collar and the yoke: the larger the interference, the larger the perimeter. This shows that the amplitude of the bending moment should be a decreasing function of the vertical collar-yoke interference. Because the azimuthal component of the Lorentz force is not expected to vary from magnet to magnet, the slope of the inner layer stress should follow the

same dependence as the bending moment and be a decreasing function of the estimated vertical collar-yoke interference at LHe temperature, which is in qualitative agreement with what is observed in Figure 24. (On the other hand, as the current increases and the collars bend, the perimeter of contact between the collars and the yoke increases, resulting in a decreasing bending moment. The bending moment eventually becomes nil as the collars touch the yoke at the midplane. This decrease of the bending moment is another factor contributing to the flattening of the inner-layer stress observed in Figures 22 and 23 at high currents.)

If the above description is correct, the slope of the inner-layer stress provides an indirect measurement of the perimeter of contact between the collar and the yoke, and thus of the collar-yoke interference at LHe temperature. The fact that magnets DD0019 and DD0026 have the smallest slopes conforms with our expectation that the use of High-Manganese steel should provide a tight fit between the collars and the yoke. The fact that magnet DC0201 has the largest slope confirms our fear that the 254- μm reduction of the collar vertical diameter might be excessive and that the collared-coil assembly might be loose inside the yoke at LHe temperature. The fact that the earlier round, Nitronic-40 steel collar magnets, DD0016 and DD0017, have smaller slopes than the later magnets of the same design, DD0027 and DD0028, is consistent with the higher coil pre-compression and the larger collar deflections observed during assembly. And last, the fact that magnets DC0202, DC0203, DC0204, and DC0205 have a slope similar to that of magnets DD0027 and DD0028 shows that the shims that were added on the collars of magnets following DC0202 acted mechanically as they were supposed to; that is, they increased the vertical collar-yoke interference in order to make a magnet originally designed as DC0201 behave like a round-collar magnet. In the case of magnet DD0018, the collar laminations were ground thinner than for magnets DD0016 and DD0017 in order to make tighter collar packs. These tighter packs enhance the rigidity in the radial direction, resulting, during excitation, in a smaller bending moment, thus a smaller slope than for a magnet assembled in the usual way with a similar collar-yoke interference. This could explain why magnet DD0018 lies below the line of the other magnets. As for magnet DC0206, it already appeared that the stress loss measured during cooldown did not follow the trend of the other magnets (see paragraph 4.2.2), which led us to suspect that something was wrong with the mounting of the strain gauge pack itself.

5.2.2.5 Coil Unloading and Quench Performance. We shall describe elsewhere¹⁰ how the quench performance is affected by the bending of the collars and the unloading of the coil inner layer. One can, however, already mention that the coil unloading does not have the dramatic influence one might think it would have. As we said earlier, in the body of the magnet the Lorentz force can be resolved into two components: one radial and one azimuthal. The radial component is maximum at the midplane, but it exists on all the turns of the coil, including the pole turn. The pole turn is normally in contact with the face of the collar pole; the radial component of the Lorentz force, although small, introduces shear stress at the interface of the two. On the other hand, the azimuthal component of the Lorentz force compresses the coil toward the midplane. The pole turn thus tends to part from the face of the collar pole, and the frictional forces at the interface decrease. As the shear stress increases and the frictional forces decrease, the risk of conductor stick-slip motion, eventually leading to quenches, increases. All the magnets described in this paper exhibited training quenches that originated in the inner-layer pole turns, at currents of the order of or above the unloading currents. However, they all reached a plateau within a few percent of the estimated short-sample current limit, and all could be operated at low temperatures—thus higher force levels—without major problems. This shows that although unloading cannot be ruled out as a cause of some of the training quenches, it is not a major threat to the magnet operation.

A possible explanation for why unloading does not necessarily translate into bad quench performance is that it may be only partial. Indeed, the beam-type strain-gauge transducers measure an average pressure, while there can be a large gradient across the collar pole face. As an illustration, Figure 25 shows the results of a collaring experiment that was performed on a coil sample in which sheets of pressure-sensitive paper were inserted between the two coil layers and the collar pole, and between the upper and lower coil halves at the midplane. It appears that at both

the pole and the midplane, the darkness of the impression varies along the conductor width, with a maximum at the inner edge of each layer. This says that the maximum pressure recorded by the paper during the experiment is radius-dependent, and presumably, that there is always a pressure gradient across the collar pole and the coil midplane. Let us assume that such gradient exists at LHe temperature. It is then thinkable that during energization one edge of the coil inner layer starts to unload from the collar pole, while the other edge remains fully loaded. This partial loading may be sufficient to prevent the conductors from moving and to maintain good quench performance. (One of the reasons for the stress gradient observed in Figure 25 is that the brass pole shims used in these magnets —see paragraph 3.2.1— are not tapered, so that the arc length of the collar cavity is smaller at the inner radius than at the outer radius.)

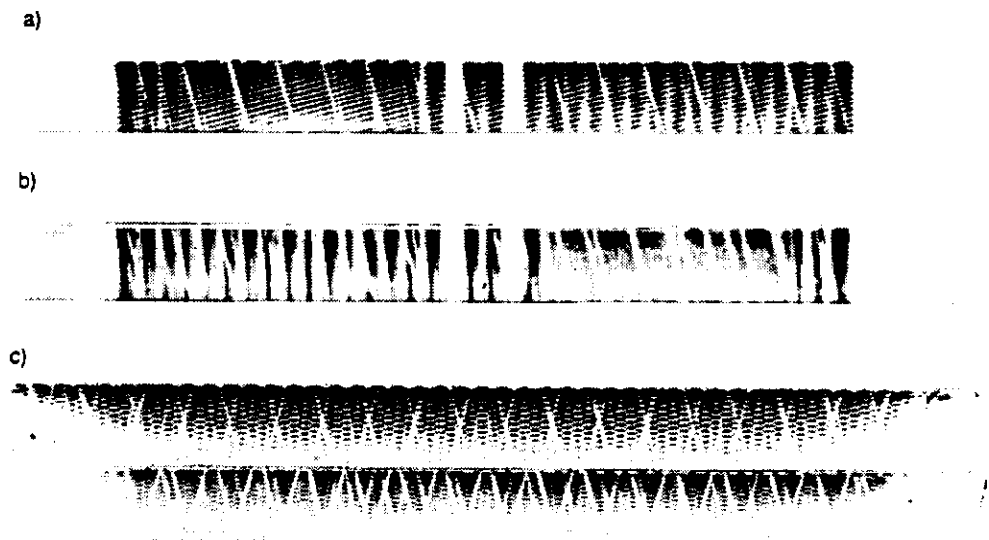


Figure 25. Impressions of pressure-sensitive papers during a collaring experiment on a 4-cm-aperture coil sample: a) across the face of the inner-layer pole turn, b) across the face of the outer-layer pole turn, c) across the coil midplane. The darker impressions correspond to the inner edge of each layer.

5.2.3 Review of Outer Layer Pressure Measurements During Excitation

5.2.3.1 Typical Example of Change During Excitation. Figure 26 presents a typical example of the change in outer-layer pressure as a function of current squared during an excitation of magnet DC0204. The four traces correspond to the pressures measured by the four beam-type strain-gauge transducers (one for each quadrant). The arrows indicate the up- and down-ramps of the current. These data are from the same strain-gauge run as that of Figure 22. Despite the fact that they are widely spread, the four traces appear to be roughly parallel. This indicates that although one can have some doubt about the absolute values of the gauge readouts, their dynamic responses are consistent. They show that, in a manner similar to that of the inner layer, the outer layer has a tendency to unload from the pole, but the amplitude of this unloading is relatively small. The main reason for this smaller unloading is that the integral of the azimuthal component of the Lorentz force over the outer layer is much smaller than for the inner layer.

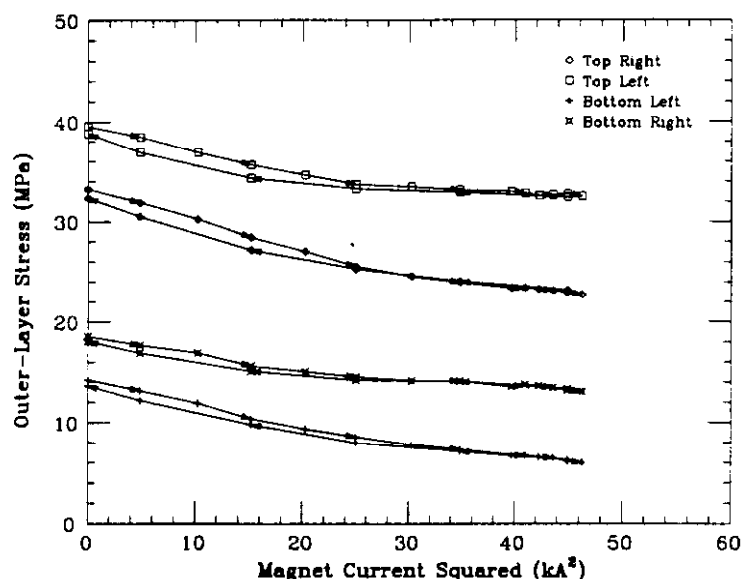


Figure 26. Change in the azimuthal pressure exerted by the coil outer layer against the collar pole during an excitation of BNL 4-cm-aperture, 17-m-long collider dipole magnet prototype DC0204. The four traces correspond to the four coil quadrants.

5.2.3.2 Cross-Magnet Comparison. Figure 27 presents a summary of the outer-layer pressure versus I^2 plots for the nine magnets described in this paper. As for Figure 23, which presented a similar summary for the inner-layer pressure, the magnets are divided into two groups. Figure 27a presents typical plots for the DD-series magnets, while Figure 27b presents typical plots for the DC-series magnets. For each magnet, the pressures are averaged over the four coil quadrants, and only current up-ramps data are displayed.

Let us first comment on Figure 27a. The main features of Figure 27a are: 1) the curve for magnet DD0026 is perfectly straight, 2) the curves for magnets DD0027 and DD0028 exhibit a breaking point, and 3) for currents below the breaking point, the curves of magnets DD0027 and DD0028 are steeper than that of magnet DD0026, while, for currents above the breaking point, the three curves are almost parallel. (In fact, the curve slopes for magnets DD0027 and DD0028 become slightly smaller than the DD0026 slope.) The curves in Figure 27b exhibit features similar to the curves of magnets DD0027 and DD0028 in Figure 27a: they all start with a relatively large slope, then break off, and, for high values of current, exhibit a much smaller slope. In summary, all the magnets with Nitronic-40 steel collars exhibit a breaking point in the outer-layer pressure versus I^2 plot, while the plot for the High-Manganese steel collar magnet is perfectly straight.

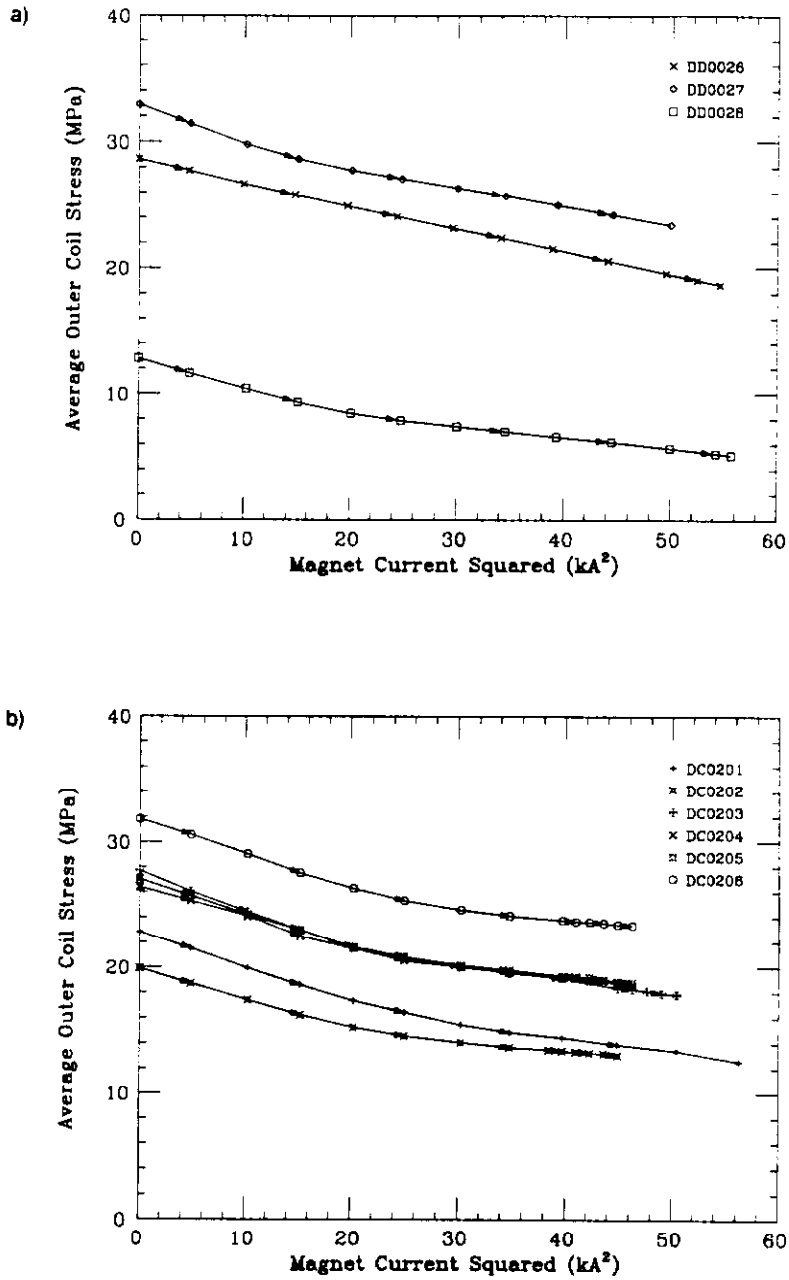


Figure 27. Summary of changes in the azimuthal pressure exerted by the coil outer layer against the collar pole during excitations of the most recent BNL 4-cm-aperture, 17-m-long collider dipole magnet prototypes: a) DD-series, and b) DC-series magnets. The pressure data are averaged over the four coil quadrants.

5.2.3.3 Explaining the Breaking Point. The differences in magnet behavior and the breaking point that is observed in Figure 27 for the Nitronic-40 steel collar magnets are consistent with what can be expected from the model we developed in paragraph 5.2.2.4, and this consistency can be taken as yet another justification of the validity of this model. The starting point of the model is that, in the case of Nitronic-40 steel collar magnets, the magnet cold mass can end up at LHe temperature with a gap between the collared-coil assembly and the yoke, extending over a certain angle on both sides of the midplane. However, during energization, the collar bends outward due to the radial component of the Lorentz force, which is maximum at the coil midplane. This elongation of the collared-coil assembly along the midplane adds a bending moment to the azimuthal component of the Lorentz force, which enhances the rate of unloading of the coil from the collar pole. However, as the current increases, the collared-coil assembly is expected to come into contact with the yoke at the midplane, which then provides a quasi-infinitely stiff support against the radial component of the Lorentz force. As the contact occurs, the additional bending moment disappears. Then, the coil keeps unloading from the pole, but this unloading results from the sole effect of the azimuthal component of the Lorentz force. At the time when the collared-coil assembly comes into contact with the yoke at the midplane, we are thus expecting to see a break in the pressure versus I^2 curve. In summary, the breaking points observed on the curves for the Nitronic-40 collar steel magnets of Figure 27 can be interpreted as the currents for which the collars contact the yoke at the midplane. For currents below the contact current, the unloading of the coil from the collar pole has two causes: 1) the coil compression under the azimuthal component of the Lorentz force, and 2) the coil bending under the radial component of the Lorentz force. Both of these factors result in a relatively large slope of the pressure versus I^2 . For currents above the contact current, the unloading is due only to the azimuthal component of the Lorentz force. The disappearance of the bending moment results in a decrease of the slope of the pressure versus I^2 . In the following we shall refer to *contact current*, the current value for which the collared coil assembly comes into contact with yoke around the midplane.

Let us now consider the case of the High-Manganese steel collar magnet. Here, we expect a tight fit between the collars and the yoke, even at LHe temperature. The yoke should thus always provide a stiff support against the radial component of the Lorentz force, and during excitation there should be no deflection of the collared-coil assembly along the midplane. Thus, at all currents the unloading of the coil from the collar pole should result only from the azimuthal component of the Lorentz force. The plot of the pressure versus I^2 is thus expected to be perfectly linear and should not exhibit any breaking point. This is consistent with what is observed in Figure 27a.

Table 5b summarizes the contact currents for the nine magnets described in this paper. Except for magnet DD0026, for which it is zero, they all lie between 3500 A and 5000 A, thus demonstrating that at full excitation the yoke does provide to the collared-coil assembly the radial support we were seeking. The question that arises now is why we can see such a breaking point on the plots of the outer-layer pressure, when we could not see anything on the plots of the inner-layer pressure. A possible explanation is that in the case of the inner-layer pressure, the breaking point is hidden by the curvature introduced in the plots by the coil non-linear properties. These non-linearities are particularly strong in the low pressure range. They should thus strongly affect the inner-layer pressure, which during energization sweeps a large dynamic range, and at high currents goes to zero. On the other hand, they should not affect too much the outer layer pressures, which sweep a much smaller range and do not appear to go to zero. However, although we did not see any break, we noted in paragraph 5.2.2.2 that in Figure 23a, for high currents, the three curves became parallel, while they diverged for lower currents. We can now add that the currents at which they become parallel are of the same order as the contact currents observed in Figure 27a. The divergence of the three curves at low currents, where variable bending effects are expected to take place, and their parallelism at high currents, where the unloading effects are expected to be similar, are thus consistent with our model.

5.2.3.4 Influence of the Collar-Yoke Interference on the Initial Slope. In the case of the inner layer, we established that the initial slope of the pressure versus I^2 exhibited a good correlation to the vertical collar-yoke interference. One would expect the outer layer initial slopes to exhibit the same kind of correlation. Figure 28 presents a summary plot of the initial slope of the outer-layer pressure versus I^2 as a function of the estimated collar-yoke interference at LHe temperature. For each magnet, the slope is calculated on average over the four coil quadrants, and the collar-yoke interference is that calculated from Eq. (20) using the vertical collar deflections measured at the axial location of the strain-gauge packs. The data presented in Figure 28 are scattered and do not exhibit any clear trend. The fact that quantitatively the initial slopes of the outer-layer pressure do not exhibit a clear correlation is not really a surprise. On several occasions in this paper we questioned the reliability of the outer-layer strain-gauge measurements. We also noticed in paragraph 4.2.3 that for the outer layer there could be some Poisson's ratio effects induced by the radial pressures exerted by the coil inner layer and the collars. As the coil is energized, the radial pressure on the outer layer greatly increases, resulting in larger Poisson's ratio effects, which could eventually compensate for the decrease of azimuthal pressures caused by the other effects. At any rate, we would also expect the variations in collar-yoke interference to result in variations of the outer layer slope of smaller amplitude than for the inner layer slope. Indeed, when the coil deflects to match the midplane bending of the collars, the arc length of the outer layer does not increase as much as that of the inner layer. The amplitude of the bending moment applied on the outer layer is thus smaller than that on the inner layer, resulting in a smaller enhancement of the coil unloading. The combination of all these elements could eventually explain the poor picture given in Figure 28. However, this lack of quantitative correlation does not jeopardize the qualitative observations made on Figure 27.

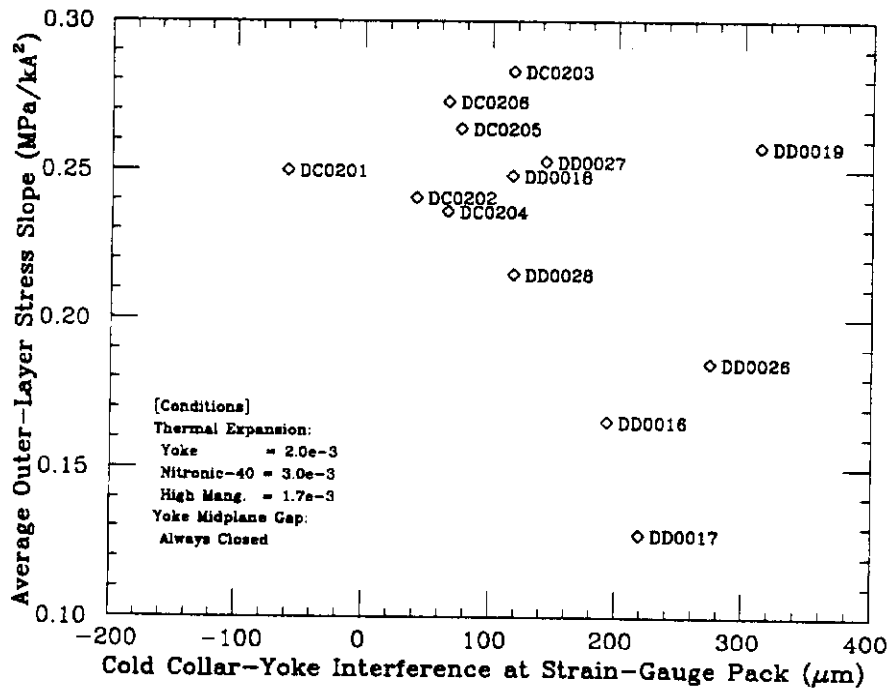


Figure 28. Correlation between the initial slopes of the average outer-layer stress versus current squared and the estimated collar-yoke interferences at LHe temperature of the most recent BNL 4-cm-aperture, 17-m-long collider dipole magnet prototypes. The slopes are averaged over the four coil quadrants. The interference is calculated at the axial location of the strain-gauge pack.

5.3 Influence of the Collared-Coil Assembly Deflections on the Sextupole Component of the Magnetic Field

5.3.1 Predicting the Change during Excitation

In the above paragraphs, we described how for some of the magnets the radial component of the Lorentz force can, at low currents, alter the shape of the collared-coil assembly by producing a deflection along the midplane. We would expect this change of shape to have an effect on some of the multipole components of the magnetic field inside the magnet bore. Computer simulations presented in Reference 23 show that a stretching of the collared-coil assembly along the midplane should result in a decrease of the normal sextupole component, b_2 . As the current increases, b_2 is expected to decrease until it reaches a plateau, when the collared-coil assembly comes into contact with the yoke at the midplane. (At higher currents, the same simulations show that the unloading of the coil from the collar pole should result in an increase of b_2 .) The continuous line of Figure 29 schematizes the expected changes of b_2 as a function of I due to the collared-coil assembly deformations. However, concurrent with these changes of shape are iron-saturation effects. The computer simulations in Reference 23 show that the iron yoke starts to saturate around the pole plane, resulting in an increase of b_2 . At higher currents, it then starts to saturate around the midplane, resulting in a decrease of b_2 , which rapidly overcomes the saturation of the pole. The dashed line of Figure 29 schematized the expected changes of b_2 as a function of I due to iron saturation. Note that for low currents—let us say, I less than 3000 A—there should not be any saturation effect, and thus no change in b_2 due to the iron. The b_2 versus I curve of a magnet is thus expected to be a combination of the two curves of Figure 29.

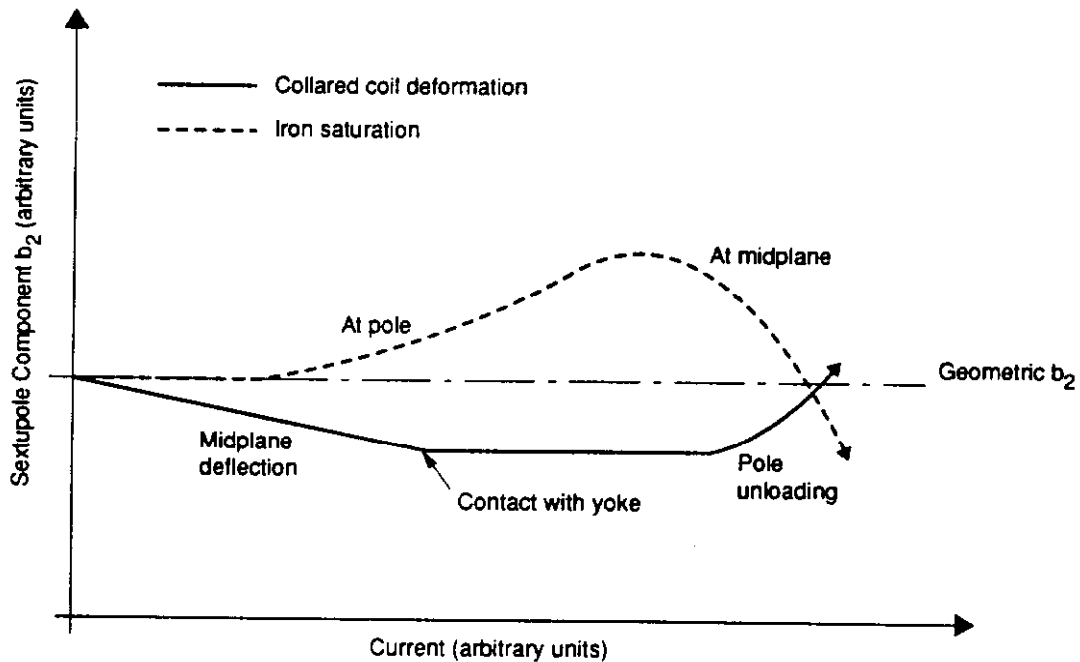


Figure 29. Expected changes in the sextupole component of the magnetic field during an excitation of a BNL 4-cm-aperture, 17-m-long collider dipole magnet prototype due to the deformations of the collared-coil assembly (continuous line) and the effects of iron yoke saturation (dashed line).

5.3.2 Data Review

In reality, the b_2 versus I curves measured on real magnets are more complicated than what we just described. They exhibit a large hysteresis between the up- and down-ramps of the current.³⁵ This hysteretic behavior comes from complicated magnetization effects in the superconducting filaments themselves, which are particularly important at low fields on the conductor, and thus low currents in the magnet. As the current increases, the two branches of the hysteresis become symmetrical and tend toward each other. In order to eliminate the magnetization effects, we shall, as suggested in Reference 23, discard the low currents data, where the hysteresis is not symmetrical, and, for the high currents, we shall consider the average between the up- and down-ramp measurements. The current above which the hysteresis becomes symmetrical was determined empirically to be 2000 A.

Figure 30 presents the up-down averages of the b_2 versus I curves measured on some of the DD-series magnets. The data were plotted using the same ranges for the X- and the Y-scales, but the plots were translated along the vertical axis so that the 2000 A values would coincide. It appears that for I between 2000 and 3000 A, the curves for magnets DD0019 and DD0026 are flat, while the curves for magnets DD0027 and DD0028 decrease. These observations are consistent with what we know of the features of these magnets. Magnets DD0019 and DD0026 use round, High-Manganese steel collars. They are expected to have a tight collar-yoke fit, with no gap around the midplane, even at LHe temperature. Hence, the collared-coil assembly is not expected to deflect along the midplane, and there should be no change in b_2 until the iron saturation effects become sensitive. On the other hand, magnets DD0027 and DD0028 use round, Nitronic-40 steel collars, for which we expect to get a midplane gap between the collars and the yoke at LHe temperature. The collared-coil assembly is thus expected to deflect along the midplane, resulting in a decrease of b_2 as observed in Figure 30. Also, this decrease in b_2 due to collar deflections should stop when

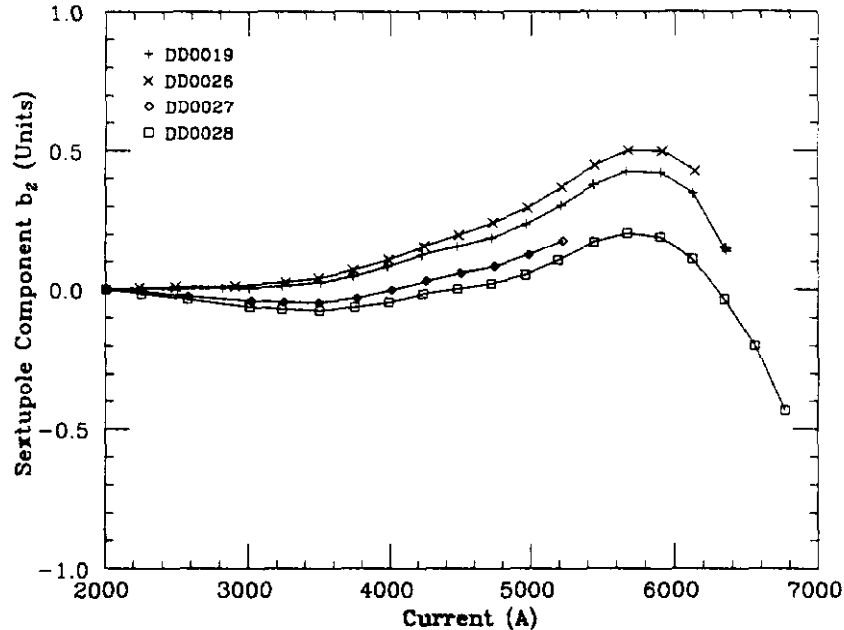


Figure 30. Examples of measurements of the sextupole component of the magnetic field during current cycles of some of the most recent BNL 4-cm-aperture, 17-m-long collider dipole magnet prototypes. The measurements are averaged over the up- and down-ramps of the current. The data are plotted using the same Y-scale, but the plots were translated along the vertical axis so that the 2000-A values would coincide.

the collared coil assembly comes into contact with the yoke. And indeed, the curves for magnets DD0027 and DD0028 appear to flatten out and to exhibit a local minimum for current values of the order of the contact currents determined in paragraph 5.2.3 from the breaks in the outer layer pressure curves. (Note that in the case of Figure 30 the impression of local minimum is reinforced by the effects of the iron saturation at the pole, which start to be sensitive around the same currents.) At any rate, the observations made in Figure 30 are in good agreement with our analyses of the mechanical data and can be taken as an independent justification of the model we developed.

5.4 Change in the Force Exerted by the Coil Against the End Plate During Excitation*

5.4.1 Predicting the Change in End Force During Excitation

As we described earlier, the main effect on the force exerted by the coil against the end-plate loading screws is expected to be that of the axial component of the Lorentz force. This component arises from the solenoidal field, which, in the coil ends, is created by the turnaround of the conductors. The axial component of the Lorentz force being directed outwardly, the force exerted by the coil against the end-plate is expected to increase as a function of current, and, as for the coil azimuthal pressure, the change is expected to be linear in current squared. In the following, therefore, we shall always plot the force measurements as a function of current squared, and we shall also look at the slope of the force versus I^2 .

Because of the axial component of the Lorentz force, the collared-coil assembly is expected to expand inside the yoke while energized. However, as we have described throughout this paper, there is some interference between the collared-coil assembly and the yoke on the vertical diameter, resulting in high frictional forces at the interface. Part of the axial component of the Lorentz force will thus be shared between the collared-coil assembly, the yoke, and the outer shell. Clear evidence of this force-sharing can be found in Reference 17, where measurement results from strain gauges that were mounted on the outer surface of the shell of some earlier 4-cm-aperture, 17-m-long prototypes are presented. Of course, the tighter the clamping of the collared-coil assembly by the yoke, the higher the frictional forces at the interface, and the more force-sharing between the collared-coil assembly, the yoke, and the shell. This larger force-sharing eventually results in a smaller end-force-versus- I^2 slope during excitation. On the other hand, one must also bear in mind that the coil ends themselves are very complicated mechanical objects. They consist of pieces which are made to fit sharply bent, multi-strand cables. If the fit is not perfect, gaps can remain between the conductors or the conductor strands, or between the conductors and the end spacers, leading to non-linear behaviors upon loading. These non-linearities eventually result in variations of the end-force-versus- I^2 slope during excitation. One can also expect magnet-to-magnet variations, depending on the level of axial compressive load at zero current. In summary, many parameters are expected to influence the slope of the end-force versus I^2 , and we have little hope of being able to sort out clearly their respective roles.

5.4.2 Review of End Force Measurements During Excitation

5.4.2.1 Typical Example. Figure 31 presents a typical example of end-force as a function of current squared during an energization of magnet DC0204. The four traces correspond to the four "bullet" gauge assemblies at the return end of the magnet (the return end is the magnet end opposite that where the current leads are connected). The arrows indicate the up- and down-ramps of the current. These data were taken during the same strain-gauge run as for Figures 22 and 26. As expected, the force exerted by the coil against the end-plate loading screws appears to increase quasi-linearly as a function of current squared.

* Analyses of the axial mechanics are preliminary.

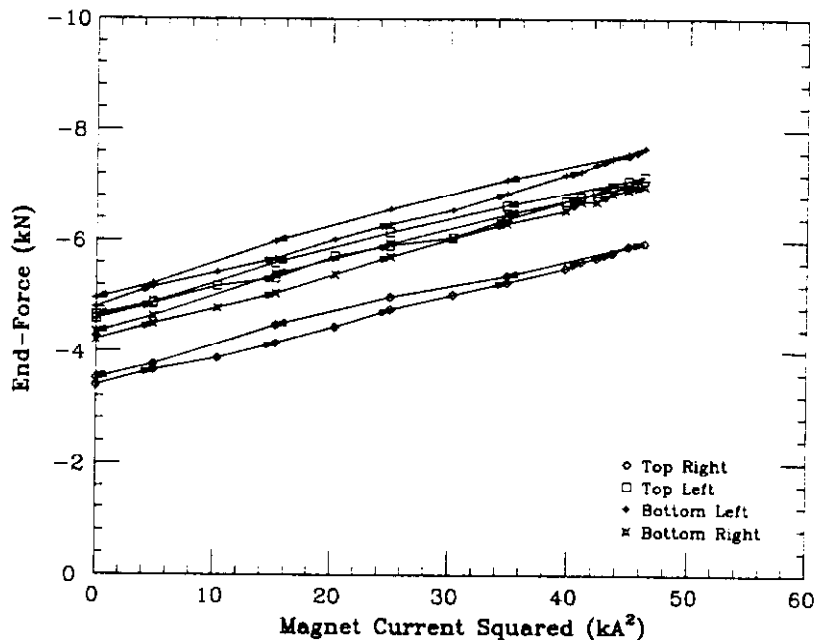


Figure 31. Change in the axial force exerted by the coil against the end-plate loading screws during an excitation of BNL 4-cm-aperture, 17-m-long collider dipole magnet prototype DC0204. The four traces correspond to the four loading screws.

One peculiarity of the end-force data, however, is that the zero-current value appears to increase significantly during the testing cycle. Figure 32 shows, as an illustration, a plot of the total end-force versus time during the first testing cycle of magnet DD0028. Each arrow on the plot corresponds to an excitation of the magnet to a current larger than 4000 A. Each arrow with a number corresponds to a quench. In the case of magnet DD0028, the end-force increased by about 54% during the first cycle, from 8.1 kN, just after cooldown, to 12.5 kN, just before warm-up. As can also be seen on Figure 32, most of this increase takes place at the time of the first quenches, while the end-force remains almost constant during the subsequent quench testing. The observations made here on magnet DD0028 are typical of the nine magnets described in this paper. As can be seen on Table 5.c, they all exhibit a large increase in end-force over their testing cycles, which varies from 3.3 kN for magnet DD0026 to 11.6 kN for magnet DC0204. The origin of this increase is not yet fully understood. One possible explanation is a *ratcheting* of the collared-coil assembly inside the yoke. As we already described, the axial component of the Lorentz force tends to pull the coil ends outwardly. During excitation, the collared-coil assembly thus tends to expand inside the yoke. However, both the collars and the yoke are laminated, and their contact surface is very rough. During excitation, or due to the thermal effects consecutive to a quench, it can thus happen that somewhere toward the magnet ends, some collar laminations slip from one yoke lamination to the other, and that, as the current is ramped down, or the magnet temperature is brought back to normal, these collar laminations stick to their new positions. These slip-stick motions could eventually explain the incremental increases of end-force observed during the first excitations or quenches.

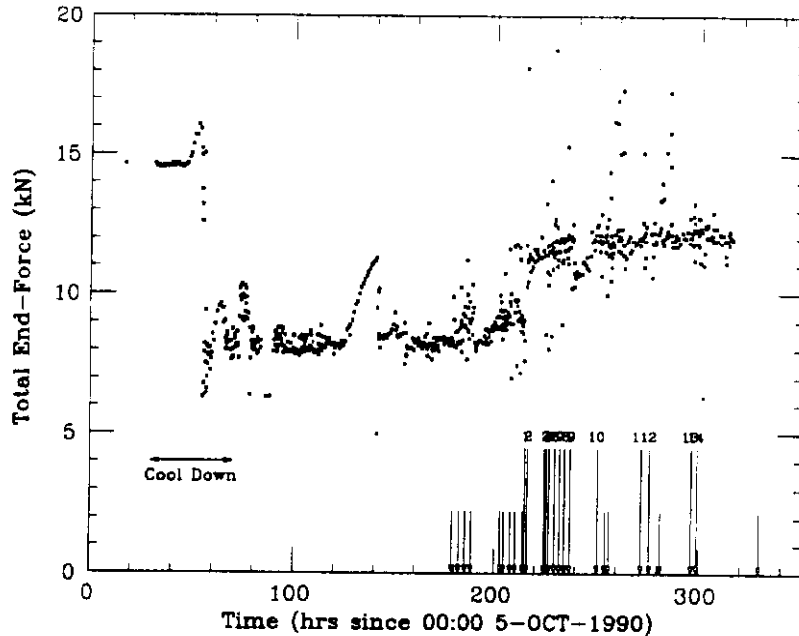


Figure 32. Change in the coil axial compressive load during a testing cycle of BNL 4-cm-aperture, 17-m-long collider dipole magnet prototype DD0028. The data are summed over the four return-end bullet gauges. The small arrows indicate magnet excitations to a current larger than 4000 A. The large arrows surmounted by a number correspond to a quench.

5.4.2.2 Cross-Magnet Comparison. Figures 33 and 34 present summaries of the end-force versus I^2 plots for the nine magnets of interest. The data in Figure 33 correspond to strain gauge runs performed at the beginning of the first testing cycles of each magnet, before the first quench, and, thus, before any substantial ratcheting has taken place. The data in Figure 34 correspond to strain gauge runs performed at the end of the testing cycles, after a quench plateau has been established, and, thus, after most of the ratcheting has taken place. As for Figures 23 and 27, the magnets have been divided into two groups. Figures 33a and 34a present typical plots for magnets DD0026, DD0027, and DD0028; Figures 33b and 34b present typical plots for the DC-series magnets. For each magnet, the force is summed over the four bullet gauges, and only current up-ramps data are displayed. Table 5c also lists the values of the end-force versus I^2 slopes for the different magnets, at both low and high currents. The values are calculated on average over selected strain-gauge runs from the first and second testing cycles of these magnets.

Let us first comment on the DD-series magnets. The main features of Figures 33a and 34a are: 1) the curves of the three magnets are parallel, 2) the curves of Figure 33a are parallel to those of Figure 34a, and 3) the slopes of the end-force versus I^2 appear to increase by about 40%, from 0.17–0.18 kN/kA² at low currents to 0.24 kN/kA² at high currents (see Table 5.c). This increase can be interpreted as a sign that the coil ends stiffen during excitation. (Note that in the case of magnet DD0027, the bullet gauges do register an increase as soon as the coil is energized, despite the fact that the end-force turns out to be almost nil after cooldown. There is thus no evidence of a gap between the end-plate loading screws and the coil ends.) Let us now consider the DC-series magnets. The main features of Figures 33b and 34b are: 1) the DC-series magnets curves are more linear and have larger initial slopes than the DD-series magnets curves, and 2) the DC-series magnets can be divided into two groups. The first group comprises magnets DC0203, DC0204, and DC0205, and is characterized by end-force slopes of 0.22–0.25 kN/kA² at low currents, and 0.24–0.26 kN/kA² at high currents. The second group comprises magnets DC0201, DC0202, and DC0206, and is characterized by end-force slopes which are 25–30% larger than the end-force slopes

of the magnets of the first group. The fact that the end-force curves of the DC-series magnets start with a larger slope and do not exhibit the same curvature as the DD-series magnets curves would seem to indicate that the ends of the DC-series magnets have a more linear behavior upon loading, and thus are better assembled. On the other hand, the larger slopes observed on magnets DC0201, DC0202, and DC0206 would seem to indicate that for these magnets, more of the axial component of the Lorentz force is transmitted to the end-plate, which also indicates that less of the axial force is shared by friction between the collared-coil assembly, the yoke, and the shell. This, again, could be interpreted as a sign that for these magnets the coil ends are stiffer. The reason that magnets DC0201, DC0202, and DC0206 behave as if they had stiffer ends than the other magnets is not yet fully understood. It is, however, noticeable that these magnets are also those with the highest values of axial pre-loads at the end of cooldown. One possible explanation is that the coil ends of these magnets were better pressed, resulting in an enhanced stiffness. (It is also noticeable that despite this enhanced stiffness, these magnets exhibit a ratcheting comparable to that of the other magnets.)

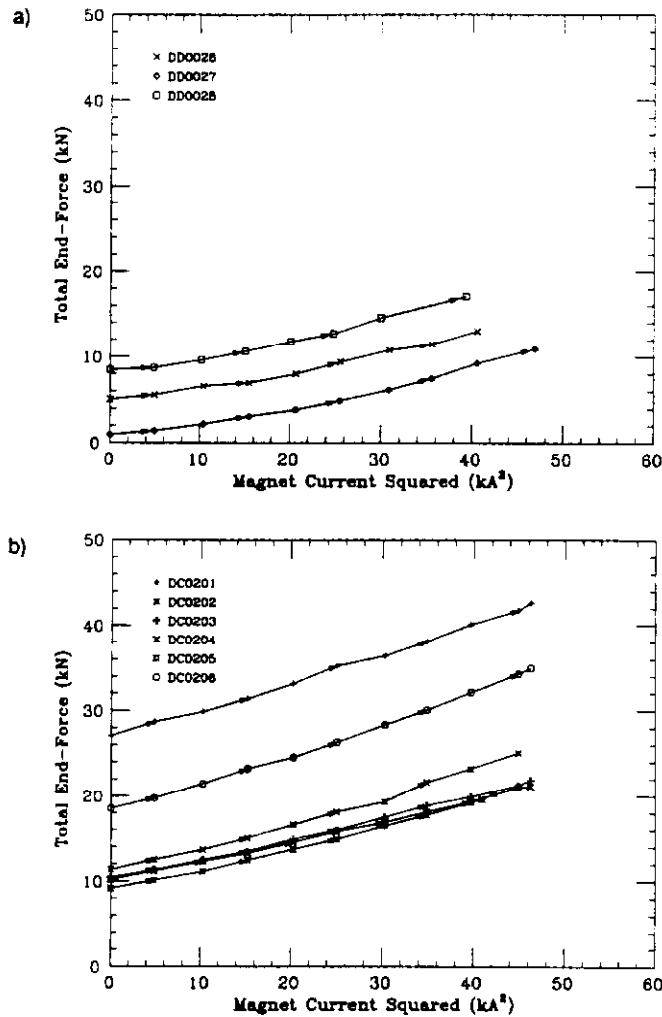


Figure 33. Summary of the changes in the axial force exerted by the coil against the end-plate loading screws during the first excitations to a large current of the most recent BNL 4-cm-aperture, 17-m-long collider dipole magnet prototypes: a) DD-series, and b) DC-series magnets. The force data are summed over the four loading screws.

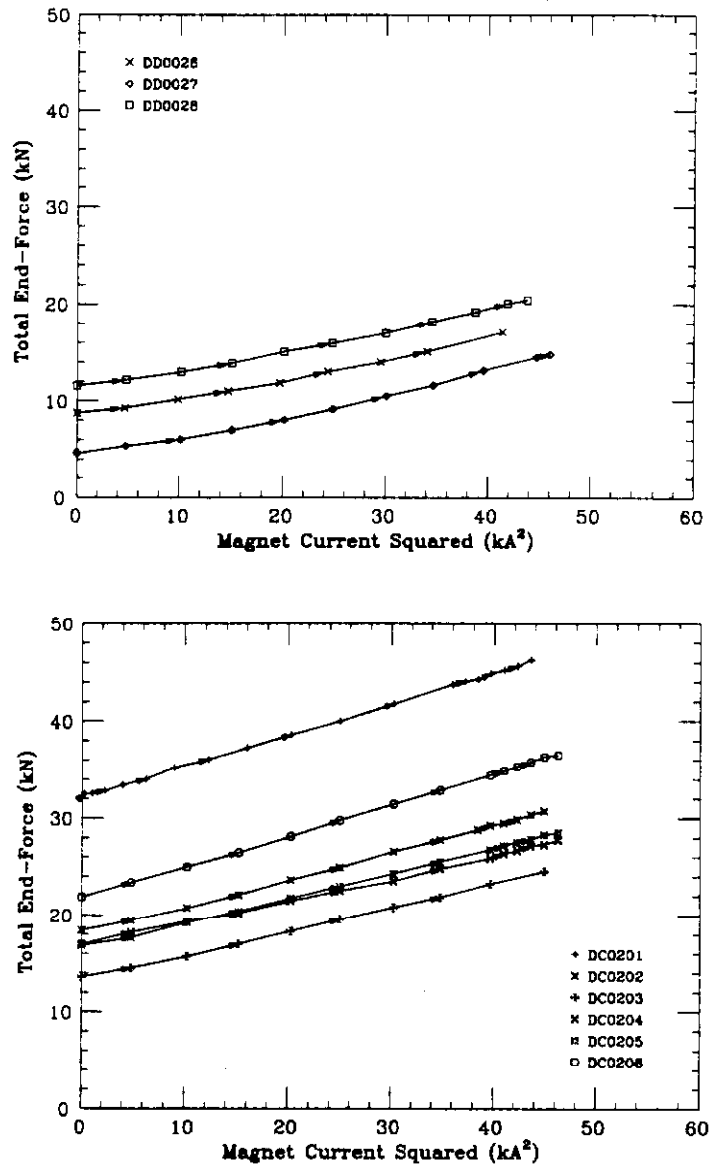


Figure 34. Summary of the changes in the axial force exerted by the coil against the end-plate loading screws during strain gauge runs performed after the establishment of a quench plateau for the most recent BNL 4-cm-aperture, 17-m-long collider dipole magnet prototypes: a) DD-series, and b) DC-series magnets. The force data are summed over the four loading screws.

5.4.2.3 Coil End Stiffness and Quench Performance. We shall describe elsewhere¹⁰ how the quench performance is affected by the end design. One can, however, already mention that there seems to be some kind of correlation between coil-end stiffness and quench performance. Magnets DC0203, DC0204, and DC0205 exhibited relatively poor quench performance, with most of the training quenches occurring in the outer layer of the coil. The training was particularly dramatic at 3.5 K, where none of these magnets reached a quench plateau. On the other hand, magnets DC0201, DC0202, and DC0206 exhibited relatively good quench performance, with all training

quenches but one in the coil inner layer. (The only outer-layer quench was observed during the test at 3.85 K nominal of magnet DC0202, and occurred at a current of 7351 A.) The two groups of magnets we defined in paragraph 5.4.2.2 can thus also be characterized by the pattern of their quench performance: magnets DC0203, DC0204, and DC0205 had poor quench performance, and were limited by their coil outer layer, while magnets DC0201, DC0202, and DC0206 had much better quench performance, with little training in their coil outer layer. The occurrence of training quenches in the coil outer layer is always a surprise, for the peak field on the outer conductor is smaller than on the coil inner layer, resulting in an operating margin a few percent larger. On the other hand, if we consider the axial component of the Lorentz force, the total force applied to the outer-layer ends is calculated to be 1.8 times larger than for the inner-layer ends.³⁶ Since the force applied to the outer-layer ends is larger, one can expect the outer layer to be more sensitive to the details of the coil-end design. Also, since the outer layer is in direct contact with the collars, one can expect the outer layer to be more sensitive to the eventual slip-stick motions of the collars described earlier. These considerations, along with the magnet test results, seem to make the case that poor training performance in the coil outer layer may be related to a lack of end-stiffness.

5.5 Summary

In this section, we reviewed the excitation data of the nine most recent BNL 4-cm-aperture, 17-m-long SSC dipole magnet prototypes. We successively analyzed the changes in azimuthal compressive stress in the coil inner and outer layers, and the changes in axial compressive load at the coil ends. We saw that for most of the magnets, the azimuthal pressure exerted by the coil inner layer against the collar pole decreased to zero during energization, revealing a possible unloading of the pole. We also found that the initial rate of decrease of the inner-layer stress during energization varied from magnet to magnet and could be correlated to the estimated vertical interference between the collars and the yoke at LHe temperature. These variations can be explained by the existence, at low currents, of a bending moment resulting from the radial component of the Lorentz force, which deflects the collared-assembly along the midplane and tends to close the eventual gap between the collared-coil assembly and the yoke. The existence of this bending moment is supported by the observation of a breaking point in the outer-layer pressure, which can be interpreted as the current at which the collared-coil assembly comes into contact with the yoke at the midplane. It is also supported by the observation, during excitation, of variations in the sextupole component of the magnetic field, which are in good qualitative agreement with the assumed deformations of the collared coil assembly. As for the axial compressive load, we first noted that during excitation the bullet gauges registered a quasi-linear increase as a function of current squared, as could be expected from the axial component of the Lorentz. However, it also appeared that the zero-current compressive load increased significantly over the testing cycle, especially at the times of the first excitations or quenches following cooldown. We suggested that this increase resulted from a ratcheting of the collared-coil assembly inside the yoke. It also appeared that there were subtle magnet-to-magnet variations in the values of the slope of the end-force versus current squared. We interpreted these slope differences in terms of stiffness of the coil-end parts, and we suggested a possible correlation between a lack of stiffness in the coil end parts and a poor training performance in the coil outer layer.

6 CONCLUSION

The main origin of quenches in superconducting particle accelerator magnets is thought to be the frictional motion of conductors or conductor strands, or of parts of the cold mass directly in contact with the superconducting coil. From there, two options are open to the magnet designer: either design magnets where everything is tightly clamped, in order to limit the risk of motion, or

design magnets where the main components are free to slide in order to render most of the motions elastic and to limit the risk of frictional heating. Early in the SSC dipole-magnet R&D program, the first school of thought prevailed. This led to the so-called line-to-line fit design, developed by Brookhaven National Laboratory, where the collared-coil assembly is meant to be fully constrained, both radially and axially, by a tightly fit yoke and thick end plates. Several 4-cm-aperture, 17-m-long dipole magnet prototypes were built in order to test the design concepts, and this paper reports on the fabrication, assembly, and mechanical behavior during cooldown and excitation of the nine most recent ones. For the nine prototypes, it appears that at LHe temperature and 6500 A, the collared-coil assembly is in contact with the yoke around the midplane, and that the coil ends are also in contact with the end-plate loading screws. For these magnets, the radial support of the collared-coil assembly around the midplane and the axial support of the coil at the ends can thus be considered to conform to the design. The next step would be to determine whether the efforts to achieve these two goals translate into suitable quench performance. This, however, will be the subject of another discussion.¹⁰

ACKNOWLEDGEMENTS

The authors are grateful to Mel Month for his continuous support during the redaction of the paper. We wish to thank James Naples, DeeDee Kennedy, Tom Coyne, Sue Weaver, Rebekah Hafley and Valerie Kelly for their help in preparation of this paper in a timely fashion.

REFERENCES

1. J. D. Jackson, ed., "Conceptual Design of the Superconducting Super Collider," SSC-SR-1020, March 1986; revised, September 1988.
2. J. R. Sanford and D. M. Matthews, eds., "Site-Specific Conceptual Design of the Superconducting Super Collider," SSCL-SR-1056, July 1990.
3. T. Garavaglia, K. Kaufman, and R. Stiening, "Application of the SSCTRK Numerical Simulation Program to the Evaluation of the SSC Magnet Aperture," SSCL-265, April 1990.
4. T. J. Peterson and P. O. Mazur, "A Cryogenic Test Stand for Full Length SSC Magnets with Superfluid Capability," *Supercollider 1*, M. McAshan, ed., 1989, pp. 551-559.
5. J. Strait, M. Bleadon, et al., "Fermilab R&D Test Facility for SSC Magnets," *Supercollider 1*, M. McAshan, ed., 1989, pp. 561-572.
6. A. Devred, T. Bush, et al., "Status of 4-cm-Aperture, 17-m-Long SSC Dipole Magnet R&D Program at BNL. Part I: Magnet Assembly," to appear in the proceedings of the 3rd Annual International Industrial Symposium on the Super Collider, Atlanta, GA, USA, March 13-15, 1991.
7. A. Devred, T. Bush, et al., "Status of 4-cm-Aperture, 17-m-Long SSC Dipole Magnet R&D Program at BNL. Part II: Mechanical Behavior," to appear in the proceedings of the Cryogenic Engineering Conference, Huntsville, AL, USA, June 11-14, 1991.
8. J. Kuzminski, T. Bush, et al., "Test Results of BNL Built 40-mm-Aperture, 17-m-long SSC Collider Dipole Magnets," presented at the 12th International Conference on Magnet Technology, Leningrad, USSR, June 23-28, 1991.
9. P. Wanderer, M. Anerella, et al., "Results of Magnetic Field Measurements of 40-mm-Aperture, 17-m-Long SSC Model Collider Dipole Magnets," presented at the 12th International Conference on Magnet Technology, Leningrad, USSR, June 23-28, 1991.
10. A. Devred, T. Bush, et al., "Status of 4-cm-Aperture, 17-m-Long SSC Dipole Magnet R&D Program at BNL. Part III: Quench Performance," to be published.
11. A. Devred, T. Bush, et al., "Status of 4-cm-Aperture, 17-m-Long SSC Dipole Magnet R&D Program at BNL. Part IV: Field Quality," to be published.
12. J. Strait, B. C. Brown, et al., "Full Length Prototype SSC Dipole Test Results," *IEEE Trans. Magn.*, **23**, No. 2, March 1987, pp. 1208-1214.
13. J. Strait, B. C. Brown, et al., "Tests of Prototype SSC Magnets," *Proceedings of the 1987 IEEE Particle Accelerator Conference*, Washington, D.C., USA, March 16-19, 1987, pp. 1540-1542.
14. J. Strait, B. C. Brown, et al., "Tests of Prototype SSC Magnets," *IEEE Trans. Magn.*, **24**, No. 2, March 1988, pp. 730-733.
15. A. Devred, M. Chapman, et al., "Quench Start Localization in Full-Length SSC R&D Dipoles," *Supercollider 1*, M. McAshan, ed., 1989, pp. 73-83.
16. C. L. Goodzeit, M. D. Anerella, et al., "Measurement of Internal Forces in Superconducting Accelerator Magnets with Strain Gauge Transducers," *IEEE Trans. Magn.*, **25**, No. 2, 1989, pp. 1463-1468.
17. J. Strait, B. C. Brown, et al., "Tests of Full Scale SSC R&D Dipole Magnets," *IEEE Trans. Magn.*, **25**, No. 2, 1989, pp. 1455-1458.
18. J. Tompkins, M. Chapman, et al., "Performance of Full-Length SSC Model Dipoles: Results from 1988 Tests," *Supercollider 1*, M. McAshan, ed., 1989, pp. 33-49.
19. J. Strait, M. Bleadon, et al., "Full Length SSC R&D Dipole Magnet Test Results," *Proceedings of the 1989 IEEE Particle Accelerator Conference*, Chicago, IL, USA, March 20-23, 1989, pp. 530-532.

20. C. Goodzeit, P. Wanderer, et al., "Status Report on SSC Dipole R&D," to appear in the Proceedings of the 10th Workshop on the INFN Eloisatron Project—New Techniques for Future Accelerators, High Energy Intensity Storage Rings, Status and Prospects for Superconducting Magnets, Erice, Italy, October 16-24, 1989.
21. C. Peters, K. Mirk, et al., "Use of Tapered Key Collars in Dipole Models for the SSC," *IEEE Trans. Magn.*, **24**, No. 2, 1988, pp. 820-822.
22. A. K. Ghosh, M. Garber, et al., "Training in Test Samples of Superconducting Cables for Accelerator Magnets," *IEEE Trans. Magn.*, **25**, No. 2, 1989, pp. 1831-1834.
23. R. Gupta, J. G. Cottingham, et al., "A Comparison of Calculations and Measurements of the Field Harmonics as a Function of Current in the SSC Dipole Magnets," to appear in the proceedings of the 1991 IEEE Particle Accelerator Conference, San Francisco, CA, USA, May 6-9, 1991.
24. R. P. Schutt and M. L. Rehak, "Transverse Cooling in SSC Magnets," *Supercollider 2*, M. McAshan, ed., 1990, pp. 209-217.
25. P. Dahl, J. Cottingham, et al., "Construction of Cold Mass Assembly for Full-Length Dipoles for the SSC Accelerator," *IEEE Trans. Magn.*, **23**, No. 2, 1987, pp. 1215-1218.
26. T. Ogitsu, K. Machata, et al., "Mechanical Hysteresis of Superconducting Coils," to be published.
27. A. Bonito Oliva, P. Gagliardi, et al., "A Statistical Analysis of the Whole Ansaldo HERA Dipoles Production," to appear in the proceedings of the 13th International Cryogenic Engineering Conference, Beijing, China, 1990.
28. J. Strait, private communication.
29. T. Reed, private communication.
30. C. Ferrero, C. Marinari, et al., "The Choice of Strain Gauge For Use in a Large Superconducting Alternator," *Adv. Cryo. Eng.*, **27**, 1982, pp. 1173-1181.
31. F. Pavese, "Investigation of Transducers for Large-Scale Cryogenic Systems in Italy," *Adv. Cryo. Eng.*, **29**, 1984, pp. 869-877.
32. C. Goodzeit, private communication.
33. J. Zbasnik, private communication.
34. T. Shintomi, T. Ogitsu, et al., "Design, Fabrication, and Test of a 5-cm Aperture, 1-m-Long Superconducting Dipole Prototype for High Energy Hadron Collider," *IEEE Trans. Magn.*, **27**, No. 2, 1991, pp. 1743-1747.
35. K. -H. Meß, and P. Schmüser, "Superconducting Accelerator Magnets," Proceedings of the CERN Accelerator School on Superconductivity in Particle Accelerators, Hamburg, FRG, May 30-June 3, 1988, CERN 89-04, 1989, pp. 87-148.
36. D. Orrel, private communication.